Universiteit
Leiden
The Netherlands

From intracluster medium dynamics to particle acceleration

Zhang, X.

Citation
Zhang, X. (2022, June 29). *From intracluster medium dynamics to particle acceleration*. Retrieved from https://hdl.handle.net/1887/3421512

Version:	Publisher's Version
License:	Licence agreement concerning inclusion of doctoral thesis in the Institutional Repository of the University of Leiden
Downloaded from:	https://hdl.handle.net/1887/3421512

Note: To cite this publication please use the final published version (if applicable).

From intracluster medium dynamics to particle acceleration

Proefschrift

ter verkrijging van
de graad van doctor aan de Universiteit Leiden,
op gezag van rector magnificus prof.dr.ir. H. Bijl,
volgens besluit van het college voor promoties
te verdedigen op woensdag 29 juni 2022
klokke 11.15 uur

door

Xiaoyuan Zhang
张啸远

geboren te Ningbo, China
in 1992

Promotor:	Prof.dr. J.S. Kaastra	
Co-promotor:	Dr. A. Simionescu	
Promotiecommissie:	Prof.dr. H.J.A. Röttgering	
	Prof.dr. H. Hoekstra	
	Prof.dr. K.H. Kuijken	
	Prof.dr. M.W. Wise	(Universiteit van Amsterdam)
	Dr. N. Ota	(Nara Women's University)

ISBN: 978-94-6423-861-7

©2022 Xiaoyuan Zhang

The cover is designed by Xiaoyuan Zhang. It is an image simulated from a power spectrum of a $-11/3$ slope power law. Python modules used: `TurbuStat` and `matplotlib`.

To my wife

Contents

1 Introduction **1**

1.1 Galaxy clusters and the intracluster medium 1

1.1.1 X-ray instruments and observations 3

1.2 Gas motions in the ICM 4

1.2.1 Shocks and cold fronts as evidence of ICM dynamics 5

1.2.2 Quantifying ICM gas motions 7

1.3 Nonthermal views of galaxy clusters 11

1.3.1 Radio relics 12

1.3.2 Radio halos 12

1.4 Connecting the nonthermal to the thermal properties 13

1.4.1 X-ray - radio associations 13

1.4.2 Accelerations mechanisms by gas motions 16

1.5 This thesis 17

1.6 Future prospects 19

2 X-ray study of the merging galaxy cluster Abell 3411-3412 with *XMM-Newton* and *Suzaku* **21**

2.1 Introduction 23

2.2 Data reduction 25

2.2.1 XMM-Newton 25

2.2.2 Suzaku 27

2.2.3 Chandra 27

2.3 Imaging analysis 29

2.4 Spectral analysis 30

2.4.1 XMM-Newton 31

2.4.2 Suzaku 34

2.4.3 XMM-Newton-Suzaku cross-calibration 36
2.5 Results 36
2.5.1 Properties of surface brightness discontinuities 36
2.5.2 Global temperature 40
2.5.3 Temperature profiles to the outskirts 41
2.6 Discussion 42
2.6.1 T_{500} discrepancy 42
2.6.2 Shock properties 44
2.6.3 The mystery of the southern edge 47
2.6.4 The location of the bow shock 48
2.7 Conclusion 50
2.A Light curves of EPIC CCDs 52
2.B Soft proton modelling 52
2.B.1 Spectral analysis 53
2.B.2 Vignetting function 55
2.B.3 Self-calibration 56
2.C Cosmic X-ray background 59
2.C.1 Point-source flux and the $\log N - \log S$ relation 60
2.C.2 Detection limit and CXB flux 62

3 Deep *Chandra* observations of merging galaxy cluster ZwCl 2341+0000 **67**
3.1 Introduction 69
3.2 Observations and data analysis 71
3.2.1 Chandra X-ray data 71
3.2.2 GMRT and JVLA radio data 78
3.3 Results 81
3.3.1 General X-ray properties 81
3.3.2 SE edge 84
3.3.3 SW bays 85
3.3.4 NE and western wings 86
3.3.5 NW cone 87
3.3.6 Bridge and northern outskirts 89
3.4 Discussion 90
3.4.1 Shock fronts and radio relics 90
3.4.2 Conic subcluster 92
3.4.3 The origin of the NE wing 96
3.5 Conclusion 97

3.A JVLA B-configuration radio map . . . 99
3.B Radio spectral index uncertainty map . . . 99
3.C Temperature uncertainty map . . . 99
3.D Projected surface brightness profile for a cone-shaped cold front . . . 101

4 ClG 0217+70: A massive merging galaxy cluster with a large radio halo and relics 103
4.1 Introduction . . . 104
4.2 Observations and data reduction . . . 105
4.3 Data analysis and results . . . 105
4.3.1 Spectral properties and X-ray redshift . . . 107
4.3.2 X-ray morphology and surface brightness discontinuities . . . 109
4.4 Discussion . . . 111
4.4.1 Radio halo scaling relations . . . 111
4.4.2 The western X-ray "channel" . . . 111
4.4.3 Possible merging scenario . . . 113
4.5 Conclusion . . . 113

5 The *Planck* clusters in the LOFAR sky: Dynamic states and density fluctuations of the intracluster medium 115
5.1 Introduction . . . 116
5.2 X-ray sample . . . 117
5.2.1 Sample for morphological analysis . . . 119
5.2.2 Sample for power spectral analysis . . . 119
5.3 Data reduction and spectral analysis . . . 120
5.3.1 XMM-Newton EPIC spectral analysis . . . 120
5.3.2 pn background scaling . . . 122
5.4 Morphological parameters . . . 123
5.4.1 Individual measurements . . . 124
5.4.2 Discrepancy in concentration parameter . . . 124
5.4.3 Discrepancy in centroid shift . . . 127
5.4.4 Relaxation score . . . 128
5.5 ICM density fluctuations on large scales . . . 128
5.5.1 Calculation of 2D surface brightness fluctuations . . . 128
5.5.2 A_{2D} spectra and correlations with other parameters . . . 131
5.5.3 Turbulent velocity dispersion . . . 131

5.6 Relation between radio halo power and ICM thermodynamic properties . . . 133
5.7 Discussion . . . 136
5.8 Conclusion . . . 137
5.A Temperature measurements of the sample . . . 148

Bibliography **149**

Nederlandse Samenvatting **159**

English Summary **163**

List of publications **167**

Curriculum Vitae **171**

Acknowledgments **173**

1 Introduction

1.1 Galaxy clusters and the intracluster medium

Back to the 18th century, Charles Messier compiled his illustrious catalog of nebulae and stellar clusters (Messier 1781) and noticed the concentration of 'nebulae' in the Virgo constellation. Almost at the same time, Wilhelm Herschel published his famous work on mapping the structure of the Universe (Herschel 1785), where he described the Coma Cluster as 'nebulous stratum'. The nature of this type 'nebulae' was disclosed one hundred years later by Hubble (1929) as galaxies outside our Milky Way. A few years later, Zwicky (1933) first estimated the mass of the Coma Cluster using the velocity dispersion of member galaxies and first proposed the idea of dark matter to account for the missing mass in galaxy clusters. In 1958, a well known optical catalog of galaxy clusters was published by Abell (1958), where clusters are divided into 6 richness classes based on the number of member galaxies. A review by Biviano (2000) explicitly covers the early day research on galaxy clusters until the departure of George Abell in 1983.

Modern observational, theoretical and numerical simulation works on cosmology build up a grand picture of the structure formation. In this picture, the large scale structure (LSS) is formed hierarchically by the collapse of gravitationally bound overdensities from the initial density perturbation field. The nodes of the cosmic web, which are gravitationally bound, are termed as *halos*, where dark matter is the predominant mass content. In the hierarchical formation, halos of galaxies are formed first, followed by galaxy groups. The most massive halos, galaxy clusters, are formed at $z \lesssim 2$, corresponding to a lookback time of $t \sim 10.5$ Gyr based on a consensus concordance ΛCDM cosmology. The halos of galaxy clusters are still

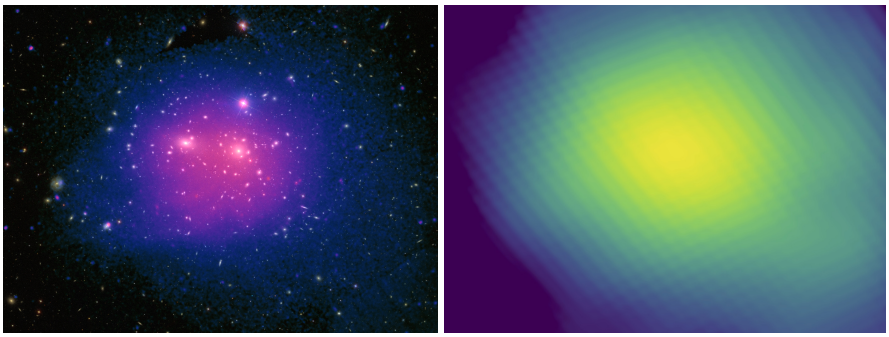

Figure 1.1: *Left*: Optical and X-ray composite image of the Coma Cluster. The yellows spots are individual galaxies in optical and the blue to magenta color is the ICM in X-rays. *Right*: *Planck* SZ map of the same sky region. Image credit: ESA/XMM-Newton/SDSS/Jeremy Sanders/Planck.

growing through cosmic accretion and mergers. See Kravtsov & Borgani (2012) for a review on galaxy cluster formation. In the context of structure formation, the cosmological parameters, such as density fractions of baryonic matter, dark matter and dark energy, and the dark energy equation of state determine the growth of the LSS. Therefore, galaxy clusters are one of the important probes for constraining the properties of our Universe, see Allen et al. (2011) for a review on observational cosmology using galaxy clusters.

Beside the macroscopic view of structure formation, galaxy clusters are key laboratories for studying the physics of space plasma. The intracluster medium (ICM), which is observed as a gaseous halo in X-rays (see Fig. 1.1), contributes the major proportion of baryonic matter. The ICM has several extreme properties among all forms of space plasma: 1) it fills the whole dozens Mpc^3 volume inside the accretion radius of the cluster; 2) it has low densities ranging from $\sim 10^{-5}$ cm^{-3} in the outskirts to $\sim 10^{-2}$ cm^{-3} at the center; 3) it has a high temperature of about a few keV ($\sim 10^7$–10^8 K), where H and He are totally ionized; 4) the magnetic field strength in the ICM is weak, usually a few μG, resulting a high plasma $\beta_{\rm pl}$ parameter[1] > 100.

The tenuous and extreme hot nature of the ICM makes it optically thin and X-ray bright, and it is in collisional ionization equilibrium (CIE). The main radiative processes are thermal bremsstrahlung for the continuum

[1] $\beta_{\rm pl} \equiv p_{\rm gas}/p_{\rm B}$

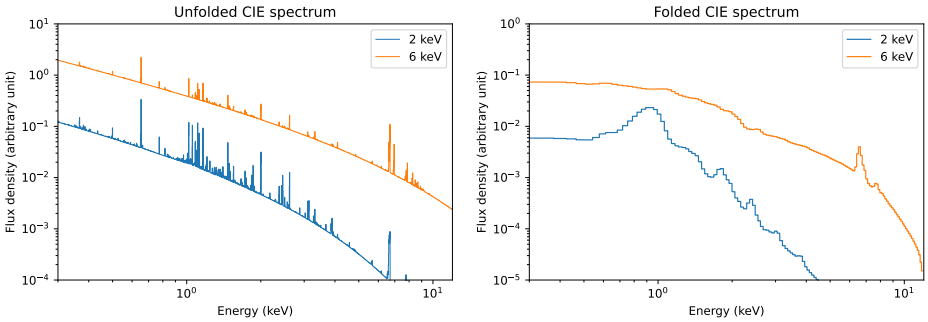

Figure 1.2: *Left*: CIE spectra for a 2 keV and a 6 keV plasma, respectively. The spectra are calculated based on the SPEXACT 3.06.01 database with a 0.3 proto-solar abundance (Lodders et al. 2009). *Right*: The same spectra as in the left panel but folded by the EPIC-pn instrumental response.

and excitation processes from highly ionized metal elements for the line emission. For low mass clusters where the temperature is relatively low, other processes such as recombination and two-photon emission are also important for continuum emission (see Kaastra et al. 2008 for a review on the thermal radiative processes). Examples of CIE spectra at temperatures of 6 keV and 2 keV are plotted in Fig. 1.2. The two spectra show different features, especially after being convolved with the instrumental responses (here *XMM-Newton* European Photon Imaging Camera (EPIC) pn for example). The main feature in a $kT = 2$ keV spectrum is the Fe L-shell complex around 1 keV energy, while in a $kT = 6$ keV spectrum, the main feature is the Fe He-α line at 6.7 keV.

In addition to the X-ray emission, which directly reflects the density and temperature of the ICM, the pressure of the ICM can be learned from the Sunyaev-Zeldovich (SZ) effect (Sunyaev & Zeldovich 1972), which is the distortion of the cosmic microwave background (CMB) due to its inverse Compton scattering with the ICM electrons.

1.1.1 X-ray instruments and observations

The current generation of X-ray missions adopt Wolter-I (Wolter 1952) grazing incidence optics for the mirror and use silicon charge-coupled device (CCD) arrays as the detector. The Wolter-I optics consist of a parabolic surface followed by a hyperbolic surface. This design allows a mirror module

to have multiple nested mirror shells to increase the collecting power to a few hundred cm^2 for X-rays below 2 keV energy. The CCD array can host millions of pixels with a pixel size of dozens of microns to cover a certain area of the sky. The disadvantage of CCD detectors is their relatively low energy resolution (see the right panel of Fig. 1.2 for example), which is unable to resolve individual lines.

For sources like galaxy clusters, due to the low photon flux, there will be no more than one photon collected by the detector at the same pixel location within a frame time. In this way, both the coordinate and energy of each individual collected photon can be measured, and these detectors are known as imaging spectrometers, such as the EPIC on *XMM-Newton* and the Advanced CCD Imaging Spectrometer (ACIS) on *Chandra*. Observations of galaxy clusters using X-ray imaging spectrometers allow us to have both spatial and spectral information of the ICM emission. With the hundred eV energy resolution of the CCD and the sub-arcmin spatial resolution of the telescopes, thermodynamic structures in both relaxed clusters and disturbed merging clusters have been well explored over the last two decades.

Alternatively, like other electromagnetic waves at lower frequencies, X-ray photons show wave properties. A diffraction grating behind the mirror can disperse the X-ray photons. The dispersed photons with different energy are then located at different positions on the detector array. This method can achieve a much higher spectral resolution $E/\Delta E$ of a few thousand for point-like sources. This type of instruments is therefore known as grating spectrometers, such as the two Reflection Grating Spectrometer (RGS) on *XMM-Newton*, the High Energy Transmission Grating (HETG) and the Low Energy Transmission Grating (LETG) on *Chandra*. For galaxy clusters, only the bright compact cores of relaxed clusters can be observed using grating spectrometers, whereas the observed spectral resolution is still degraded due to the diffuse nature of the ICM, and imaging is not possible with this type of technology.

The performance of the most widely used X-ray telescopes and the onboard imaging spectrometers are listed in Table 1.1.

1.2 Gas motions in the ICM

Throughout the ~ 10 Gyr lookback time since the first cluster formation, galaxy clusters grow by accretion of the intergalactic medium and hierar-

Table 1.1: Comparison of the most widely used X-ray telescopes and the onboard imaging spectrometer for the ICM study.

Telescope	HEW[a] ($''$)	Instrument	$A_{\rm eff}$[b] ($\rm cm^2$)	FoV	ΔE[c] (eV)
XMM-Newton	15	EPIC-MOS 1,2	500	$\varnothing = 30'$	150
		EPIC-pn	1300		
Chandra	0.5	ACIS-I	600*/300†	$16.9' \times 16.9'$	280
		ACIS-S	750*/400†	$8.3' \times 8.3'$	150
Suzaku	110	XIS 0,2,3	330	$18' \times 18'$	140
		XIS 1	370		

[a] Half energy width.
[b] At 1.5 keV.
[c] At 5.9 keV.
* After launch.
† In 2022.

chical mergers. Meanwhile, on smaller scales, the accretion of mass onto the supermassive black holes hosted by the central brightest cluster galaxies (BCGs) trigger energetic active galactic nuclei (AGN) outbursts. All these processes drive gas motions in the ICM, though with different observational features. This thesis mainly focuses on the gas motions on large scales and therefore we will not discuss the gas motions due to AGN feedback.

Fig. 1.3 shows the ICM turbulent velocity field in a numerical simulation (Vazza et al. 2017), where turbulence fills the entire volume inside the accretion shock. Most of the turbulence is solenoidal ($\nabla \cdot \vec{v} = 0$), while a small fraction is compressive ($\nabla \times \vec{v} = 0$). The compressive component is mostly in layers at different radii, which trace shocks, including outer cosmic accretion shocks and inner merging shocks.

1.2.1 Shocks and cold fronts as evidence of ICM dynamics

Major and minor mergers can both drive ICM bulk motions, but in different ways. Shocks and cold fronts are the two evident signatures of ICM bulk motions and are widely observed in both relaxed and merging systems (Markevitch & Vikhlinin 2007).

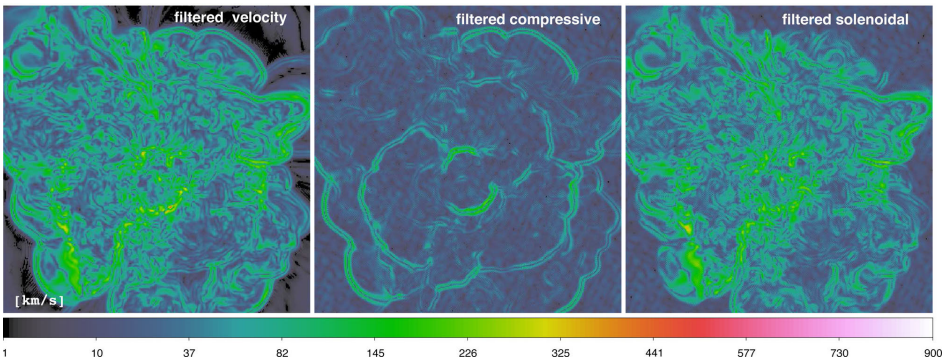

Figure 1.3: The ICM turbulent velocity field of a $M_{\rm tot} = 10^{14}\ M_{\odot}$ cluster in a cosmological simulation (Vazza et al. 2017). The box size is 5.8 Mpc^3. The *Middle* and *Right* panels show the compressive and solenoidal components, respectively. Image credit: Franco Vazza.

Major mergers are the collisions of two (or more) halos with mass ratio < 10, and are the most energetic events in the Universe, releasing $> 10^{64}$ erg energy. Gravitational potential energy is first converted to kinetic energy of the two halos. The collision velocity can be up to a few thousand km s^{-1}, exceeding the local sound speed (see Eq. 1.1). As a result, pairs of Mpc scale merging shocks are generated, see the innermost pair in the middle panel of Fig. 1.3 as an example in simulations. In the same process, if one of the subclusters has a dense cool core, an additional interface will be created between the decelerated post-shock flow and the core, which is named a cold front. Cold front is originally a meteorological terminology, representing the transition zone between warm air and cold air. In ICM astrophysics, it represents the subsonic and isobaric interface between ICM gas with two different temperatures. Bow shock - cold front patterns are frequently observed in merging systems, e.g. the Bullet Cluster (Markevitch et al. 2002), Abell 2146 (Russell et al. 2010, 2012) and Abell 3376 (Urdampilleta et al. 2018). Due to the longer thermal diffusion timescale compare to the pressure equilibrium timescale at the interface (Vikhlinin et al. 2001; Markevitch et al. 2003), the ICM shows clear stratification with cold dense gas on the one side and hot diluted gas on the other side.

Minor mergers (mass ratio > 10), which take place more frequently during the structure formation, drive bulk motions in different ways. When the impact factor is small, i.e. the subhalo directly falls into the major halo, a

similar bow shock - cold front pattern will be generated if the falling speed exceeds the local sound speed, e.g. M89 in the Virgo Cluster (Kraft et al. 2017). On the contrary, when the impact factor is large, i.e. the subhalo is flying by or falling through an orbital trajectory, if the major cluster has a dense cool core, the core will suffer from the gravitational perturbation from the subhalo. The perturbation is not strong enough to entirely pull the core out of the bottom of the gravitational well, but can displace the core and make it move around within the central region. A cold front is created between the displaced central cool gas and the ambient hot gas. This cold front will evolve to spiral shapes and is named a 'sloshing' cold front (Markevitch et al. 2001).

In addition to the obvious X-ray surface brightness (SB) discontinuities, major mergers and sloshing will also generate turbulence. Theoretical works (Schekochihin & Cowley 2006; Melville et al. 2016) and observations of different aspects (Ichinohe et al. 2017; Kraft et al. 2017; Zhuravleva et al. 2019) suggest that the magnetized ICM has a large effective Reynolds number, i.e. the ratio of kinetic energy to viscous damping in a fluid flow. The high Reynolds number implies the presence of turbulent motions in the ICM. Though there is not enough direct observational evidence (the indirect evidence and methods will be discussed later in Sect. 1.2.2), numerical simulations already show that ICM can be generated by cosmic accretion, mergers, and sloshing (Vazza et al. 2009; van Weeren et al. 2012; ZuHone et al. 2013; Nelson et al. 2014; Vazza et al. 2017).

1.2.2 Quantifying ICM gas motions

Different from some other variable astronomical objects, e.g. AGNs, variable stars, supernovae, etc., the timescales of different processes in the ICM are mostly $> 10^8$ yrs. Therefore, we are unable to observe the temporal evolution of the ICM. Quantifying ICM gas motions is based on imaging and spectroscopic analyses, i.e. studying the SB, emission lines and continuum properties. A detailed review on this topic is presented by Simionescu et al. (2019). In this section, we focus on the shock speed and turbulent velocity dispersions in the ICM.

Shock speed

From the shock Mach number definition $\mathcal{M}_{\rm shock} \equiv v_{\rm shock}/c_{\rm s}$, where $v_{\rm shock}$ is the shock speed and $c_{\rm s}$ the sound speed in the pre-shock region, quanti-

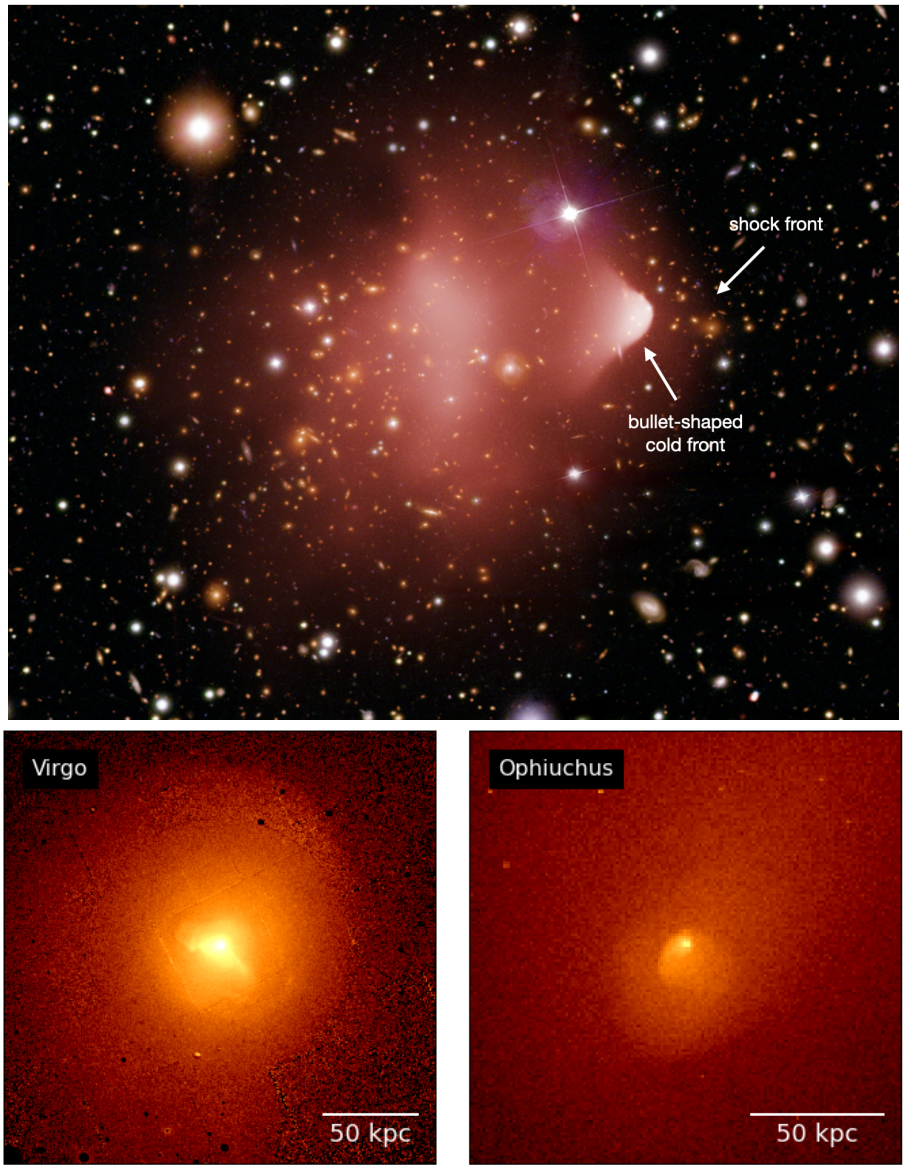

Figure 1.4: Gallery of shocks and cold fronts. *Top*: Optical and X-ray composite image of the Bullet Cluster, which shows a textbook bow shock - cold front pattern. Image credit: NASA/CXC/CfA/M.Markevitch et al./STScI; Magellan/U.Arizona/D.Clowe et al. *Bottom Reft* and *Bottom Right*: Sloshing cold fronts in the Virgo Cluster and the Ophiuchus Cluster, respectively. The two images are adapted from ZuHone & Su (2022) and are originally from Simionescu et al. (2010) and Giacintucci et al. (2020).

fying shock speed needs the measurements of $c_{\rm s}$ and $\mathcal{M}_{\rm shock}$. The former quantity depends on the temperature of the ICM,

$$c_{\rm s} = \sqrt{\frac{\gamma kT}{\mu m_{\rm p}}}, \tag{1.1}$$

where $\gamma = 5/3$ for an ideal gas. The shock Mach number can be quantified based the Rankine-Hugoniot condition (Macquorn Rankine 1870; Landau & Lifshitz 1959),

$$\mathcal{M}_{\rm shock} = \left[\frac{2C}{\gamma + 1 - C(\gamma - 1)}\right]^2, \tag{1.2}$$

where $C \equiv n_{\rm post}/n_{\rm pre}$, the density ratio across the shock. Alternatively, the temperature jump can also be a proxy of Mach number,

$$\frac{kT_{\rm post}}{kT_{\rm pre}} = \frac{(\gamma+1)/(\gamma-1) - C^{-1}}{(\gamma+1)/(\gamma-1) - C}, \tag{1.3}$$

where $kT_{\rm post}$ and $kT_{\rm pre}$ are the temperature in the post-shock and pre-shock regions, respectively.

The ICM density profile at a large radius can be approximated as a power law. Based on this, a practical way to measure the density jump of a spherical shock is using a double power-law density model to forward fit the surface brightness profile. The number density profile can be expressed as

$$n(r) = \begin{cases} C \times n_0 \left(\dfrac{r}{r_{\rm shock}}\right)^{-\alpha_1} & \text{when } r \leqslant r_{\rm shock}, \\ n_0 \left(\dfrac{r}{r_{\rm shock}}\right)^{-\alpha_2} & \text{when } r > r_{\rm shock}, \end{cases} \tag{1.4}$$

where n_0 the density normalization, $r_{\rm shock}$ the shock location, α_1 and α_2 the post and pre-shock power law indices, respectively. The corresponding surface brightness profile is

$$S(r) \propto \int_{-\infty}^{\infty} \left[n\left(\sqrt{l^2 + r^2}\right)\right]^2 {\rm d}l, \tag{1.5}$$

where l is the line-of-sight (LOS) coordinate. This method has several caveats that may lead to over- or underestimations of the density jump.

First, it can only be used for a shock where the temperatures of the two sides are both $\gtrsim 3$ keV, in which condition the soft band cooling function is approximately a constant across the shock. Second, the density profile in Eq. 1.4 is based on a spherically symmetric assumption. For real merging shocks, the geometry is more complicated and therefore the density jump could be underestimated especially when the shock plane is not parallel with the LOS. Third, due to the complex geometry, the zero point of r is usually hard to determine in merger systems, and the best-fit result of C is also sensitive to the starting point. Moreover, with only imaging study, a shock front cannot be directly distinguished from a cold front, which also shows a similar surface brightness jump. The observed temperature jumps are less sensitive to the merging geometry and can be used to distinguish shocks from cold fronts. The disadvantage of using temperature jumps for quantifying the shock Mach number is that it requires much more counts to have a robust temperature measurement.

Turbulent velocity dispersion

Quantifying a turbulent Mach number is more difficult than the shock Mach number. The direct way is to measure the turbulent Doppler line broadening. The *Hitomi* telescope first measured the turbulent broadening at the Fe XXV Heα lines in the Perseus Cluster core (Hitomi Collaboration et al. 2016), where the dispersion is < 200 km s^{-1}. Due to the loss of *Hitomi*, currently we do not have instruments for this method. With the performance of the current generation instruments, there are still several indirect ways to quantify the turbulent strength.

For cool core clusters, at the very center of the core region, the density is high enough to have a non-negligible optical depth for a few specific lines with large oscillation strengths, which will lead to resonant scattering of photons emitted from this region, resulting in a suppression of the line strength (Gilfanov et al. 1987). This resonant scattering effect is sensitive to the turbulent velocities, i.e. a higher velocity dispersion results in a lower optical depth. Therefore, the suppression of the line strength is an indicator of the turbulent velocities. Using the RGS grating spectrometer, works by Xu et al. (2002); Werner et al. (2009); de Plaa et al. (2012); Pinto et al. (2016) successfully applied this method on halos from group size to cluster size. See sect. 2 in Gu et al. (2018) for a review on this method.

The method of SB fluctuation power spectrum can also be used for estimating the turbulent velocity dispersions. The theoretical rationale of this

method is that numerical simulations show that for weak turbulence, the turbulent Mach number $\mathcal{M}_{\rm turb}$ is proportional to the fluctuations of ICM entropy or density (Gaspari & Churazov 2013; Gaspari et al. 2014),

$$\mathcal{M}_{\rm turb,1D} \propto \frac{\delta\rho}{\rho}. \tag{1.6}$$

Meanwhile, the perturbations of the density field result in SB fluctuations on top of the smoothing varying global cluster emission. Therefore, by computing the power spectrum of the SB fluctuation $P_{\rm 2D}$ and inferring the power spectra of the density fluctuation $P_{\rm 3D}$ through deprojection, one can estimate the three dimensional density fluctuation (Churazov et al. 2012)

$$A_{\rm 3D} \equiv \frac{\delta\rho}{\rho} = \sqrt{P_{\rm 3D}(k) 4\pi k^3}, \tag{1.7}$$

where k is the wavenumber representing a specific scale. Based on the unity slope in Eq. 1.6 (Zhuravleva et al. 2014b), the one dimensional turbulent velocity dispersion is therefore $\sigma_{v,\rm 1D} \equiv \mathcal{M}_{\rm turb,1D} \times c_{\rm s} = A_{\rm 3D} \times c_{\rm s}$.

1.3 Nonthermal views of galaxy clusters

In addition to the stellar component in the cluster galaxies and the thermal emission from the ICM, nonthermal diffuse emission is also detected.

In the γ-ray band, due to the limit of the capabilities of the current γ-ray satellites, the very high energy regime of the cluster field is still little explored. Some detections of excess emission were only reported in the field of the Coma Cluster using *Fermi* data (Ackermann et al. 2016; Xi et al. 2018; Adam et al. 2021; Baghmanyan et al. 2021).

At radio frequencies, the observations of cluster extended radio sources have achieved substantial progress over the past few decades. It turns out that, beside the ubiquitously observed tailed radio galaxies, which have a nature of AGN as the accelerator, other types of extended sources are observed in the fields of galaxy clusters, especially merging clusters. These radio sources have synchrotron nature and steep spectra with spectral index[2] $\alpha < -1$ (e.g. Giovannini et al. 2009; Feretti et al. 2012). Based on the location, morphology, polarization and spectral properties, extended cluster radio sources are classified as radio relics, radio halos and radio

[2] $S_\nu \propto \nu^\alpha$

phoenices, where radio relics and radio halos are the two types of most widely observed sources. An example of a galaxy cluster that hosts both radio relics and a radio halo, Abell 2744, is plotted in Fig. 1.5. This example illustrates the differences between radio relics and radio halos in terms of locations, morphologies, spectral properties and polarization properties. A review by van Weeren et al. (2019) presents detailed studies of extended cluster radio sources.

1.3.1 Radio relics

Radio relics, also termed as radio *gischt* (sea spray in German) in early days, are located in the peripheries of clusters. The textbook radio relic in CIZA J2242.8+5301 (the Sausage Cluster) illustrates well the typical properties of radio relics: over one Mpc linear size, spectral flattening at the outer edge, high polarization degree, perpendicularity between polarization electric field vectors and the relic orientation (e.g. van Weeren et al. 2010; Stroe et al. 2013; Hoang et al. 2017; Di Gennaro et al. 2018, 2021). While the Sausage relic is in a perfect arc-like shape, other radio relics show more complex morphology, e.g. the relics in Abell 3667 (Rottgering et al. 1997; de Gasperin et al. 2022), Abell 3376 (Bagchi et al. 2006; Chibueze et al. 2022) and Abell 2256 (Clarke & Ensslin 2006; Kale & Dwarakanath 2010; van Weeren et al. 2012; Rajpurohit et al. 2022). Some galaxy clusters even host a pair of radio relics on the opposite sides of the cluster, e.g. Abell 3667, Abell 3376, Abell 1240 (Bonafede et al. 2009), etc.

1.3.2 Radio halos

Radio halos are located at the center of clusters, overlapping with the ICM emission. Their emissivity is lower than radio relics. Radio halos are unpolarized and have roundish morphologies. The spectral variation across the radio halo is not clear yet. While some sources show uniform spectral indices e.g. the radio halo in the Toothbrush Cluster (van Weeren et al. 2016a; Rajpurohit et al. 2020), other sources show local spectral variation, e.g. the radio halos in Abell 2744 (Rajpurohit et al. 2021) and in the Coma Cluster (Bonafede et al. 2022).

Based on the linear size, there are two subclasses, giant radio halos and mini radio halos. The radii of mini radio halos are usually ~ 100 kpc and up to 300 kpc (e.g. RX J$1347.5-1145$, Gitti et al. 2007), while the radii of giant radio halos can be over 1 Mpc. Though they are in distinct sizes, mini

radio halos and giant radio halos have similar orders of magnitude radio power, in which case the two populations are distinguished in the power - radius diagram (Cassano et al. 2008).

1.4 Connecting the nonthermal to the thermal properties

To understand the origins of the cluster extended radio sources, i.e. the cosmic rays (CRs) permeating the ICM, the key is to know the acceleration mechanism and what processes in the structure formation accelerate the CRs. Due to energy losses through synchrotron and inverse Compton emission, the life time of CR is $< 10^8$ yrs, which means that in-situ acceleration mechanisms are required to form the Mpc scale radio sources (Jaffe 1977).

1.4.1 X-ray - radio associations

Radio relics

The idea that extended radio sources in the cluster peripheries are accelerated by shocks is first proposed by Ensslin et al. (1998) and Miniati et al. (2000). The first concrete evidence of a radio relic - X-ray shock association was found in Abell 3667 (Finoguenov et al. 2010). Since then, X-ray shocks at the locations of radio relics have been reported in over ten clusters (e.g. Akamatsu et al. 2015; Eckert et al. 2016; Botteon et al. 2016; Urdampilleta et al. 2018), by which the shock acceleration scenario is therefore confirmed. For many of the radio relics, due to the large projected radii, the ICM density at the relic locations are quite low, which poses difficulty for the detection of the corresponding shock. Moreover, distinguishing a shock front from a cold front requires large number of counts on the low density side for spectral analysis. Shallow X-ray observations could draw a false conclusion, see **Chapter 3** for an example of ZwCl 2341+0000.

The established shock - radio relic connection helps us to better understand the merger configuration, e.g. a double-relic implies a small angle between the merger axis and the sky plane. Meanwhile, numerical simulations of shocks try to explain the observed irregularity of radio relics, e.g. the ring-like relic in Abell 3376 and the filamentary structures in the relic in Abell 2256. The simulation of Skillman et al. (2013) shows the complexity of the shock plane, where the Mach number and magnetic field strength is not uniform. A different viewing angle will result in a different observed

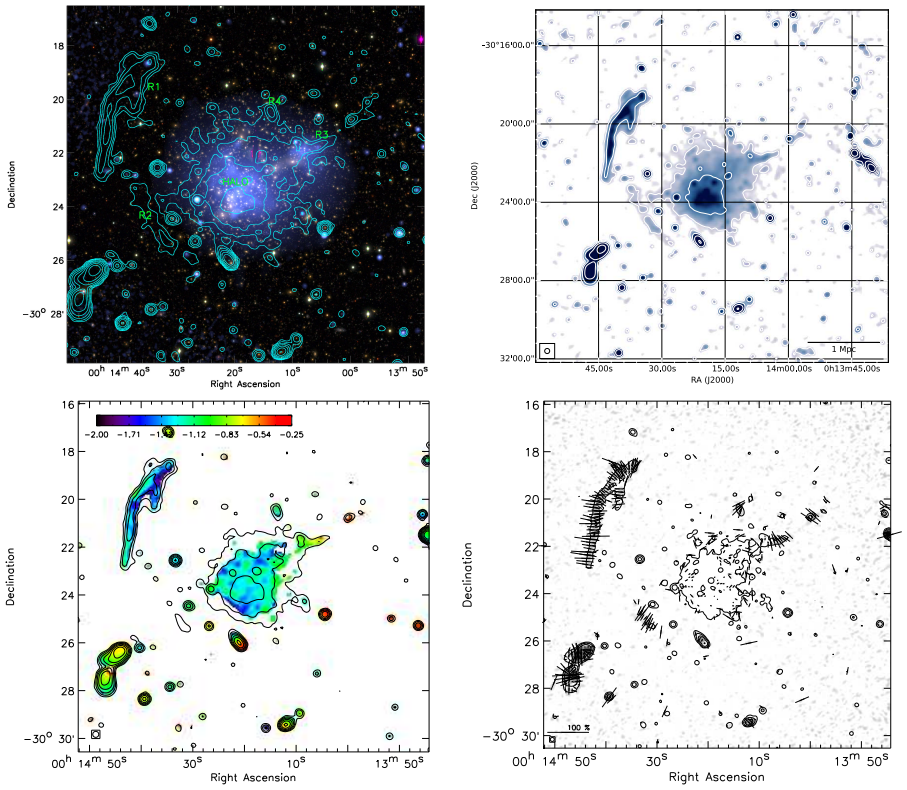

Figure 1.5: Observational properties of radio relics and radio halos, taking Abell 2744 as an example. The figures are adopted from Pearce et al. (2017). *Top left*: The X-ray (blue) and optical composite image overlaid with radio contours. *Top right*: JVLA 1.5 GHz image tapered to $15''$ resolution. *Bottom left:* Spectral map between 1.5 GHz and 3.0 GHz. *Bottom right:* Polarization map of the S band (2 – 4 GHz).

radio morphology. A recent simulation by Dominguez-Fernandez et al. (2021) shows that the shock propagating in a turbulent medium can produce filamentary radio emission.

Radio halos

Radio halos are located at the center of galaxy clusters. The surface intensity of radio halos fades away radially, similar to the SB of the ICM. Analysis of the point-to-point correlation between the radio and the X-ray SB have been performed on many radio halos (e.g. Govoni et al. 2001; Schaal et al. 2016; Rajpurohit et al. 2018; Botteon et al. 2020; Bonafede et al. 2022). These studies find that the SB in the two bands are overall correlated, and the slopes are different between giant radio halos and mini radio halos. In giant radio halos, the slope tends to be sublinear, which means the intensity variation in the radio is shallower than in the X-rays, while mini radio halos show the opposite trend.

Several radio halos have edges associated with X-ray shock or cold fronts. The edge - shock associations are in giant radio halos, e.g. the Coma Cluster (Brown & Rudnick 2011), the Bullet Cluster (Shimwell et al. 2014), Abell 2034 (Shimwell et al. 2016), the Toothbrush Cluster(van Weeren et al. 2016a), as well as a recent new candidate in ClG 0217+70 (see **Chapter 4**). Different from the shock - relic associations, the shocks at the radio halo edges are much closer to the cluster center. It is not yet clear whether the radio edge is formed due to shock acceleration. Associations between cold fronts and radio halo edges have also been reported. They are mainly found in mini halos, where part of the mini radio halo is confined by the sloshing cold fronts, e.g. the Perseus Cluster (Gitti et al. 2002) and Abell 2029 (Govoni et al. 2009). It is also not yet clear whether the subsonic motion of the sloshing cold fronts and the turbulent motions due to the sloshing are responsible for (mildly) accelerating the central CRs.

The occurrence of giant radio halos is also connected to the dynamic status of the cluster. Cassano et al. (2010) studied the relation between X-ray morphology and radio halo occurrence and found that dynamically disturbed clusters are statistically more likely to host a giant radio halo. This bimodality suggests that the turbulence generated by major mergers is the most promising source for accelerating CRs.

1.4.2 Accelerations mechanisms by gas motions

Shock acceleration

CR acceleration in the shock plane is usually described by the diffusive shock acceleration (DSA) theory (Bell 1978a,b; Drury 1983; Blandford & Eichler 1987; Jones & Ellison 1991), where the acceleration process is also known as the first order Fermi process (Fermi 1949). In the DSA theory, when a particle moves from the upstream to the downstream, if the diffusion length is much larger than the thickness of the shock, it will be scattered back and forth across the shock multiple times and will gain energy each time. The accelerated CRs have a power law distribution in the momentum space, $N(p) \propto p^{-\delta}$. Based on the relation between the power law index of CR momentum and the radio spectral index $\alpha = (1-\delta)/2$, the injected spectral index by the DSA is

$$\alpha_{\rm inj} = \frac{1}{2} - \frac{\mathcal{M}^2_{\rm shock}+1}{\mathcal{M}^2_{\rm shock}-1}. \tag{1.8}$$

Eq. 1.8 can be applied to spatially resolved radio relics for Mach number estimation. For low resolution radio observations, $\alpha_{\rm inj}$ is usually converted from the integrated spectral index of the entire radio relic, $\alpha_{\rm inj} = \alpha_{\rm int} + 0.5$ (Kardashev 1962). However, this injected and integrated spectral index relation is disfavored by recent observations (Stroe et al. 2013; Hoang et al. 2021, also in **Chapter 3**).

One problem of applying DSA to radio relics is that the merging shocks have a low Mach number, $\mathcal{M}_{\rm shock} \lesssim 3$, where the acceleration efficiency is not sufficient for the observed relic power (Pinzke et al. 2013). The most viable solution is the reacceleration scenario (Markevitch et al. 2005; Kang et al. 2012; Pinzke et al. 2013). In this scenario, due to a preexisting seed population, the weak shock can easily accelerate the aged CR to a Lorentz factor $\gamma \sim 10^4$. The reacceleration scenario can also explain the irregularity of the relic morphology. A recent simulation by ZuHone et al. (2021) shows that the large scale ICM motions can transport aged CRs ejected by AGNs to a large radius. Shocks light these aged CRs up to radio relics and the morphology follows the distribution of the seed population.

Turbulent acceleration

Due to the high $\beta_{\rm pl}$ of the ICM, the turbulence on large scales is purely hydrodynamic. Once the energy cascade reaches the Alfvén scale $l_{\rm A}$, the

hydrodynamic turbulence becomes magnetohydrodynamic (MHD) turbulence. MHD turbulence can accelerate CRs through the second order (stochastic) Fermi processes (Fermi 1949), where the momentum change is a second order phenomenon. In these processes, particles can gain or lose energy in each scatter and the probability of gaining energy is higher than losing energy. The second order Fermi processes are milder than the first order Fermi processes. There are several proposed detailed MHD turbulent acceleration mechanisms for the ICM-like plasma, e.g. resonant transit-time damping acceleration and non-resonant acceleration by large scale compressive motions (e.g. Brunetti & Lazarian 2007, 2011).

Due to the mild acceleration efficiency, turbulent acceleration is also unlikely to accelerate CRs from the thermal pool directly. In other words, the MHD turbulence can only reaccelerate the seed CR populations to the energies that produce the observed radio halo emission.

1.5 This thesis

Though we already built up a general picture that radio relics trace cluster merging shocks and radio halos are the results of the subsequent turbulence, there are still many questions unsolved in this field. What is the origin of the discrepancy in shock Mach numbers from X-rays and radio? Is a radio relic always a tracer of merging shocks? Before this thesis work, there was one exception known in the double relic cluster ZwCl 2341+0000, where only 2/3 of the southern relic was associated with an X-ray SB jump (Ogrean et al. 2014). If the edge is a shock and it reaccelerates the CRs for the relic, where does the remaining 1/3 of the relic come from? What parameters in the ICM build up the radio halo power - mass correlation? Is the turbulent Mach number - radio halo power correlation (Eckert et al. 2017) satisfied in samples of different mass ranges and observation frequencies? This thesis aims to better understand these questions starting from X-ray observations. It covers works from case studies to sample study and topics from merging shocks to ICM turbulence. This thesis is structured as follows.

In **Chapter 2**, the detailed analysis of *XMM-Newton* and *Suzaku* observations of Abell 3411 is presented. The cluster Abell 3411 hosts a radio relic that shows a direct evidence of shock reacceleration, where a mild SB jump at the relic location was also detected by *Chandra* (van Weeren et al. 2017). Thanks to the high sensitivity of *XMM-Newton* and the low instru-

mental background of *Suzaku*, we successfully measured the ICM temperature jump across the SB jump and confirmed its shock nature. Meanwhile, a novel method of modeling the soft proton background of the *XMM-Newton* EPIC was presented. This method can successfully reduce the systematics of the soft proton in spectral fitting, especially in the ICM temperature regime of $kT > 4$ keV.

Chapter 3 presents the deep (206 ks) *Chandra* observations of the double radio relic cluster ZwCl 2341+0000 to solve the puzzle of shock - relic connection. The deep observations reveal that the nature of a shock candidate is actually a disrupted cool gas clump. This discovery emphasizes that the shock nature of a SB jump needs to be confirmed with thermodynamic properties of the ICM. The exact location of this shock is suggested by an updated radio spectral index map, where the ICM emission is faint and we can only put a lower limit on the Mach number. In the deep observations, we also discovered a unique cone-like subcluster core remnant. After comparing with numerical simulations, we interpret that this conic structure is in a transition stage between an early blunt-body shape and a late flaring stage, which were previously observed in other systems.

Chapter 4 reports a serendipitous discovery of a galaxy cluster at $z = 0.18$, which is measured using the 6.7 keV Fe XXV Heα lines. The redshift of this cluster was incorrectly estimated as $z = 0.066$ using highly extincted optical data (Brown et al. 2011). With the updated redshift, the radio sources in this cluster show magnificent properties. Among them, one radio relic is located at $r > r_{200}$ and with a linear size > 2 Mpc. The X-ray image also exhibits two SB edges, suggesting a new candidate of radio halo edge - X-ray shock associations. In the subsequent LOFAR radio analysis (Hoang et al. 2021), the two outermost radio relics have a span of 5 Mpc, making this cluster one of the largest separated radio halo - relic system.

Chapter 5 studies the Planck SZ cluster sample in the Low Frequency Array (LOFAR) Two-meter Sky Survey DR2 footprint and focuses on the connections between the ICM properties and the radio halo properties. In this chapter, morphological parameters are calculated as the indicators of cluster dynamic states. Meanwhile, turbulent velocity dispersions are estimated using SB fluctuation power spectra as described in Sect. 1.2.2. Together with the known ICM density profile and temperature, we computed the turbulent dissipation flux in the volumes of the radio halos and find they are correlated with the 150 MHz radio halo power in a unity slope.

This correlation suggests a tight connection between the radio halo power and two ICM properties, i.e. the gas mass in the radio halo volume and the local sound speed determined by the ICM temperature.

1.6 Future prospects

In 2020s, the *XRISM* mission[3] will reopen the window of high resolution imaging X-ray spectroscopy. The imaging spectrometer Resolve will have a < 7 eV spectral resolution to measure the Doppler broadening due to velocity dispersions. Limited by its large point spread function (PSF) size, only nearby high mass clusters are proper candidates for observations. Nevertheless, using a structure function method (e.g. ZuHone et al. 2016), the amplitude and injection scale of the turbulent spectrum can be measured. The high spectral resolution also allow us to better disentangle multitemperature ICM using line diagnostics, by which the post-shock temperature can be better measured.

In one decade, the *Athena* mission will have unprecedented capabilities in both sensitivity and spectral resolution. The high resolution spectrometer X-IFU has a 2.5 eV resolution and will allow us to further explore the velocity structures in the ICM (Roncarelli et al. 2018). Meanwhile, the other instrument WFI has a $40' \times 40'$ field of view. Together with the 10000 cm^2 soft band effective area and the $< 10''$ PSF size, the density fluctuation in the cluster outskirts will be exploited in detail (Bulbul et al. 2019).

[3] `https://xrism.isas.jaxa.jp`

2 X-ray study of the merging galaxy cluster Abell 3411-3412 with *XMM-Newton* and *Suzaku*

X. Zhang, A. Simionescu, H. Akamatsu, J.S. Kaastra, J. de Plaa and R.J. van Weeren

(Astronomy & Astrophysics, Volume 642, A89)

Abstract

Context: Previous *Chandra* observations of the Abell 3411-3412 merging galaxy cluster system revealed an outbound bullet-like sub-cluster in the northern part and many surface brightness edges at the southern periphery, where multiple diffuse sources are also reported from radio observations. Notably, a southeastern radio relic associated with fossil plasma from a radio galaxy and with a detected X-ray edge provides direct evidence of shock re-acceleration. The properties of the reported surface brightness features have yet to be constrained from a thermodynamic viewpoint.

Aims: We use the *XMM-Newton* and *Suzaku* observations of Abell 3411-3412 to reveal the thermodynamical nature of the previously reported re-acceleration site and other X-ray surface brightness edges. We also aim to investigate the temperature profile in the low-density outskirts with *Suzaku* data.

Methods: We performed both imaging and spectral analysis to measure the density jump and the temperature jump across multiple known X-ray surface brightness discontinuities. We present a new method to calibrate the vignetting function and spectral model of the *XMM-Newton* soft proton background. Archival *Chandra*, *Suzaku*, and *ROSAT* data are used to estimate the cosmic X-ray background and Galactic foreground levels with improved accuracy compared to standard blank sky spectra.

Results: At the southeastern edge, temperature jumps revealed by both *XMM-Newton* and *Suzaku* point to a $\mathcal{M} \sim 1.2$ shock, which agrees with the previous result from surface brightness fits with *Chandra*. The low Mach number supports the re-acceleration scenario at this shock front. The southern edge shows a more complex scenario, where a shock and the presence of stripped cold material may coincide. There is no evidence for a bow shock in front of the northwestern "bullet" sub-cluster. The *Suzaku* temperature profiles in the southern low-density regions are marginally higher than the typical relaxed cluster temperature profile. The measured value $kT_{500} = 4.84 \pm 0.04 \pm 0.19$ keV with *XMM-Newton* and $kT_{500} = 5.17 \pm 0.07 \pm 0.13$ keV with *Suzaku* are significantly lower than previously inferred from *Chandra*.

2.1 Introduction

Galaxy clusters are the largest gravitationally bound objects in the Universe. They grow hierarchically by merging with sub-clusters and accreting matter from the intergalactic medium. During mergers, gravitational energy is converted to thermal energy in the intracluster medium (ICM) via merging-induced shocks and turbulence. Shocks compress and heat the ICM, which exhibits surface brightness and temperature jumps. As a consequence, the pressure is discontinuous across a shock front. In galaxy clusters, there is another type of surface brightness discontinuity, namely 'cold fronts', which are produced by the motion of relatively cold gas clouds in the ambient high-entropy gas (Markevitch & Vikhlinin 2007). In merger systems, cold fronts indicate sub-cluster cores under disruption. It is hard to determine whether a surface brightness discontinuity is a shock or a cold front based on imaging analyses alone, especially when the merging scenario is complicated or still unclear. On the other hand, the temperature and pressure profiles across shocks and cold fronts show different trends. For a cold front, the denser side of the discontinuity has a lower temperature, such that the pressure profile remains continuous. Hence, temperature measurements from spectroscopic analysis are necessary to distinguish shocks from cold fronts.

Besides heating and compressing the ICM, shocks can accelerate a small proportion of particles into the relativistic regime as cosmic ray protons (CRp) and electrons (CRe). The interaction of CRe with the magnetic field in the ICM leads to synchrotron radiation that is observable at radio wavelengths as radio relics. Radio relics are often observed in galaxy cluster peripheries with elongated (0.5 to 2 Mpc) arched morphologies and high polarisation ($\gtrsim 20\%$, Ensslin et al. 1998). The basic idea of the shock acceleration mechanism is diffusive shock acceleration (DSA, Blandford & Eichler 1987; Jones & Ellison 1991). According to DSA theory, the acceleration efficiency depends on the shock Mach number $\mathcal{M}$. The Mach number can be derived either from X-ray observations using the Rankine-Hugoniot jump condition (Landau & Lifshitz 1959) or from the radio injection spectral index $\alpha_{\rm inj}$ on the assumption of DSA. Since the first clear detection of an X-ray shock co-located with the northwestern radio relic in Abell 3667 (Finoguenov et al. 2010), around 20 X-ray–radio coupled shocks have been found (see van Weeren et al. 2019 for a review). However, there are still some remaining questions surrounding the observational results so far.

First, both X-ray and radio observations suggest low Mach numbers for cluster-merging shocks ($\mathcal{M} < 4$). In weak shocks, particles from the thermal pool are less efficiently accelerated due to the steep injection spectrum (Kang & Jones 2002) and less effective thermal-leakage-injection (Kang et al. 2002). The re-acceleration scenario has been proposed to alleviate this problem (Markevitch et al. 2005). With the presence of pre-existing fossil plasma, the acceleration efficiency would be highly increased (Kang & Jones 2005; Kang & Ryu 2011). Second, the Mach numbers derived from X-ray observations are not always identical to those from radio observations. This could be explained from both sides. The X-ray estimations from surface brightness or temperature jumps may suffer from projection effects (Akamatsu et al. 2017). In radio, when using the integrated spectral index $\alpha_{\rm int}$ to calculate Mach numbers, the simple approximation that $\alpha_{\rm int} = \alpha_{\rm inj} + 0.5$ (Kardashev 1962; Ensslin et al. 1998) would be incorrect when the underlying assumptions fail (Kang 2015; Stroe et al. 2016). The systematic errors associated to both methods need to be studied thoroughly before we can ascribe the discrepancy to problems in DSA theory.

Abell 3411-3412 is a major merger system where the first direct evidence of the re-acceleration scenario was observed (van Weeren et al. 2017). From the dynamic analysis with optical samples, it is a probable binary merger at redshift $z = 0.162$, about 1 Gyr after the first passage. The two sub-clusters have comparable masses of $\sim 1 \times 10^{15} M_{\odot}$. Later, Golovich et al. (2019b) increased the optical sample from 174 to 242 galaxies and confirmed the redshift. From the same dataset, recently, Andrade-Santos et al. (2019) use the $Y_X - M$ scaling relation to find $r_{500} \sim 1.3$ Mpc, $kT = 6.5 \pm 0.1$ keV, and $M_{500} = (7.1 \pm 0.7) \times 10^{14} M_{\odot}$, which is much lower than the result from the previous dynamic analysis. Based on the *Chandra* X-ray flux map, the core of one sub-cluster is moving towards the northeast and shows bullet-like morphology while another sub-cluster core has been entirely stripped during the previous passage. From radio images, at least four 'relics' are located at the southern periphery of the system (van Weeren et al. 2013; Giovannini et al. 2013). The most northwestern of these four is associated with a radio galaxy, where the spectral index decreases along the radio jet and starts to increase at a certain location of the relic. The flattening edge is co-located with an X-ray surface brightness discontinuity. All the evidence points to a scenario in which CRes lose energy via synchrotron and inverse Compton radiation in the jet, and then are re-accelerated when crossing the shock. The analysis by van Weeren et al. (2017) shows the Mach num-

ber from radio observation is $\mathcal{M}_{\rm radio} = 1.9$, and the compression factor of the shock from the X-ray surface brightness profile fitting is $C = 1.3 \pm 0.1$, corresponding to $\mathcal{M}_{\rm SB} = 1.2$. Later Andrade-Santos et al. (2019) report that the compression factor at this discontinuity based on *Chandra* data is $C = 1.19^{+0.21}_{-0.13}$. Additionally, these latter authors provide the temperature measurements of both pre-shock and post-shock regions. However, they use large radii sector (annulus) regions to extract spectra, which makes the temperature ratio biased by the ICM far away from the shock location. Golovich et al. (2019b) suggest this shock could be produced by an optically poor group. Besides the southwest shock, Andrade-Santos et al. (2019) report a south surface brightness discontinuity as a cold front from the core debris of the sub-cluster Abell 3412; a potential surface brightness discontinuity in front of the southeast shock; and a bow shock in front of the 'bullet' with $\mathcal{M}_{\rm SB} = 1.15^{+0.14}_{-0.09}$.

In this paper, we analyse archival *XMM-Newton* and *Suzaku* data in order to constrain the thermodynamical property of the reported shock and to characterise the other X-ray surface brightness discontinuities. The paper is organised as follows. In Sect. 2.2, we describe the data reduction processes. In Sects. 2.3 and 2.4, we describe imaging and spectral analysis methods, selection regions, model components, and systematic errors. We present results in Sect. 2.5. We discuss and interpret our results in Sect. 2.6. We summarise our results in Sect. 2.7. We assume $H_0 = 70$ km s^{-1} Mpc^{-1}, $\Omega_{\rm m} = 0.3$, and $\Omega_\Lambda = 0.7$. At the redshift $z = 0.162$, $1'$ corresponds to 167.2 kpc.

2.2 Data reduction

2.2.1 XMM-Newton

We analysed 137 ks of *XMM-Newton* European Photon Imaging Camera (EPIC) archival data (ObsID: 0745120101) for this target. The *XMM-Newton* Science Analysis System (SAS) v17.0.0 is used for data reduction. MOS and pn event files are obtained from the observation data files with the tasks `emproc` and `epproc`. The out-of-time event file of pn is produced by `epproc` as well.

This observation suffers from strong soft proton contamination. To minimise the contamination of soft proton flares, we adopt strict good time interval (GTI) filtering criteria. For each detector, we first bin the 10 – 12

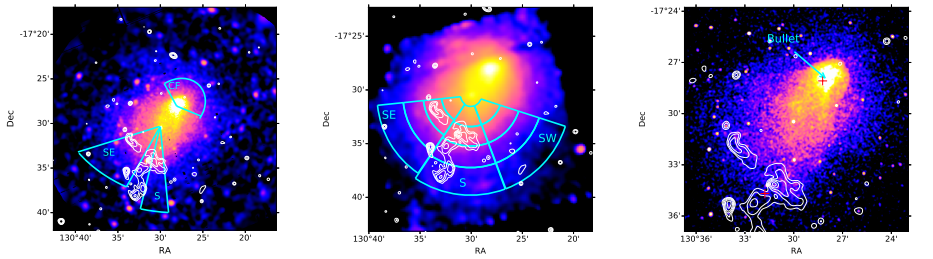

Figure 2.1: Smoothed flux image of Abell 3411 combined from 1.2 – 4.0 keV *XMM-Newton* EPIC CCDs (top left), 0.7 – 7.0 keV *Suzaku* XIS CCDs (top right), and 1.2 – 4.0 keV *Chandra* ACIS-I (bottom). Particle background and vignetting effect have been corrected. White contours are GMRT 610 MHz radio intensity. *XMM-Newton* and *Suzaku* analysis regions are plotted with cyan sectors. The locations of two BCGs are plotted with red crosses in the *Chandra* image. The coordinates of the BCGs are obtained from Golovich et al. (2019a).

keV light curve in 100 s intervals. We take the median value of the histogram as the mean flux of the source. All bins with count rate more than $\mu + 1\sigma$ are rejected, where the σ is derived from a Poisson distribution. To exclude the contamination of some extremely fast flares, we then bin the residual 10 – 12 keV light curve in 20 s intervals and reject bins with a count rate of more than $\mu + 2\sigma$. After GTI filtering, the clean exposure time of MOS1, MOS2, and pn are 89 ks, 97 ks, and 74 ks, respectively. For both imaging and spectral analysis, we select single to quadruple MOS events (`PATTERN<=12`) and single to double pn events (`PATTERN<=4`).

Particle backgrounds are generated from integrated Filter Wheel Closed (FWC) data [1] 2017v1. The FWC spectra of MOS are normalised using the unexposed area as described by Kuntz & Snowden (2008). The normalisation factors of MOS1 and MOS2 FWC spectra are 0.97 and 0.98, respectively. For pn, there is no 'clean' out-of-field-of-view (FOV) area (see Appendix 2.A). Therefore we normalise the integrated FWC spectrum using the FWC observation in revolution 2830, which was performed six months after our observation and is the closest FWC observation time. The normalisation factor of the integrated pn FWC spectrum is 0.82.

[1] `https://www.cosmos.esa.int/web/xmm-newton/filter-closed`

2.2.2 Suzaku

Abell 3411 was observed by Suzaku for 127 ks (ObsID: 809082010). A $21'$ offset area was observed for 39 ks (ObsID: 809083010). We use standard screened X-ray Imaging Spectrometer (XIS) event files for analysis. Two clocking mode (5×5 and 3×3) event lists are combined. Additionally, geomagnetic cut-off rigidity (COR) > 8 selection is applied to filter the event files and generate the non-X-ray background (NXB). The latest recommended recipe for removing flickering pixels [2] is applied to both observation and NXB event files. After COR screening, the valid source exposure time is 105 ks for XIS0, and 108 ks for XIS1 and XIS3. The NXB spectra are generated using the task `xisnxbgen` (Tawa et al. 2008) and are subtracted directly. The normalisation of NXB spectra is scaled by the 10 – 14 keV count rates. To estimate the systematic error contributed by the NXB in the spectral analysis, we assume a fluctuation of 3% around the nominal value (Tawa et al. 2008).

The *Suzaku* XIS astrometry shift could be as large as $50''$ (Serlemitsos et al. 2007). To measure the offset of our observation, we first make a combined 0.7 – 7.0 keV XIS flux map to detect point sources and then compare the XIS coordinates with EPIC coordinates from the 3XMM-DR8 catalogue (Rosen et al. 2016). We follow the instruction[3] to correct the vignetting effect. Only four point sources are detected by `wavdetect` in the CIAO package. The mean XIS RA offset is $25.0 \pm 0.3''$ to the east, and the mean Declination offset is $6.8 \pm 0.3''$ to the south.

2.2.3 Chandra

We use the same *Chandra* dataset as van Weeren et al. (2017). Event files, as well as auxiliary files, are reproduced by task `chandra_repro` in the Chandra Interactive Analysis of Observations (CIAO) package v4.10 with `CALDB` 4.8.0. We use `merge_obs` to merge all observations and create a 1.2 – 4.0 keV flux map. Stowed event files are used as particle backgrounds. The normalisations are scaled by the 10 – 12 keV band count rate of each observation.

The observation IDs, instruments, pointing coordinates, and clean exposure times of the observations taken with all three satellites are listed in Table 2.1.

[2] `https://heasarc.gsfc.nasa.gov/docs/suzaku/analysis/xisnxbnew.html`
[3] `https://heasarc.gsfc.nasa.gov/docs/suzaku/analysis/expomap.html`

Table 2.1: Observation information.

Telescope	ObsID	Instrument	Pointing Coordinates (RA, Dec)	Valid Exp. (ks)
XMM-Newton	0745120101	EPIC-MOS1	08:41:55, -17:28:43	89
		EPIC-MOS2		97
		EPIC-pn		74
Suzaku	809082010	XIS 0	08:42:03, -17:34:12	105
		XIS 1		108
		XIS 3		108
	809083010 (Offset)	XIS 0	08:43:06, -17:19:34	32
		XIS 1		32
		XIS 3		32
Chandra	13378	ACIS-I	08:42:05, -17:32:16	10
	15316		08:42:03, -17:29:53	39
	17193		08:42:01, -17:29:56	22
	17496		08:42:04, -17:29:02	32
	17497		08:42:01, -17:29:19	22
	17583		08:42:01, -17:29:56	32
	17584		08:42:02, -17:29:29	33
	17585		08:42:01, -17:29:19	24

2.3 Imaging analysis

We used the *XMM-Newton* 1.2 – 4.0 keV band for surface brightness analysis. The vignetting-corrected exposure maps were generated by the task `eexpmap`. Pixels with less than 0.3 of the maximum exposure value were masked by `emask` and then excluded. Because half of the photons from mirrors 1 and 2 are deflected by the RGS system, and the quantum efficiency of MOS is different from that of pn, we needed to scale the MOS exposure maps to make the MOS fluxes match the pn flux. We first derived the radial surface brightness profiles of the three detectors with unscaled exposure maps. The selection region is a circle centred at the pn focal point. We fitted $0' < r < 6'$ MOS-to-pn surface brightness ratios with a constant model. The ratios are 0.37 and 0.38 for MOS1 and MOS2, respectively. We combined the net count maps and scaled exposure maps from three detectors to produce a flux map. The particle-background-subtracted, vignetting-corrected, smoothed image is shown in Fig. 2.1. We excluded point sources before we extracted the surface brightness profiles. The coordinates of point sources were obtained from the 3XMM-DR8 catalogue (Rosen et al. 2016) and checked by visual inspection. The exclusion shape of each point source was generated by the `psfgen` in SAS with the PSF model `ELLBETA`.

We extracted surface brightness profiles along four regions, which are marked on the *XMM-Newton* flux map in Fig. 2.1. The first selection region (the southwest region) is the previously reported shock (van Weeren et al. 2017). From the *XMM-Newton* flux map, this discontinuity is unlikely to be seen by the naked eye. With the help of the *Chandra* flux map, we are able to define an elliptical sector whose side is parallel to the discontinuity. The second region (south) is crossing the south discontinuity seen in the *Chandra* flux map (Andrade-Santos et al. 2019) as well as a diffuse radio emission. The third one (cold front) stretches along the direction of the bullet and probably hosts a bow shock. The last one is the bullet itself. We set the region boundary carefully to be parallel to the surface brightness edge.

We extracted surface brightness profiles from both *XMM-Newton* and *Chandra* datasets. We used a projected double power-law density model to

fit discontinuities, whose unprojected density profile is

$$n(r) = \begin{cases} C n_{\rm edge} \left(\dfrac{r}{r_{\rm edge}} \right)^{-\alpha_1} & \text{When } r \leqslant r_{\rm edge}, \\ n_{\rm edge} \left(\dfrac{r}{r_{\rm edge}} \right)^{-\alpha_2} & \text{When } r > r_{\rm edge}, \end{cases} \tag{2.1}$$

where C is the compression factor at the shock or cold front, and $r_{\rm edge}$ and $n_{\rm edge}$ are the radius and the density at the edge, respectively. We assume the curvature radius along the line of sight is equal to the average radius of the surface brightness discontinuity (i.e. the ellipticity along the third axis is zero). The projected surface brightness profile is

$$S(r) = \int_{-\infty}^{\infty} n^2 \left(\sqrt{z^2 + r^2} \right) {\rm d}z + S_{\rm bg}, \tag{2.2}$$

where z is the coordinate along the line of sight, and $S_{\rm bg}$ is the surface brightness contributed by the X-ray background. For *Chandra*, we measure $S_{\rm bg} = 7 \times 10^{-7}$ count s^{-1} cm^{-2} arcmin^{-2} from the front-illuminated ACIS-S chips. For XMM-Newton, this value is more difficult to properly estimate. Because soft protons are less vignetted than photons, we can see an artificial surface brightness increases beyond $10'$. We therefore avoid regions located beyond $10'$ from the focal point. C-statistics (Cash 1979) is adopted to calculate the likelihood function for fitting.

2.4 Spectral analysis

To study the thermodynamic structure of the cluster, in particular across known surface brightness discontinuities, we performed spectroscopic analysis and obtained the temperature from different selection regions. For spectral analysis, the spectral fitting package SPEX v3.05 (Kaastra et al. 1996; Kaastra et al. 2018a) was used. The reference proto-solar element abundance table is from Lodders et al. (2009). OGIP format spectra and response matrices were converted to SPEX format by the `trafo` task. All spectra were optimally binned (Kaastra & Bleeker 2016) and fitted with C-statistics (Cash 1979). The Galactic hydrogen column density was calculated using the method of Willingale et al. (2013)[4], which takes both atomic

[4] `https://www.swift.ac.uk/analysis/nhtot/`

and molecular hydrogen into account. The weighted effective column density is $n_{\rm H} = 5.92 \times 10^{20}$ cm^{-2}. We used the ROSAT All-Sky Survey (RASS) spectra generated by the X-Ray Background Tool[5] (Sabol & Snowden 2019) to help us to constrain two foreground thermal components: the local hot bubble (LHB) and Galactic halo (GH). The RASS spectrum was selected from a $1^\circ - 2^\circ$ annulus centred at our galaxy cluster. The two foreground components were modelled using single-temperature collisional ionisation equilibrium (CIE) models in SPEX. The GH is absorbed by the Galactic hydrogen while the LHB is unabsorbed. We fixed the abundance to the proto-solar abundance for those two components. The best-fit foreground parameters are shown in Table 2.3. These temperatures are consistent with previous studies (e.g. Yoshino et al. 2009).

2.4.1 XMM-Newton

In the *XMM-Newton* spectral analysis, the effective extraction region areas of spectra from different detectors were calculated using the SAS task `backscale`. To ensure that the extracted spectra from different detectors cover the same sky area, we excluded the union set of the bad pixels of all three detectors from each spectrum. This method leads to lower photon statistics but can reduce the spectral discrepancies due to different selection regions when we perform the parallel fitting. With the calculated `backscale` parameter, we determined the sky area of each spectrum with respect to 1 arcmin^2 and set the region normalisation to that value. The spectral components and models are listed in Table 2.2. We fitted all spectra from different detectors simultaneously. We plot the MOS1 spectrum within r_{500} in Fig. 2.2 as an example to show all spectral components. The components of the MOS2 and pn spectra are similar, so we only additionally plot the fit residuals of these two detectors in Fig. 2.2.

The ICM is modelled with a single temperature CIE. The abundances of metal elements are coupled with the Fe abundance. With the FWC data, we find the particle background continuum can be fit by a broken power law with break energy at 2.5 and 2.9 keV for MOS and pn, respectively. Because the instrumental lines in particle backgrounds are spatially variable, we fitted instrumental lines as delta functions with free normalisations. The energies of instrumental lines are taken from Mernier et al. (2015). If the selection region includes MOS1 CCD4 or MOS2 CCD5 pixels, chan-

[5] `https://heasarc.gsfc.nasa.gov/cgi-bin/Tools/xraybg/xraybg.pl`

Table 2.2: Spectral fitting components and models.

Component	Model[a]	RMF	ARF	Coupling
	XMM-Newton EPIC			
ICM	$cie * reds * hot$[b]	Yes	Yes	-
LHB	cie	Yes	Yes	RASS
GH	$cie * hot$	Yes	Yes	RASS
CXB	$pow * hot$	Yes	Yes	-
FWC continuum	pow	Yes	No	-
FWC lines	$delt$s	Yes	No	-
SP	pow	Dummy[c]	No	-
	Suzaku XIS			
ICM	$cie * reds * hot$	Yes	Yes	-
LHB	cie	Yes	Yes	RASS
GH	$cie * hot$	Yes	Yes	RASS
CXB	$pow * hot$	Yes	Yes	-
	Suzaku XIS offset observation			
LHB	cie	Yes	Yes	RASS
GH	$cie * hot$	Yes	Yes	-
CXB	$pow * hot$	Yes	Yes	-
SWCX	$delt$	Yes	Yes	-
	RASS			
LHB	cie	Yes	Yes	-
GH	$cie * hot$	Yes	Yes	-
CXB	$pow * hot$	Yes	Yes	-

[a] For details of different models, please see the SPEX Manual (`https://spex-xray.github.io/spex-help/index.html`).
[b] We set the temperature of the *hot* model to 5×10^{-4} keV to mimic the absorption of a neutral plasma.
[c] The dummy RMF has a uniform photon redistribution function; see Appendix 2.B for details.

Table 2.3: X-ray foreground components constrained by the RASS spectrum. The normalisations are scaled to a 1 arcmin^2 area.

	Flux (0.1 – 2.4 keV) 10^{-2} ph s^{-1} m^{-2}	kT keV
LHB	3.61 ± 0.07	0.11 ± 0.01
GH	1.49 ± 0.28	0.20 ± 0.02

nels below 1.0 keV are ignored because of the low-energy noise plateau [6]. The two foreground components are coupled with the components of the RASS spectrum. To determine the point source detection limit and calculate the cosmic CXB flux, we first used the CIAO package tool `wavdetect` to detect point sources in a 1 – 8 keV combined *XMM-Newton* EPIC flux image. We set `wavdetect` parameters `scale="1.0 2.0 4.0"`, `ellsigma=4`, and `sigthresh=1e-5`, which is roughly the reciprocal of the image size in our case. The values of other parameters were left as the default. In the detected source list, we selected the four lowest detection significance sources to extract and combined their MOS and pn spectra. The source extraction regions are directly obtained from the output of the *wavdetect* task. Local backgrounds were extracted and subtracted from the total source spectra with elliptical annuli, whose inner radii are the radii of the source regions, and the width is $15''$. We fitted the point source spectra using $abs * pow$ models with free power law normalisation and photon index. The best-fit flux in 2 – 8 keV range is $(6.0 \pm 0.5) \times 10^{-15}$ erg s^{-1} cm^{-2}. Two out of four sources are in our *Chandra* point source catalogue (see Appendix 2.C). Their *Chandra* fluxes are $(6.8 \pm 1.1) \times 10^{-15}$ and $(9.2 \pm 1.2) \times 10^{-15}$ erg s^{-1} cm^{-2}, respectively. Therefore, we used 6.0×10^{-15} erg s^{-1} cm^{-2} from 2 – 8 keV as a detection limit to calculate the CXB surface brightness. The corresponding CXB surface brightness is 3.5×10^{-14} erg s^{-1} cm^{-2} arcmin^{-2} with a fixed photon index $\Gamma = 1.41$; see Appendix 2.C for details. The CXB deviation is calculated by Eq.2.17; we fitted spectra with $\pm 1\sigma_{\rm sys}$ CXB luminosity to obtain the systematic errors contributed by CXB uncertainty. We also included the GH systematic error for *XMM-Newton* spectral analysis with the uncertainty measured from the *Suzaku* offset observation (see Sect. 2.4.2). We calibrated the soft proton background in terms of spec-

[6] `https://xmm-tools.cosmos.esa.int/external/xmm_user_support/documentation/uhb/epicdetbkgd.html`

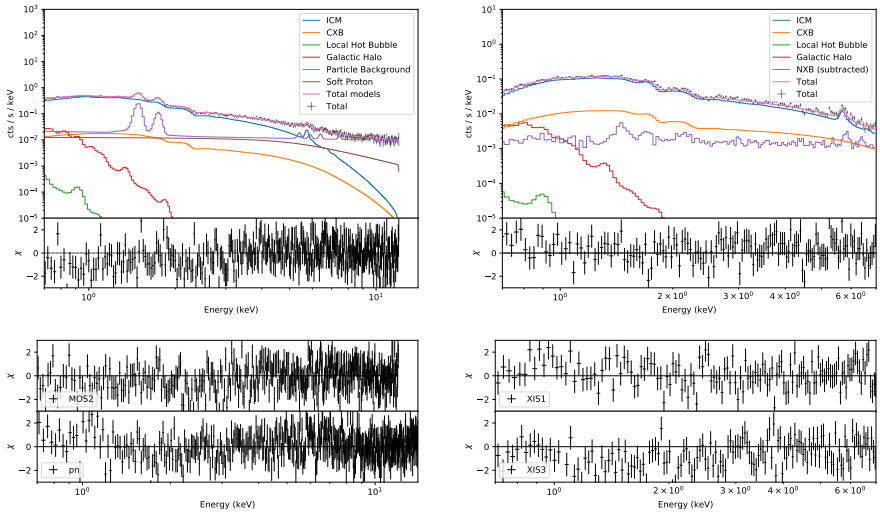

Figure 2.2: r_{500} *XMM-Newton*-EPIC MOS1 (top left) and *Suzaku* XIS0 (top right) spectra as well as individual spectral components. We also plot residuals from the other two EPIC detectors (bottom left) and XIS detectors (bottom right). The fit statistics are $\mathrm{C-stat/d.o.f} = 1992/1554$ for *XMM-Newton* EPIC spectra and $\mathrm{C-stat/d.o.f} = 563/423$ for *Suzaku* XIS spectra.

tral models and vignetting functions with an observation of the Lockman Hole (see Appendix 2.B). The best-fit parameters and the systematic uncertainties of each soft proton component are listed in Table 2.10. When studying the systematics from the soft proton components, we fit spectra with $\pm 1\sigma_{\mathrm{sys}}$ of the MOS1, MOS2, and pn soft proton luminosity individually. The envelope of the highest and the lowest fitted temperatures are taken as the systematics from the soft proton model.

2.4.2 Suzaku

In the *Suzaku* spectral analysis, the energy range 0.7 – 7.0 keV is used for spectral fitting. Auxiliary response files (ARFs) are generated by the task `xissimarfgen` (Ishisaki et al. 2007) with the parameter `source_mode=UNIFORM`. X-ray spectral components are the same as those of the EPIC spectra. We exclude sources with 2 – 8 keV flux $S_{2-8\mathrm{keV}} > 2 \times 10^{-14}$ erg s^{-1} cm^{-2} in our catalogue (see Appendix 2.C) using $1'$ radius circles. The unresolved CXB flux, as well as its uncertainty for each selected region, were calculated

Table 2.4: Best-fit parameters of *Suzaku* offset spectra. The distance of model components is set to $z = 0.162$ to calculate the emissivity. Normalisations are scaled to a 1 arcmin^2 area.

Component	Parameter	Unit	Value	Status
LHB	$norm$	10^{64} m^{-3}	4.7×10^5	Fixed
	kT	keV	0.11	Fixed
GH	$norm$	10^{64} m^{-3}	$(5.6 \pm 0.7) \times 10^5$	Free
	kT	keV	0.20	Fixed
CXB	lum	10^{30} W	$(2.15 \pm 0.07) \times 10^4$	Free
	Γ	-	1.41	Fixed

using Eq. 2.17. All spectra from different detectors were fitted simultaneously as well. Because the *Suzaku* ARFs are normalised to 400π arcmin^2, we set region normalisations in SPEX to 400π. In that case, the fitted luminosity value corresponds to 1 arcmin^2. An example of the XIS0, the r_{500} spectrum is shown in Fig. 2.2 to illustrate all spectral components. As in the EPIC spectra, we additionally plot the residuals of XIS1 and XIS3.

Offset observation

We used the offset observation to study the systematic error from the foreground X-ray components. We extracted spectra from the full FOV but excluded the XIS0 bad region and point sources by visual inspection. We fitted the spectrum from 0.4 to 7.0 keV with LHB, GH, and CXB components. Additionally, we added a delta line component at 0.525 keV to fit an extremely strong O I Kα line, which is generated by the fluorescence of solar X-rays with neutral oxygen in the Earth's atmosphere (Sekiya et al. 2014). Because the LHB flux is prominent at energies much lower than 0.4 keV, we still coupled the normalisation and temperature with the RASS LHB component. From 0.4 to 1 keV, the spectrum is dominated by the GH. We freed the normalisation of the GH but still coupled the temperature with the RASS GH component. The CXB power law index was set as $\Gamma = 1.41$, and the normalisation was thawed. Best-fit parameters are listed in Table 2.4. The best-fit GH normalisation is 40% lower than the best-fit value from RASS. We include the 40% GH normalisation to study the systematic error.

Selection regions

Because of the large radius of the point spread function (PSF) of *Suzaku*, structures on small scales are not resolved. We use sector regions centred at the centre of the cluster and extending towards the southeast (SE), south (S), and southwest (SW) directions (see Fig. 2.1) to extract spectra and measure the temperature profiles.

2.4.3 XMM-Newton-Suzaku cross-calibration

Because *Suzaku* XIS has a lower instrumental background and does not suffer from soft proton contamination due to its low orbit, its temperature measurements in faint cluster outskirts can be considered more reliable than those from *XMM-Newton* EPIC. Therefore, we used the *Suzaku* temperature profiles to cross-check the validity of the *XMM-Newton* temperature profile and verify our soft proton modelling approach. We used the *Suzaku* SE selection region for the cross-check because the S and SW regions cover the missing MOS1 CCD. We extracted EPIC spectra from the exact same regions as the XIS spectra except for the point-source exclusion regions. All spectra were fitted using the method described in Sects. 2.4.1 and 2.4.2. We plot *Suzaku* and *XMM-Newton* temperature profiles as well as profiles from only MOS and pn in Fig. 2.3. Except for the second subregion from the cluster centre, the MOS temperatures are globally higher than *Suzaku* XIS temperatures, which are themselves higher than pn temperatures. The total EPIC temperatures are in agreement with XIS temperatures within the systematic errors.

2.5 Results

We performed both imaging and spectral analysis for surface brightness discontinuities. We measured the global temperature of the cluster. Meanwhile, we obtained temperature profiles to the cluster outskirts using the *Suzaku* data.

2.5.1 Properties of surface brightness discontinuities

We calculate surface brightness profiles from each selection region shown in Fig. 2.1. We use the double power law model introduced in Sect. 2.3 to fit surface brightness profiles. Because *Chandra* has a narrow PSF, we

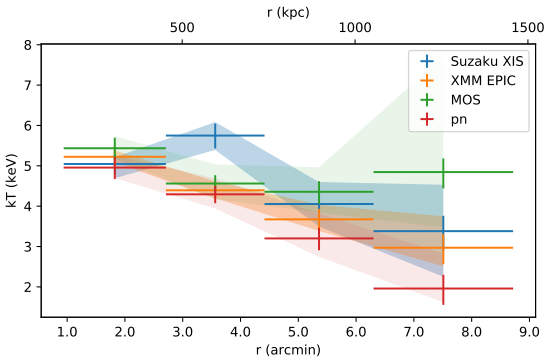

Figure 2.3: Temperature profiles of both *Suzaku* and *XMM-Newton* in the *Suzaku* SE selection region. Filled bands of each profile represent the major systematic errors, i.e. SP for *XMM-Newton* and CXB+GH for *Suzaku*.

Table 2.5: Best-fit parameters and statistics of surface brightness profiles in Fig. 2.4.

	Chandra			*XMM-Newton*	
	$r_{\rm edge}$ ($'$)	C	C-stat / d.o.f.	C	C-stat / d.o.f. [a]
SE	4.00 ± 0.10	1.33 ± 0.13	$54.4/54$	1.09 ± 0.08	$70.3/43$
S	4.76 ± 0.05	1.74 ± 0.15	$55.1/44$	1.45 ± 0.10	$86.2/34$
CF	1.30 ± 0.01	2.00 ± 0.06	$75.2/74$	1.74 ± 0.05	$61.3/74$

[a] Fixed $r_{\rm edge}$ based on the *Chandra* model.

first fit *Chandra* profiles to obtain precise $r_{\rm edge}$s. For *XMM-Newton* profiles, we convolve a $\sigma = 0.1'$ Gaussian kernel to the model to mimic the PSF effect. We fix $r_{\rm edge}$ for the *XMM-Newton* profile fitting based on the value determined with *Chandra*. We compare the C-statistic value when fixing C to the *Chandra* result or allowing it to be free in the fit.

Surface brightness profiles and fitted models are plotted in Fig. 2.4, and fitted parameter values as well as fitting statistics are listed in Table 2.5. There is a systematic offset between the density jumps measured with *Chandra* and *XMM-Newton*. We use the best-fit $r_{\rm edge}$ as the location of the shock/cold front to extract spectra. We also split both the high and low-density sides into several bins when extracting spectra. Temperature profiles are plotted in Fig. 2.5.

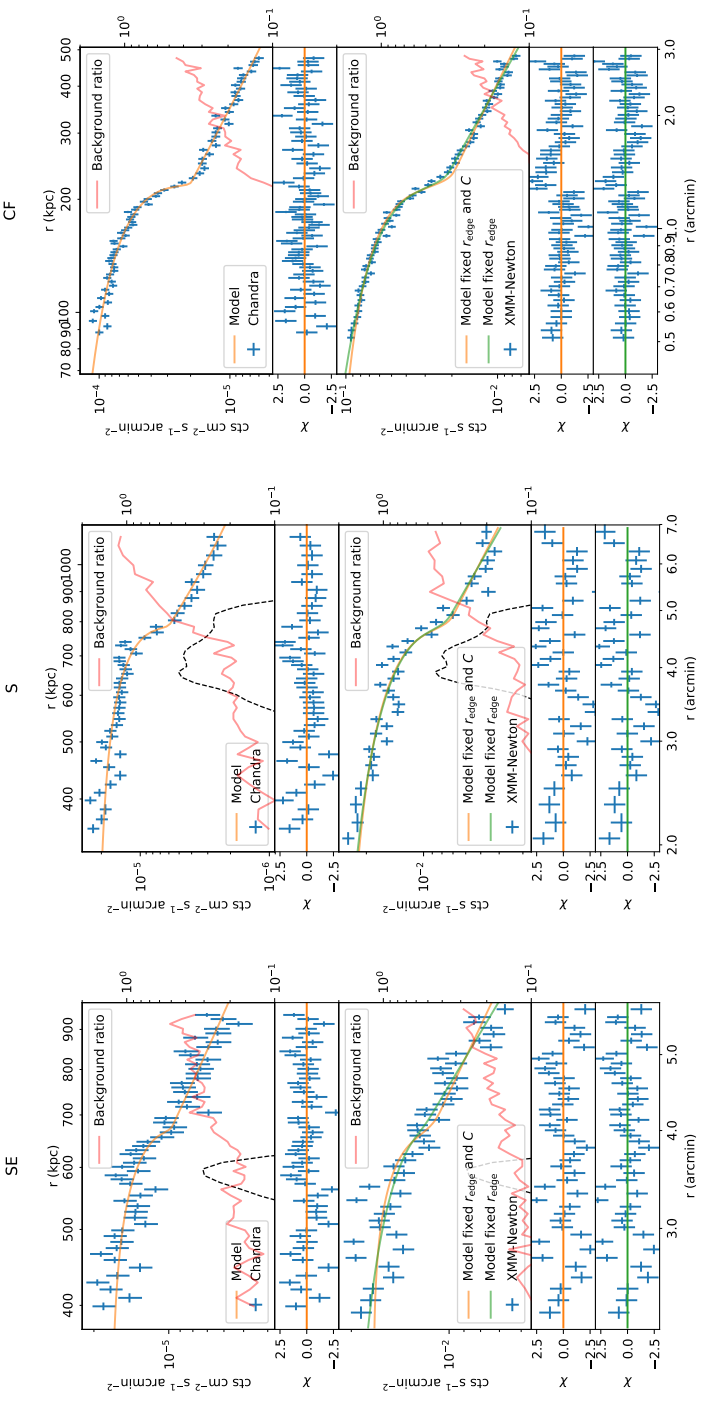

Figure 2.4: Surface brightness profile fitting results of SE, S, and cold front (CF) regions. The upper panel is the *Chandra* surface brightness. The lower panel is the *XMM-Newton* surface brightness profile fitted by fixed and free C parameters. All *XMM-Newton* models are smoothed by a $\sigma = 0.1'$ Gaussian function. Red lines indicate the ratio between the subtracted FWC background counts and the remaining signal, which include the ICM, X-ray background, and soft proton contamination. In regions where this ratio is higher than one, the FWC background dominates. Black dashed lines are the radio surface brightness profiles in an arbitrary unit.

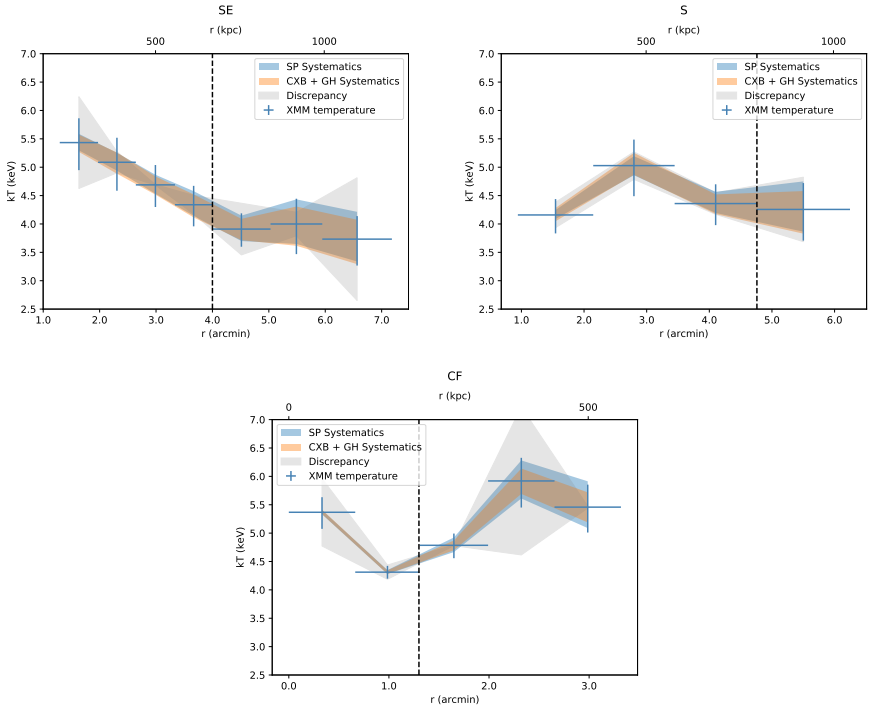

Figure 2.5: *XMM-Newton* temperature profile of each region. Dashed lines indicate edge locations fitted from surface brightness profiles. Grey bands indicate the temperature discrepancy between MOS and pn.

Southeast

At the previously reported shock front, the compression factor fitted with our selection region from the *Chandra* profile is identical to the result of van Weeren et al. (2017), namely $C = 1.3 \pm 0.1$, and is slightly higher than the result of Andrade-Santos et al. (2019), $C = 1.19^{+0.21}_{-0.13}$, but within 1σ uncertainty. However, it is hard to find this feature in the *XMM-Newton* profile. Fitting with fixed $r_{\rm edge}$ and C, we obtain C-stat / d.o.f $= 76.4/44$. If we free the C parameter, the fitted $C_{\rm XMM-Newton} = 1.09 \pm 0.08$, which means the data are consistent with the lack of a density jump, but are consistent with the result of Andrade-Santos et al. (2019). The reason that we do not detect an edge in the *XMM-Newton* profile could be the missing pixels around the edge. The radio relic is located very close to bad pixel columns of MOS2,

and a CCD gap of pn. The temperature profile (the top-left panel in Fig. 2.5) drops linearly and then flattens at larger radii. The temperature at the bright side of the edge is higher than at the other side. Hence, we rule out the possibility that this edge is a cold front.

South

In the southern region, a significant surface brightness jump is seen in both *Chandra* ($C_{\rm Chandra} = 1.74 \pm 0.15$) and *XMM-Newton* ($C_{\rm XMM-Newton} = 1.45 \pm 0.10$) profiles. A simple spherically symmetric double power-law density model cannot fit the *Chandra* profile perfectly; it is a sudden jump with flat or even increasing surface brightness profile on the high-density side. There is an excess above the best-fit model at the edge. The temperature is almost identical across the edge, which is not a typical shock or cold front. We discuss this edge in Sect. 2.6.3.

Cold front

The cold front surface brightness profile can be well modelled by the double power-law density model. The density ratio from *Chandra* observation $C_{\rm Chandra} = 2.00 \pm 0.06$ is higher than that from the *XMM-Newton*, which is $C_{\rm XMM-Newton} = 1.74 \pm 0.05$. Similar to the southern edge, even if we account for the PSF of *XMM-Newton*, the density jump measured by *XMM-Newton* is smaller than that determined using *Chandra*. In addition, the inner power-law component of the density profiles is steeper when measured with XMM-Newton than with Chandra. The energy dependence of the vignetting function and of the effective area (and their uncertainties) can affect this inner slope, which in turn is correlated with the density jump (a steeper inner power-law leads to a smaller compression factor). This may contribute to the observed differences. The temperature profile confirms that it is a cold front. The temperature reaches the minimum before the cold front and then rises until $r = 3'$.

2.5.2 Global temperature

We extract spectra from the region with $r_{500} = 1.3$ Mpc (Andrade-Santos et al. 2019) to obtain the global temperature. Although we miss MOS1 CCD3 and 6, most of the flux is in the centre CCD, which means our result will not be significantly biased by the missing CCDs. The best-fit temper-

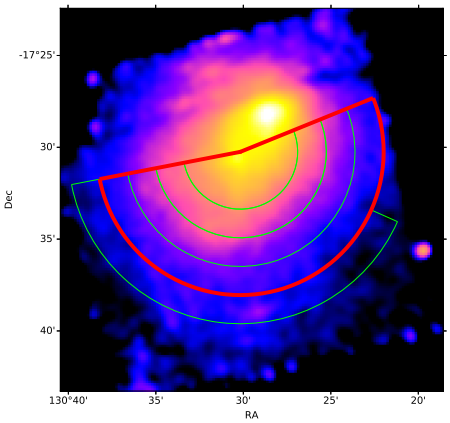

Figure 2.6: *Suzaku* semicircle r_{500} selection region (red) and radial bins (green).

ature is $kT_{500} = 4.84 \pm 0.04 \pm 0.19$ keV, where the second error item represents the systematic uncertainty. The temperatures of individual detectors are listed in Table 2.6. The $kT_{500,\mathrm{MOS}}$ is about 0.1 keV higher than $kT_{500,\mathrm{pn}}$. These two measurements agree within their 1σ uncertainty interval, which is dominated by the systematic error from the soft proton model. Compared with the result of Andrade-Santos et al. (2019) of $kT_{500} = 6.5 \pm 0.1$ keV, the kT_{500} in our work is much lower.

We also used *Suzaku* data to check the global temperature. *Suzaku* does not suffer from soft proton contamination, and its NXB level is lower than that of *XMM-Newton*, making it a valuable tool to check our *XMM-Newton* analysis. The *Suzaku* observation does not cover the whole r_{500} area. To avoid the missing XIS0 strip, we extract spectra from the south semicircle (see the red region in Fig. 2.6). The best-fit results with all detectors as well as with the only front-illuminated (FI, XIS0 + XIS3) and back-illuminated (BI, XIS1) CCDs are listed in Table 2.6. The best-fit temperature is $kT_{500} = 5.17 \pm 0.07 \pm 0.13$ keV, which is slightly higher than the *XMM-Newton* result.

2.5.3 Temperature profiles to the outskirts

Individual *Suzaku* temperature profiles of three sectors are shown in Fig. 2.7. Apart from three individual directions, we split the *Suzaku* r_{500} re-

Table 2.6: kT_{500} from *XMM-Newton* and *Suzaku*.

	kT_{500} (keV)	$\sigma_{\rm sys}$[a](keV)
XMM-Newton	4.84 ± 0.04	0.19
MOS	4.92 ± 0.06	0.37
pn	4.80 ± 0.06	0.40
Suzaku	5.17 ± 0.07	0.13
FI	5.36 ± 0.11	0.13
BI	4.97 ± 0.12	0.13

[a] For *XMM-Newton* spectra, the major systematic error is from the soft proton component. For *Suzaku* spectra, the systematic error is the combined from the CXB and GH components.

gion into four annuli (the green regions in Fig. 2.6), and define another bin outside of r_{500}. We plot all four profiles together with a typical relaxed cluster outskirt temperature profile (Burns et al. 2010), where we take $\langle kT \rangle = 5.2$ keV. The curve obtained by these latter authors agrees with *Suzaku* observations of relaxed clusters remarkably (Akamatsu et al. 2011; Reiprich et al. 2013). For our data, at r_{500}, the southern temperature profile agrees with the profile of Burns et al. (2010). The other three profiles are marginally higher than the typical relaxed cluster temperature profile but within 1σ systematic error. In the work of Burns et al. (2010), $\langle kT \rangle$ is the averaged temperature between 0.2 and 2.0 r_{200}. Because our *Suzaku* observation only covers the r_{500} area, the actual $\langle kT \rangle$ could be slightly lower than the value we use. In that case, the southern temperature profile could also be marginally higher than the profile of Burns et al.. This cluster is undergoing a major merger, and our results show that the temperature in the outskirts has been disturbed.

2.6 Discussion

2.6.1 T_{500} discrepancy

Our measurements of kT_{500} are lower than the result of *Chandra* data. The cross-calibration uncertainties between *XMM-Newton* EPIC and *Chandra* ACIS may be the major cause for this discrepancy. Using the scaling relation of temperatures between EPIC and ACIS $\log kT_{\rm EPIC} = 0.0889 \times$

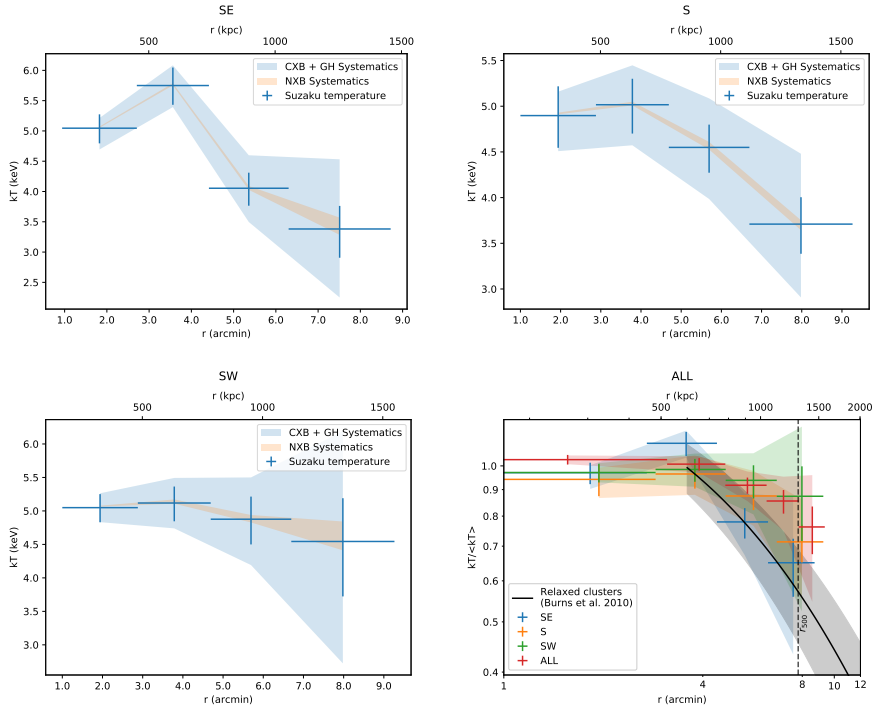

Figure 2.7: *Suzaku* temperature profiles of the SE, S, and SW regions, as well as a comparison with the relaxed temperature profile in the outskirts predicted by numerical simulations.

$\log kT_{\rm ACIS}$ (Schellenberger et al. 2015), a 6.5 keV ACIS temperature corresponds to a 5.3 keV EPIC temperature, which is close to our measurement. By contrast, the temperature discrepancy between *XMM-Newton* EPIC and *Suzaku* XIS is relatively small. This discrepancy of 8% is slightly larger than the value from the *Suzaku* XIS and *XMM-Newton* EPIC-pn cross-calibration study (5%, Kettula et al. 2013). Because the *Suzaku* extraction region does not cover the cold front, the reported *Suzaku* temperature may be higher than the average value within the entire r_{500} region, explaining this difference.

With our temperature results, we use the $M_{500}-kT_X$ relation $h(z)M_{500} = 10^{14.58} \times (kT_X/5.0)^{1.71}\ M_\odot$ (Arnaud et al. 2007) to roughly estimate the mass of the cluster. The kT_X is the temperature from 0.1 to $0.75r_{500}$. We do not exclude the inner $0.1r_{500}$ part because it is not a relaxed system, and

there is no dense cool core in the centre. For $kT_X = 5.0$ keV, the $M_{500} - T_X$ relation suggests a mass of $M_{500} = 5.1 \times 10^{14}\ M_\odot$. This is less than that from the Planck Sunyaev-Zeldovich catalogue of $M_{\rm SZ} = (6.6 \pm 0.3) \times 10^{14}\ M_\odot$ (Planck Collaboration et al. 2016). However, this underestimation is not surprising. Because the source is undergoing a major merger, the kinetic energy of two sub-halos is still being dissipated into the thermal energy of the ICM. Once the system relaxes, the kT_X will be higher than in the current epoch.

2.6.2 Shock properties

The shock Mach number can be calculated by the Rankine-Hugoniot condition (Landau & Lifshitz 1959) either from the density jump or from the temperature jump,

$$\mathcal{M} = \left[\frac{2C}{\gamma + 1 - C(\gamma - 1)}\right]^2 \tag{2.3}$$

$$\frac{T_1}{T_2} = \frac{(\gamma+1)/(\gamma-1) - C^{-1}}{(\gamma+1)/(\gamma-1) - C}, \tag{2.4}$$

where C is the compression factor across the shock, and $\gamma = 5/3$ if we assume the ICM is an ideal gas. Because the systematic errors from the CXB and GH are Gaussian, we directly propagate them into the statistical error when estimating the Mach number uncertainty. However, the soft proton systematic uncertainty is not Gaussian, and so we use the measured temperature and the temperature obtained by varying the soft proton component within their $\pm 1\sigma$ uncertainties determined in Appendix 2.B to estimate the *XMM-Newton* Mach number systematic error.

The *Suzaku* southeast sector covers the re-acceleration site, and we see a jump from the second to the third point in that temperature profile. The *Suzaku* spectral extraction regions are defined unbiasedly. We further inspect the temperature profile based on the radio morphology. The radio-based selection region is shown in Fig. 2.8. We intentionally leave a $1.1'$ gap (Akamatsu et al. 2015) between the second and the third bin to avoid photon leakage from the brighter side. We plot both the *XMM-Newton* and *Suzaku* temperature profiles of this sector in Fig. 2.9. Because *XMM-Newton* has a much smaller PSF than *Suzaku*, we can use the spectrum from the gap.

There is a systematic offset between *Suzaku* and *XMM-Newton*. The *Suzaku* temperature is globally higher than the *XMM-Newton* temperature.

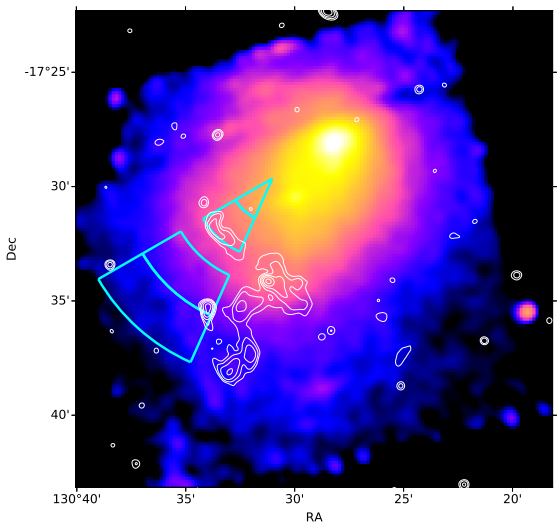

Figure 2.8: *Suzaku* flux map and the cyan spectral extraction regions are based on radio morphology (white contours).

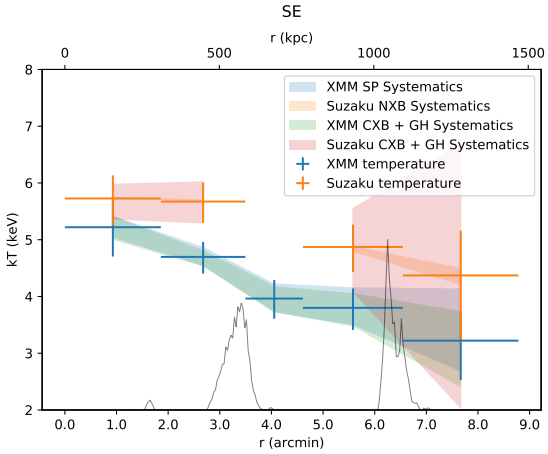

Figure 2.9: *Suzaku* and *XMM-Newton* temperature profiles from the radio-based selection regions in Fig. 2.8. The radio surface brightness profile is plotted as a black line.

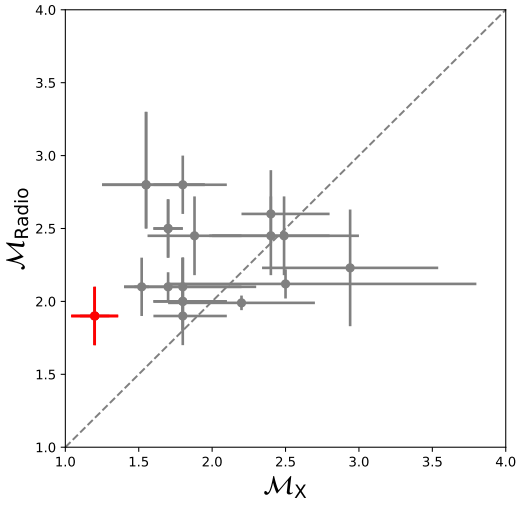

Figure 2.10: Shock Mach numbers derived from radio spectral index ($\mathcal{M}_{\rm Radio}$) against those from the ICM temperature jump ($\mathcal{M}_{\rm X}$). The data points of previous studies (grey) are adapted from Fig. 22 in van Weeren et al. (2019). The red point is the southwestern shock in Abell 3411-3412.

Both profiles drop from the centre of the cluster to the outskirts. The new *XMM-Newton* temperature profile is similar to the previous one in Sect. 2.5.1. The temperature decreases from the centre of the cluster and flattens after the radio relic. We use temperatures across the radio relic to obtain the shock Mach number. As a comparison, we calculate the Mach number by the density jump fitted from the *Chandra* surface brightness profile. Results are listed in Table 2.7. From our spectral analysis, we confirm the Mach number of this shock is close to the value measured from the surface brightness profile fit. Results from all telescopes point to the value $\mathcal{M}_{\rm X} \sim 1.2$. This shock is another case where the radio Mach number is higher than the X-ray Mach number (see Fig. 2.10). Such a low Mach number supports the re-acceleration scenario. We note that our calculation does not account for the presence of a 'relaxed' temperature gradient in the absence of a shock. This could further reduce the Mach number, but the conclusion that the re-acceleration mechanism is needed would remain robust.

Table 2.7: Comparison of the southeast shock Mach number obtained from different instruments and methods. The second error in the *XMM-Newton* measurement is the soft proton systematic error.

Instrument	$\mathcal{M}_T$	$\mathcal{M}_{\rm SB}$
XMM-Newton EPIC	$1.19 \pm 0.15 \pm 0.03$	
Suzaku XIS	1.17 ± 0.23	
Chandra ACIS		1.20 ± 0.07
		$1.13^{+0.14}_{-0.08}{}^{\dagger}$

† From (Andrade-Santos et al. 2019).

2.6.3 The mystery of the southern edge

The density jump at the southern edge is strong, and Andrade-Santos et al. (2019) claim it is a cold front from the sub-cluster Abell 3412. From our spectral fitting, the temperature inside and outside of the southern edge is $kT = 4.36 \pm 0.34$ keV, and $kT = 4.26 \pm 0.46$ keV, respectively. The projected temperature jump is 1.02 ± 0.14. From the surface brightness fitting, the de-projected density jump is $C = 1.7 \pm 0.2$. This value corresponds to a de-projected temperature jump of 1.48 ± 0.25 under the assumption of Rankine-Hugoniot shock conditions, and a temperature jump 0.59 ± 0.07 under the assumption that it is a cold front in pressure equilibrium. Neither the shock scenario nor the cold front scenario matches the measured lack of temperature jump.

To obtain the de-projected temperature jump, we simply assume that the spectrum from the high-density side is a double-temperature spectrum. The temperature of one of the components is the same as that from the low-density side. We assume that the discontinuity structure is spherically symmetric, and calculate the volume ratio between the intrinsic and projected components in the high-density side. We fit spectra from both sides simultaneously. For the high-density side spectrum, we couple one CIE temperature to that of the low-density spectrum. We also couple the normalisation of that component to that of the low-density spectrum with a factor of the volume ratio. We leave the other two temperature and normalisation parameters free. The de-projected temperature ratio is then 1.08 ± 0.17 with a systematic uncertainty 0.10. This value is $\sim 1.3\sigma$ offset from the shock scenario but is $\sim 2.6\sigma$ offset from the cold front scenario. Therefore, the temperature jump we measured is in closer agreement with

the shock scenario. Also, the pressure across the edge is out of equilibrium. The pressure jump implies a supersonic motion of the gas.

The presence of a huge density jump but a marginal temperature jump suggests an excess of surface brightness on the bright side of the edge. Also, the *Chandra* surface brightness profile shows a tip beyond the best-fit double power-law density model. Because the brightest cluster galaxy (BCG) of Abell 3412 (see Fig. 2.1) is located only $1'$ away from the southern edge, the surface brightness excess may be due to the remnant core of the subcluster Abell 3412. We are therefore looking at a more complex superposition of a core and a shock. The second possibility is that the excess emission may be associated with one galaxy in the cluster, which contains highly ionised gas. The gas is being stripped from the galaxy while it moves in the cluster (e.g. ESO 137-001 Sun et al. 2006). A third possibility is that the excess emission could be inverse Compton (IC) radiation from the radio jet tail on top of the X-ray edge. We estimate the upper limit of IC emission based on the equation from Brunetti & Jones (2014):

$$F_{\rm IC}(\nu_{\rm X}) = 1.38 \times 10^{-34} \left(\frac{F_{\rm Syn}(\nu_{\rm R})}{\rm Jy}\right) \left(\frac{\nu_{\rm X}/{\rm keV}}{\nu_{\rm R}/{\rm GHz}}\right)^{-\alpha} \times \frac{(1+z)^{\alpha+3}}{\left\langle B_{\mu{\rm G}}^{1+\alpha}\right\rangle} \ell(\alpha), \tag{2.5}$$

where $\left\langle B_{\mu{\rm G}}^{1+\alpha}\right\rangle$ is the emission-weighted magnetic field strength and $\ell(\alpha)$ is a dimensionless function. In Abell 3411, the radio spectral index at the southern edge is $\alpha \sim 1$ (van Weeren et al. 2017), at which $\ell = 3.16 \times 10^3$. In the third southern spectral extraction region, the averaged radio flux at 325 MHz is 1.2×10^{-3} Jy arcmin^{-2}. Usually, in the ICM, the magnetic field value B is approximately equal to between one and a few μG. If we use $\langle B \rangle = 1$ μG to estimate the upper limit of the X-ray IC flux, the corresponding flux density is 3.24×10^{-24} erg s^{-1} Hz^{-1} cm^{-2} arcmin^{-2}. The converted photon density is 7.8×10^{-9} ph s^{-1} keV^{-1} cm^{-2} arcmin^{-2} at 1 keV. In the 1.2 – 4.0 keV band, the contribution of the IC emission is 2.8×10^{-8} ph s^{-1} cm^{-2} arcmin^{-2}, which is about two orders of magnitude lower than the total source flux. This possibility is therefore ruled out.

2.6.4 The location of the bow shock

In front of the bullet, Andrade-Santos et al. (2019) claim the detection of a bow shock with $\mathcal{M} = 1.15^{+0.14}_{-0.09}$ at $r = 3.48^{+0.61}_{-0.71}$ arcmin. The signif-

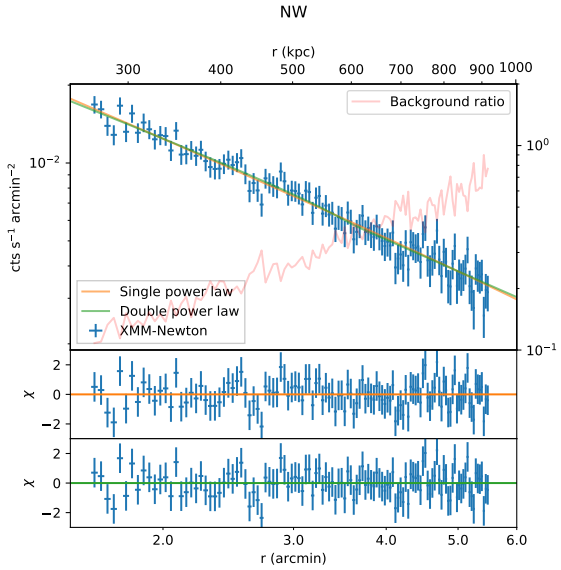

Figure 2.11: *XMM-Newton* surface brightness profile of the northwest region. No density jump is found.

icance of the density jump is low and the uncertainty of the location is large. To confirm this jump, we extract the *XMM-Newton* surface brightness profile in front of the bullet using the same region definition as that used by Andrade-Santos et al. (2019) (see Fig. 2.11). We fit the profile using both single power-law and double power-law models. The double power-law model returns C-stat/d.o.f. $= 98.4/115$ with density jump $C = 1.056 \pm 0.061$. As a comparison, the single power-law model returns C-stat/d.o.f. $= 99.8/118$. A single power-law model can fit this profile well.

So far, radio observation cannot pinpoint the bow shock because this cluster has neither a radio relic nor a radio halo edge in the northern outskirts. One other method to predict the bow shock location is to use the relation between the bow shock stand-off distance and the Mach number (Sarazin 2002; Schreier 1982). However, Dasadia et al. (2016) found that most of the bow shocks in galaxy clusters have longer stand-off distances than the expected value. In extreme cases, such as that of Abell 2146 (Russell et al. 2010), the difference can reach a factor of ten (Dasadia et al. 2016). Recently, from simulations, Zhang et al. (2019a) found that the unexpectedly large stand-off distance can be due to de-acceleration of the cold front

speed after the core passage, while the shock front can move faster.

The offset between the projected BCG (see Fig. 2.1) and the X-ray peak positions implies the merging phase. For the sub-cluster Abell 3411, the BCG lags behind the X-ray peak by $\sim 17''$. Without a weak-lensing observation, we consider the position of the BCG as the bottom of the gravitational potential well of the dark matter halo. When two sub-clusters undergo the first core passage, the position of the dark matter halo will usually be in front of the gas density peaks (e.g. the Bullet cluster, Clowe et al. 2006) because dark matter is collision-less, but the ICM is collisional. When the dark matter halo reaches the apocentre, the ambient gas pressure drops quickly and so the gas can catch up and overtake the mass peak (e.g. Abell 168, Hallman & Markevitch 2004). Hence, the location of the BCG of Abell 3411 indicates the dark matter halo has almost reached its apocentre. The dynamic analysis also suggests the two sub-clusters are near their apocentres (van Weeren et al. 2017). Thus, the stand-off distance could be much larger than the expected value. The stand-off distance calculated from the bow shock location reported by Andrade-Santos et al. (2019) almost matches the Mach number $\mathcal{M} \sim 1.2$. We speculate that the real bow shock location could be far ahead of the reported location. Unfortunately, in the northwestern outskirts, the *XMM-Newton* counts are dominated by the background, and the *Suzaku* observation does not cover that region. We are unable to probe the bow shock by thermodynamic analysis.

2.7 Conclusion

We analyse the *XMM-Newton* and *Suzaku* data to study the thermodynamic properties of the merging system Abell 3411-3412. We calibrate the *XMM-Newton* soft proton background properties based on one Lockman hole observation and apply the model to fit the Abell 3411 spectra (Appendix 2.B). Our work is an update of the current understanding of this merging system. We summarise our results as follows:

1. We measure $T_{500} = 4.84 \pm 0.04 \pm 0.19$ with *XMM-Newton* and $T_{500} = 5.17 \pm 0.07 \pm 0.13$ in the southern semicircle with *Suzaku*. The corresponding mass from the $M_{500} - T_{\rm X}$ relation is $M_{500} = 5.1 \times 10^{14}$ $M_{\odot}$.

2. The *Chandra* northern bullet-like sub-cluster and southern edges are detected by *XMM-Newton* as well, while the southeastern edge shows

no significant density jump in the *XMM-Newton* surface brightness profile.

3. The southern edge was claimed as a cold front previously (Andrade-Santos et al. 2019). With our *XMM-Newton* analysis, the temperature jump prefers a shock front scenario. There is a clear pressure jump indicating supersonic motions, although the geometry seems to be more complicated, with a possible superposition of a shock and additional stripped material from the Abell 3412 sub-cluster.

4. Both *Suzaku* and *XMM-Newton* results confirm the southeastern edge is a $\mathcal{M} \sim 1.2$ shock front, which agrees with the previous result from *Chandra* surface brightness fit (van Weeren et al. 2017; Andrade-Santos et al. 2019). Such a low Mach number supports the particle re-acceleration scenario at the shock front.

Acknowledgments

We thank the anonymous referee for constructive suggestions that improved this paper. X.Z. is supported by the the China Scholarship Council (CSC). R.J.vW. acknowledges support from the ERC Starting Grant ClusterWeb 804208. SRON is supported financially by NWO, The Netherlands Organization for Scientific Research. This research made use of Astropy,[7] a community-developed core Python package for Astronomy (Astropy Collaboration et al. 2013, 2018). This research is based on observations obtained with *XMM-Newton*, an ESA science mission with instruments and contributions directly funded by ESA Member States and NASA. This research has made use of data obtained from the *Suzaku* satellite, a collaborative mission between the space agencies of Japan (JAXA) and the USA (NASA). This research has made use of data obtained from the *Chandra* Data Archive and the *Chandra* Source Catalog, and software provided by the *Chandra* X-ray Center (CXC) in the application package CIAO.

[7] `http://www.astropy.org`

2.A Light curves of EPIC CCDs

In Table 2.1, the MOS2 GTI is about 8 ks larger than MOS1. We plot the light curve and filtered GTIs of each EPIC detector in Fig. 2.12. Although the light curves of two MOS detectors show a similar trend, some flares are only significant in MOS1. This explains why we obtain less GTI for MOS1.

Out-of-FOV detector pixels are usually used for particle background level estimation. However, the out-of-FOV corners of the EPIC-pn CCD suffer from soft proton flares as well. We select 100s binned pn out-of-FOV light curves with selection criteria `FLAG==65536 && PATTERN==0 && (PI IN [10000:12000])`. To make a comparison, we extract light curves of the two MOS CCDs with the same out-of-FOV region expressions as in Sect. 2.2, which are from Kuntz & Snowden (2008). Light curves are plotted in Fig. 2.13. We use a two-sample Kolmogorov-Smirnov (KS) test to check whether the cumulative density function (CDF) of the count rate matches a Poisson distribution. For the pn CCD, the p-value is less than 0.05. Therefore, the null hypothesis that the count rate follows a Poisson distribution is rejected. The KS test suggests that the out-of-FOV region of the pn detector is significantly contaminated by soft proton flares, while the out-of-FOV of the MOS area is clean enough to be used as a reference for the particle background level estimation.

2.B Soft proton modelling

Our observation suffered from significant soft proton contamination. Although we adopt strict flare filtering criteria, the contamination in the quiescent state is not negligible. Inappropriate estimations of the soft proton flux, as well as its spectral shape, would introduce considerable systematic error to fit the results. The integrated flare state soft proton spectra from MOS are studied by Kuntz & Snowden (2008). They are smooth and featureless, with the shape of an exponential cut-off power law. The spectrum is harder when flares are stronger.

The soft proton spectra of pn during flares have not been studied yet. To investigate the soft proton background properties, including spectral parameters, vignetting functions, and so on, we analyse one observation of the Lockman Hole (ObsID: 0147511201), which is also heavily contaminated by soft proton flares. That observation was also performed with the medium filter. Flare state time intervals are defined by $\mu + 2\sigma$ filtering cri-

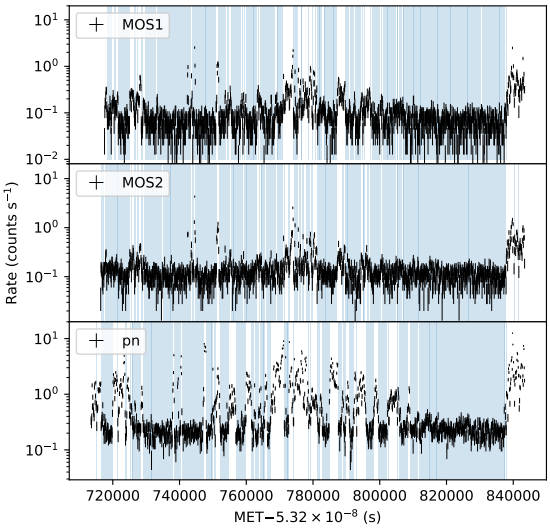

Figure 2.12: Inside FOV light curves for the three EPIC detectors in the 10 –12 keV band with 100s bins. The filtered GTIs are shown as blue shadows.

teria on 100 s binned light curves in the 10 – 12 keV energy intervals. The flare state proportion of pn is $\sim 87\%$. The pure flare state spectra are simply calculated by subtracting quiescent state spectra from flare state spectra.

2.B.1 Spectral analysis

Flare state soft proton spectra in the 0.5 – 14.0 keV band within a $12'$ radius are plotted in Fig. 2.14. The spectra of the centre and outer MOS CCDs are plotted individually. The shape of the pn spectrum is almost coincident with that of MOS; they are all smooth and featureless and can be described as a cut-off power law. The spectra from central MOS CCDs are coincident with each other. However, the spectra from outer CCDs are slightly different.

Redistribution matrix files (RMFs) generated by `rmfgen` are calibrated on photons and include the photon redistribution jump at the Si K edge. However, we do not see any feature there in the soft proton spectra. As a result, we use `genrsp` in FTOOL to generate a dummy RMF for fitting. A SPEX built-in generalised power-law model is used to model the soft

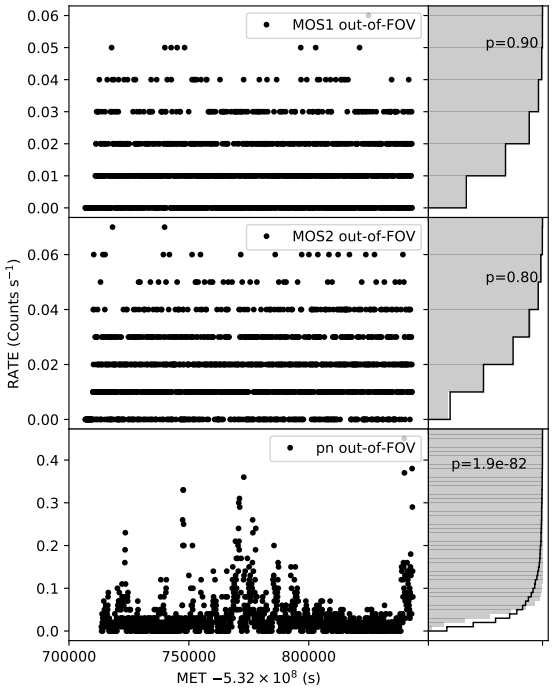

Figure 2.13: Out-of-FOV 10 –12 keV light curves of three EPIC detectors. Right panels are CDFs of count rates. For each light curve, the CDF of the Poisson distribution with μ from the data is plotted as a grey area. The p-values to reject the null hypothesis that the count rate distribution is Poisson are labelled.

proton spectra. The generalised power law can be expressed as

$$F(E) = AE^{-\Gamma}e^{\eta(E)}, \tag{2.6}$$

where A is the flux density at 1 keV, Γ is the photon index, and $\eta(E)$ is given by

$$\eta(E) = \frac{r\xi + \sqrt{r^2\xi^2 + b^2(1-r^2)}}{1-r^2}, \tag{2.7}$$

with $\xi = \ln(E/E_0)$ and $r = (\sqrt{1+(\Delta\Gamma)^2} - 1)/|\Delta\Gamma|$, where E_0 is the break energy, $\Delta\Gamma$ is photon index difference after the break energy, and b is the break strength. Instead of using flux density A, we have adjusted the model implementation to use 2 – 10 keV integrated luminosity L as a normalisation factor.

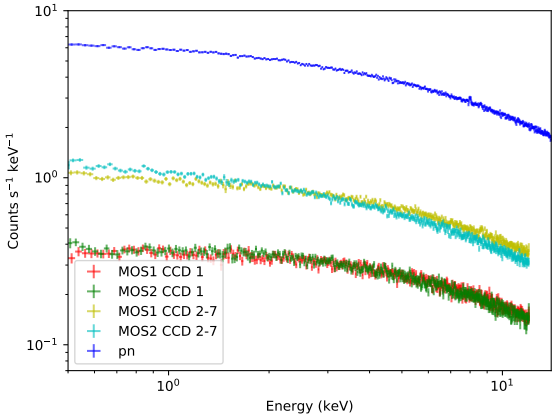

Figure 2.14: Flare state soft proton spectra in $12'$ radius.

We fit the integrated pn, MOS centre CCD, and MOS outer CCDs spectra with the model described above. To solve the degeneracy of parameters, we fix all Γ to 0, and therefore the photon index after the break energy $\Gamma_2 = \Delta\Gamma$. We manually choose sets of E_0 and b values inside the 1σ contours from the parameter diagrams (see Fig. 2.15). All fixed and fitted parameters, as well as the fit statistics, are listed in Table 2.8.

2.B.2 Vignetting function

The soft proton vignetting function is different from that of X-rays. To determine the spatial distribution of soft proton counts, we study the vignetting behaviour of different CCDs from the Lockman hole observation. We calculate surface brightness profiles with our surface brightness profile analysis tool. We take total count maps as the source images and quiescent state count maps as backgrounds. A uniform dummy exposure map is applied. The surface brightness profile of the residual soft protons reflects the vignetting behaviour.

The count weighted vignetting functions in the 2 – 10 keV band are shown in Fig. 2.16. Because the MOS outer chips are closer to the mirror, there is a gap the vignetting functions of the central and outer CCDs. The vignetting behaviours of MOS1 and MOS2 centre CCDs are similar, but different in the outer CCDs. We fit vignetting functions with β profiles

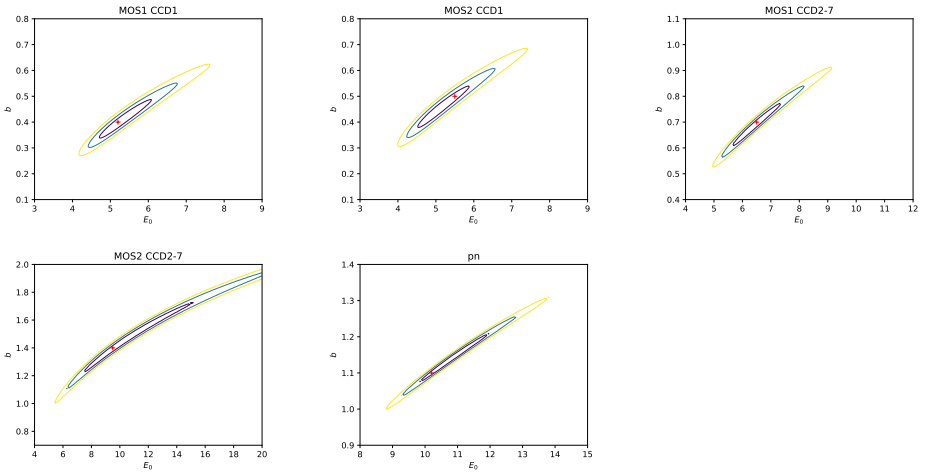

Figure 2.15: Best-fit statistics for the Lockman hole soft proton flare state spectra in E_0 vs. b space. The chosen parameters are plotted as red crosses. Contours from inner to outer are 1σ, 2σ, and 3σ confidence levels.

(Cavaliere & Fusco-Femiano 1976)

$$S(r) = S_0 \left[1 + \left(\frac{r}{r_0}\right)^2\right]^{0.5-3\beta}, \tag{2.8}$$

where r_0 is fixed to $40'$. Best fit parameters are listed in Table 2.9.

2.B.3 Self-calibration

We extract MOS and pn spectra from the Abell 3411 observation, separating the MOS centre and outer CCD region. We exclude the union of the MOS and pn bad pixel regions using additional region selection expressions. The selected regions are annuli centred at the pn focal point from $1'$ to $12'$ with width $1'$. From the central MOS CCD region, we extract spectra up to $r = 6'$. From the outer MOS CCD region, we extract spectra from $r = 8'$. There are 3×5 centre region spectra and 3×4 outer region spectra in total. The energy range 0.5 – 14.0 keV is used for spectral fitting. Spectral components are the same as described in Table 2.2. We first fit FWC spectra with an exponential cut off power law and delta lines. We freeze the FWC continuum with the fitted cut-off power-law parameters and fit

Table 2.8: Best-fit parameters of flare state soft proton spectra in the Lockman Hole observation.

	Γ_2	E_0 (keV)	b	C-stat/d.o.f.
MOS1 CCD 1	0.941 ± 0.008	5.2	0.4	622/890
MOS2 CCD 1	1.060 ± 0.008	5.5	0.5	658/890
MOS1 CCD 2-7	1.206 ± 0.006	6.5	0.7	807/457
MOS2 CCD 2-7	1.629 ± 0.008	9.5	1.4	728/457
pn	1.632 ± 0.004	10.2	1.1	840/539

Table 2.9: Best fit parameters of 2 – 10 keV soft proton vignetting functions. Parameter r_0 is fixed to $40'$.

	S_0 (arbitrary unit)	β
MOS1 CCD1	1.824 ± 0.008	2.35 ± 0.10
MOS1 CCD 2-7	1.906 ± 0.009	1.51 ± 0.03
MOS2 CCD1	1.778 ± 0.008	2.17 ± 0.10
MOS2 CCD 2-7	1.743 ± 0.008	1.45 ± 0.03
pn	8.316 ± 0.011	1.325 ± 0.010

the soft proton and ICM components. We add two delta lines at 0.56 and 0.65 keV to fit the SWCX radiation. The other free parameters are Γ_2 and L of soft proton components, $norm$, T and Z of the ICM. The best-fit values of a subset of the most relevant parameters are plotted in Fig. 2.17.

We use constant models to fit five Γ_2 profiles, and use the vignetting models from Appendix 2.B.2 to fit five luminosity profiles individually. We fix each β parameter but thaw the normalisation. Best-fit soft proton L_0s and Γ_2s are listed in the second and third columns of Table 2.10, respectively. The best-fit model profiles are plotted with solid lines in Fig. 2.17. If we assume the detector responses to SP are identical over time and in both flare and quiescent states, we can estimate the luminosity profiles in a second way. For this, we need to calculate the ratio of normalisations among different detectors. From Appendix 2.B.2 we have surface brightness radial profiles at the flare state

$$S_{\rm Det}^{\rm Flare}(r) = \int_2^{10} {\rm Vig}_{\rm Det}(r) F_{\rm Det}^{\rm Flare}(E, r) {\rm d}E, \tag{2.9}$$

where $F_{\rm Det}^{\rm Flare}$ are the flare state spectrum models of different CCDs at radius

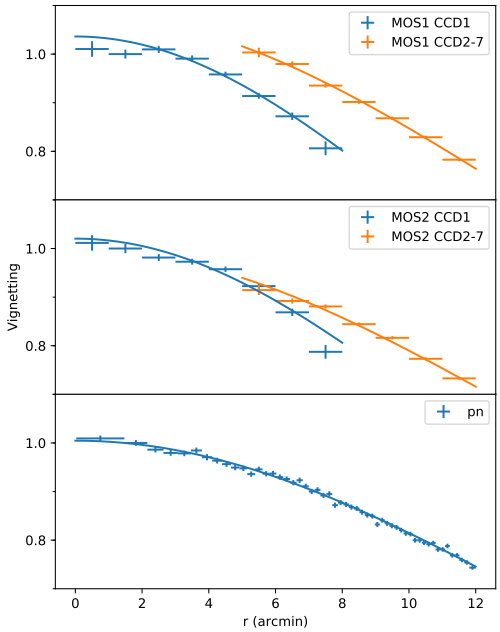

Figure 2.16: Vignetting functions of flare state soft protons detected by the EPIC CCDs in the 2 – 10 keV band determined from the Lockman hole observation. Each set of measurements is normalised to the second data point. Solid lines are best-fit β models.

r, and Vig is the vignetting function. Det can be MOS1 center, MOS1 outer, MOS2 center, MOS2 outer and pn. We take pn as a reference. The count rate ratio between other detectors and pn is

$$\xi^{\rm Flare}_{\rm CR,Det/pn}(r) = \frac{{\rm Vig}_{\rm Det}(r)}{{\rm Vig}_{\rm pn}(r)} \frac{\int_2^{10} F^{\rm Flare}_{\rm Det}(E,r){\rm d}E}{\int_2^{10} F^{\rm Flare}_{\rm pn}(E,r){\rm d}E}. \tag{2.10}$$

The energy flux ratio between other detectors and pn at the quiescent state

can be easily calculated:

$$\begin{aligned}\xi^{\rm Quiescent}_{\rm E,Det/pn}(r) =& \frac{{\rm Vig}_{\rm Det}(r)}{{\rm Vig}_{\rm pn}(r)} \frac{\int_2^{10} EF^{\rm Quiescent}_{\rm Det}(E,r){\rm d}E}{\int_2^{10} EF^{\rm Quiescent}_{\rm pn}(E,r){\rm d}E} \\ =& \xi^{\rm Flare}_{\rm CR,Det/pn}(r) \frac{\int_2^{10} F^{\rm Flare}_{\rm pn}(E,r){\rm d}E}{\int_2^{10} F^{\rm Flare}_{\rm Det}(E,r){\rm d}E} \times \\ & \frac{\int_2^{10} EF^{\rm Quiescent}_{\rm Det}(E,r){\rm d}E}{\int_2^{10} EF^{\rm Quiescent}_{\rm pn}(E,r){\rm d}E}. \end{aligned} \tag{2.11}$$

With the best-fit quiescent state Γ_2, we obtain $\xi^{\rm Quiescent}_{\rm E}$s and list them in the fourth column of Table 2.10. We couple the MOS L parameter to that of pn with the scale factor $\xi^{\rm Quiescent}_{\rm E}$ to fit the L profiles simultaneously. The best-fit L_0 of pn is $(9.5\pm0.2)\times10^{37}W$. We plot this set of luminosity models with dashed lines in Fig. 2.17.

The systematic errors of radial luminosity models include two parts: one is the offset between the measured model (solid lines) and the empirical model on the basis of the Lockman Hole observation (dashed lines); another is from the intrinsic scatter that makes the $\chi^2/{\rm d.o.f.}$ of each profile in Fig. 2.17 larger than 1.

The offset systematic errors, $\eta_{\rm off}$, are calculated using the formula $\eta_{\rm off} = |L_0^{\rm dashed} - L_0^{\rm solid}|/L_0^{\rm solid}$. The intrinsic systematic errors, $\eta_{\rm in}$, are calculated such that

$$\sum_i \frac{\left(L_i - \hat{L}_i\right)^2}{\sigma_i^2 + \eta_{\rm in}^2 L_i^2} = {\rm d.o.f.}, \tag{2.12}$$

where $\hat{L}_i$ is the model luminosity at the ith point. The total systematic errors are then $\eta^2_{\rm total} = \eta^2_{\rm off} + \eta^2_{\rm in}$. We list the offset, intrinsic, and total systematic errors in the fifth to seventh columns of Table 2.10.

We apply the self-calibrated soft proton model to spectra from regions of interest. Parameters E_0 and b are fixed based on the values in Table 2.8. Γ_2 is fixed given in Table 2.10. L is fixed to the value calculated from the vignetting function 2.8 with β values from Table 2.9 and normalisation values from the column L_0 in 2.10.

2.C Cosmic X-ray background

Thanks to the *Chandra* observation, we are able to study the $\log N - \log S$ relationship of point sources in the Abell 3411-3412 field. The result can

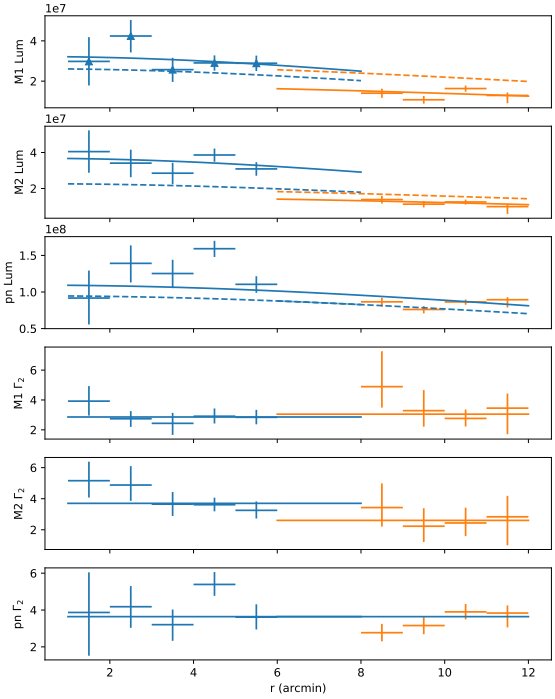

Figure 2.17: Radial profiles of L and Γ_2 from the Abell 3411 observation. Blue points are from the centre MOS CCD region and orange points are from the outer MOS CCDs region. The best-fit radial models are plotted with lines.

help us to constrain the *XMM-Newton* point-source detection limit and to optimise point-source exclusion in the *Suzaku* analysis.

2.C.1 Point-source flux and the $\log N - \log S$ relation

We use `wavdetect` to detect point sources in this field. An exposure-weighted PSF map is provided for source detection. The wavelet size is set as 1.0, 2.0, and 4.0. The task returns 147 sources in total. After visual inspection, 113 sources are left. We use `roi` to extract source and background regions for each point source. The background regions are set as elliptical annuli from 1.5 to 2.0 times the source radius. We extract spectra for each source from each observation using the task `specextract`. A point source aperture correction is applied. For each point source, all source and background spectra, as well as response files from each observation, are

Table 2.10: Best-fit parameters and systematics of quiescent state soft proton components.

	L_0 (10^{37}W)	Γ_2	$\xi_{\rm E}^{\rm Quiescent}$	$\eta_{\rm off}$	$\eta_{\rm in}$	$\eta_{\rm total}$
MOS1 CCD1	3.22 ± 0.25	2.86 ± 0.26	0.29	0.19	0	0.19
MOS2 CCD1	3.68 ± 0.24	3.70 ± 0.29	0.34	0.38	0	0.38
MOS1 CCD 2-7	1.78 ± 0.12	3.05 ± 0.46	0.16	0.58	0.15	0.60
MOS2 CCD 2-7	1.54 ± 0.12	2.60 ± 0.58	0.14	0.30	0	0.30
pn	10.94 ± 0.28	3.64 ± 0.20	1.00	0.13	0.18	0.22

combined by `combine_spectra`. We model each point source spectrum with an absorbed power-law model. The energy range 0.5 – 7.0 keV is used for spectral fitting. We fit spectra with both a fixed $\Gamma = 1.41$ and a free Γ. If the relative error of Γ is less than 10%, we adopt the best-fit Γ and the corresponding flux. We exclude sources with zero fitted flux or $\Gamma > 5$ and compile the rest 101 sources into a catalogue.

To check the $\log N - \log S$ relation of our sample, we plot the cumulative source number curve in Fig. 2.18. The $\log N - \log S$ relationship from the Chandra Deep Field South (CDF-S) has been well studied by Lehmer et al. (2012). X-ray point sources in the range $10^{-15} < S < 10^{-13}$ (erg s^{-1} cm^{-2}) are dominated by AGNs (including X-ray binaries), and their distribution can be expressed by a broken power law,

$$\frac{{\rm d}N}{{\rm d}S} = \begin{cases} K(S/S_{\rm ref})^{-\beta_1} & (S \leqslant f_b) \\ K(f_b/S_{\rm ref})^{\beta_2-\beta_1}(S/S_{\rm ref})^{-\beta_2} & (S > f_b) \end{cases}, \tag{2.13}$$

where $S_{\rm ref} = 10^{-14}$ erg s^{-1} cm^{-2}, and $f_b = 6.4 \pm 1.0 \times 10^{-15}$ erg s^{-1} cm^{-2} is the power-law break flux. The power-law index after the break flux is $\beta_2 = 2.55 \pm 0.17$. We plot the total CDF-S cumulative $\log N - \log S$ curve in Fig. 2.18 as well. The normalisation of the Abell 3411-3412 field is higher than that of the CDF-S. To cross check our point source flux analysis, we look up the catalogue compiled by Wang et al. (2016b), which covers the Abell 3411-3412 field. In their work, for each source, the 0.3 – 8.0 keV flux is calculated with a fixed $\Gamma = 1.7$ and a free $n_{\rm H}$. We assume $n{\rm H} = 4.8 \times 10^{20}$ cm^{-2} and convert the 0.3 – 8.0 keV flux to a 2 – 8 keV flux. The cumulative curve from that catalogue is also plotted. Though the methods of point-source flux calculation are different from our work, the $\log N - \log S$ curve is consistent with ours at the faint end. At the bright end, the discrepancy is due to the assumptions for flux calculation. The consistency of results

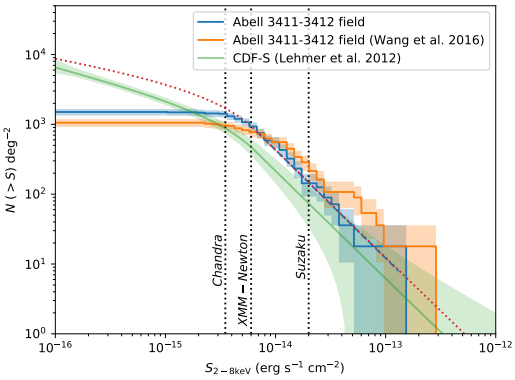

Figure 2.18: $\log N - \log S$ curve from *Chandra* observations. The blue steps are from our analysis of the Abell 3411-3412 field. The best-fit power law is plotted as a blue dashed line. The model we assume to calculate the unresolved CXB in this field is shown as the red dotted line. The orange steps are from the Wang et al. (2016b) catalogue of this field. As a comparison, the curve from CDF-S is plotted as a green line. The error of the CDF-S curve includes both Poisson error and the uncertainties on the best-fit parameters. The detection limits of *Chandra* and *XMM-Newton* as well as the *Suzaku* point-source exclusion limit in this paper are marked as vertical dotted lines.

from two independent analyses proves that in this field, the number of point sources is much higher than the average value in the CDF-S. We fit our cumulative curve from 6×10^{-15} to 1×10^{-13} erg s^{-1} cm^{-2} using a single power-law model with a fixed cumulative index $\alpha = \beta_2 + 1 = 1.55$. The ratio between our normalisation to that from CDF-S is $K_{\rm A3411}/K_{\rm CDF-S} = 2.03 \pm 0.03$.

2.C.2 Detection limit and CXB flux

From the cumulative $\log N - \log S$ curve, the *Chandra* detection limit in this field is $\sim 3.5 \times 10^{-15}$ erg s^{-1} cm^{-2}. The detection limit of *XMM-Newton* is 6×10^{-15} erg s^{-1} cm^{-2}; see Sect. 2.4.1 for details. The *Suzaku* detection limit is much higher because of the large PSF radius of $r_{\rm HEW} = 1'$. Excluding more point sources would make the spectrum fitting less biased by unresolved sources but would decrease the signal statistics at the same time. We exclude from the *Suzaku* analysis only point sources detected by

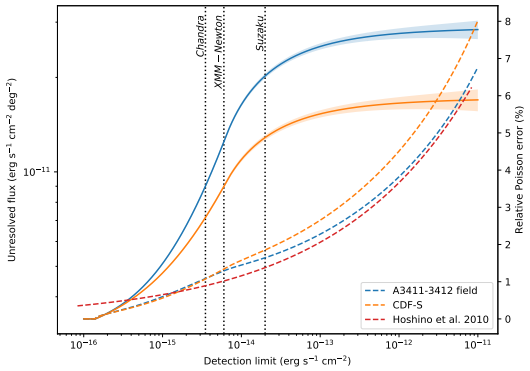

Figure 2.19: Unresolved CXB flux in the 2 – 8 keV band as a function of the point-source detection limit. The curves of CDF-S and our field are plotted with orange and blue lines, respectively. Dashed lines indicate the relative poisson error for 1 deg^2 sky area.

Chandra with a flux above 2×10^{-14} s^{-1} cm^{-2}. Point source coordinates are from the compiled *Chandra* catalogue. We inspect the chosen sources on the flux maps and additionally include two sources. One is a super-soft source (130.527°, -17.569°) whose photon index $\Gamma = 3.8$ causes the 2 – 8 keV flux $F = 7.2 \times 10^{-15}$ erg s^{-1} cm^{-2} to be below our exclusion limit. Another one is (130.561°, -17.657°), which is just at the edge of the *Chandra* field, but the source is bright in the *XMM-Newton* flux map. We shift all source coordinates to match the *Suzaku* astrometry.

The unresolved point source flux from CXBTools [8] is based on the $\log N - \log S$ relation from the work of Lehmer et al. (2012). As we have find the point source density in our field is twice higher than that of CDF-S, we need to take that into account to estimate the unresolved CXB level of *XMM-Newton* and *Suzaku* spectral components properly. The number density of point sources below the *Chandra* detection limit is unknown, but we speculate the $\mathrm{d}N/\mathrm{d}S$ curve of our field will converge into the curve of CDF-S when S is small. We assume the convergent point is $S_{\mathrm{cov}} = 1.4 \times 10^{-16}$ erg s^{-1} cm^{-2} , and at the breaking point of Lehmer et al. (2012)'s curve f_{b}, the differential curve normalisation is twice that of the curve from CDF-S. We

[8] `http://doi.org/10.5281/zenodo.2575495`

can express this relationship with the equation as below:

$$\left(\frac{\mathrm{d}N}{\mathrm{d}S}\right)_{\mathrm{CDF-S}}(S_{\mathrm{cov}}) = 2 \times \left(\frac{\mathrm{d}N}{\mathrm{d}S}\right)_{\mathrm{CDF-S}}(S_{\mathrm{cov}}) \times \left(\frac{S_{\mathrm{cov}}}{f_{\mathrm{b}}}\right)^{\alpha}. \quad (2.14)$$

The solution of the function is $\alpha = 0.18$. Therefore, in our field, the differential $\log N - \log S$ relation is

$$\left(\frac{\mathrm{d}N}{\mathrm{d}S}\right)_{\mathrm{A3411}} = 2 \times \left(\frac{\mathrm{d}N}{\mathrm{d}S}\right)_{\mathrm{CDF-S}} \times \begin{cases} \left(\frac{S}{f_{\mathrm{b}}}\right)^{0.18} & (S_{\mathrm{cov}} \leqslant S < f_{\mathrm{b}}) \\ 1 & (S \geqslant f_{\mathrm{b}}) \end{cases}, \quad (2.15)$$

and the unit of source flux is erg s^{-1} cm^{-2}. The cumulative curve of this modified $\log N - \log S$ model is plotted as the red dotted line in Fig. 2.18.

We apply the differential $\log N - \log S$ relation to estimate unresolved CXB flux in this paper. The unresolved CXB flux and its Poisson uncertainty can be expressed as

$$F(S < S_{\mathrm{lim}}) = A\left[F(S < S_{\mathrm{cov}}) + \int_{S_{\mathrm{cov}}}^{S_{\mathrm{lim}}} S\left(\frac{\mathrm{d}N}{\mathrm{d}S}\right)_{\mathrm{A3411}} \mathrm{d}S\right] \quad (2.16)$$

$$\sigma_F^2 = A\int_{S_{\mathrm{cov}}}^{S_{\mathrm{lim}}} S^2\left(\frac{\mathrm{d}N}{\mathrm{d}S}\right)_{\mathrm{A3411}} \mathrm{d}S, \quad (2.17)$$

where the unresolved flux below 1.4×10^{-16} erg s^{-1} cm^{-2} is 3.4×10^{-12} erg s^{-1} cm^{-2} deg^{-2} (Hickox & Markevitch 2006), and A is the sky area of the selection region. The unresolved flux as a function of the detection limit is plotted in Fig. 2.19 together with the relative error for a 1 deg^2 sky area. For comparison, we over-plot the empirical relative error curve from Hoshino et al. (2010).

We note that for *XMM-Newton* data analysis, the actual CXB residual luminosity is not uniform due to the ICM emission. The detection limit extends to fainter point sources further out in radius as the ICM emission decreases. The point source sensitivity (in cgs units) can be expressed as

$$F = 1.609 \times 10^{-9}\bar{E}\frac{S^2}{2At}\left(1 + \sqrt{1 + \frac{4BP}{S^2}}\right), \quad (2.18)$$

where $\bar{E}$ is the averaged photon energy, S the signal-to-noise ratio, A the effective area, t the exposure time, B the background counts per PSF beam,

and P the PSF size. We use a quadratic function to model the radial increase of the PSF size and use a linear function to model the vignetting effect. The background B in the formula is composed of the cluster emission and other background components. The cluster emission is modelled by a β model (see Eq.2.8). The estimated 2D standard deviation of the residual CXB flux inside $10'$ is $\sim 12\%$. As a comparison, based on the uncertainty curve in Fig. 2.19, the CXB uncertainty contributed by the cosmic variance in a 3 arcmin^2 selection region is $\sim 45\%$ and this value will be larger in a smaller selection region. Therefore, we only take the cosmic variance into account. For *Suzaku* data analysis, we adopt the point-source exclusion limit based on the Chandra point-source catalogue, and can therefore assume a uniform residual CXB flux.

3 Deep *Chandra* observations of merging galaxy cluster ZwCl 2341+0000

X. Zhang, A. Simionescu, C. Stuardi, R.J. van Weeren, H.T. Intema, H. Akamatsu, J. de Plaa, J.S. Kaastra, A. Bonafede, M. Brüggen, J. ZuHone and Y. Ichinohe

(Astronomy & Astrophysics, Volume 656, A59)

Abstract

Context: Knowledge of X-ray shock and radio relic connection in merging galaxy clusters has been greatly extended in terms of both observation and theory over the last decade. ZwCl 2341+0000 is a double-relic merging galaxy cluster; previous studies have shown that half of the southern relic is associated with an X-ray surface brightness discontinuity, while the other half not. The discontinuity was believed to be a shock front. Therefore, it is a mysterious case of an only partial shock-relic connection.

Aims: By using the 206.5 ks deep *Chandra* observations, we aim to investigate the nature of the southern surface brightness discontinuity. Meanwhile, we aim to explore new morphological and thermodynamical features.

Methods: We perform both imaging and spectroscopic analyses to investigate the morphological and thermodynamical properties of the cluster. In addition to the X-ray data, we utilize the GMRT 325 MHz image and JVLA 1.5 GHz and 3.0 GHz images to compute radio spectral index maps.

Results: Surface brightness profile fitting and the temperature profile suggest that the previously reported southern surface brightness discontinuity is better described as a sharp change in slope or as a kink. This kink is likely contributed by the disrupted core of the southern subcluster. The radio spectral index maps

show spectral flattening at the south-eastern edge of the southern relic, suggesting that the location of the shock front is 640 kpc away from the kink, where the X-ray emission is too faint to detect a surface brightness discontinuity. We update the radio shock Mach number to be $\mathcal{M}_{\rm radio,S} = 2.2 \pm 0.1$ and $\mathcal{M}_{\rm radio,N} = 2.4 \pm 0.4$ for the southern and northern radio relics based on the injection spectral indices. We also put a 3σ lower limit on the X-ray Mach number of the southern shock to be $\mathcal{M}_{\rm X\text{-}ray,S} > 1.6$. Meanwhile, the deep observations reveal that the northern subcluster is in a perfect cone shape, with a ~ 400 kpc linear cold front on each side. This type of conic subcluster has been predicted by simulations but is observed here for the first time. It represents a transition stage between a blunt-body cold front and a slingshot cold front. Strikingly, we found a 400 kpc long gas trail attached to the apex of the cone, which could be due to the gas stripping. In addition, an over-pressured hot region is found in the south-western flank of the cluster.

3.1 Introduction

As the nodes of the large-scale structures in the Universe, galaxy clusters grow hierarchically by accreting gas from cosmic filaments and merging with subclusters. Major galaxy cluster mergers are the most dramatic events in the Universe, releasing energies of up to 10^{64} erg. During the merger, the intracluster medium (ICM) that belongs to each subcluster is mixed and shows a disturbed X-ray morphology. Two types of surface brightness jumps, shock fronts and contact discontinuities, are discovered in both observations (e.g., Vikhlinin et al. 2001; Markevitch et al. 2002; Owers et al. 2009; Ghizzardi et al. 2010; Botteon et al. 2018) and simulations (e.g., Ascasibar & Markevitch 2006; ZuHone 2011) of merging clusters.

Since the first report of the association of an X-ray shock and a radio relic (Finoguenov et al. 2010) – which is a type of morphologically elongated, spectrally steep, and polarized diffuse radio source observed in galaxy cluster peripheries – dozens of radio relics have been confirmed to be associated with shock fronts (see the review of van Weeren et al. 2019). The Mach number of shock fronts can be estimated either by radio observations based on the assumption of the diffusive shock acceleration (DSA) theory (e.g., Krymskii 1977; Bell 1978a; Blandford & Ostriker 1978) or by X-ray observations based on the Rankine-Hugoniot condition (Landau & Lifshitz 1959). The Mach numbers estimated from radio observations are systematically higher than those based on X-ray observations (van Weeren et al. 2019), which could be due to the projection effects (Hong et al. 2015) or the propagation of shocks through a magnetized turbulent ICM (Dominguez-Fernandez et al. 2021). Nevertheless, most of the merging shocks are in low Mach numbers ($\mathcal{M} \lesssim 3$), which challenge the acceleration efficiency of the current DSA theory. Therefore, galaxy clusters are unique laboratories for investigating the particle acceleration of weak shocks.

In contrast to shock fronts, contact discontinuities, also known as cold fronts, are sharp surface brightness and temperature edges that hold pressure equilibrium. The cold fronts in merging clusters are usually "remnant core" cold fronts (Tittley & Henriksen 2005), that is, the cores of the original subclusters, and are undergoing ram-pressure stripping (Gunn & Gott 1972). Typically, the remnant cores are in the shape of blunt bodies, for example, Bullet Cluster (Markevitch et al. 2002) and Abell 2146 (Russell et al. 2010). By studying the cold fronts with the subarcsecond spatial resolution of *Chandra*, knowledge of transport processes and the effect of mag-

netic fields in the ICM has been well developed (Markevitch & Vikhlinin 2007; Zuhone & Roediger 2016).

ZwCl 2341+0000 ($z = 0.27$) is a merging galaxy cluster that hosts radio relics in its southern and northern peripheries (van Weeren et al. 2009). The presence of the double relics usually suggests a binary merger with a simple merging geometry and a small angle between the merging axis and the plane of the sky. This merging axis angle was later confirmed to be $10^{\circ}{}^{+34}_{-6}$ by Benson et al. (2017). The diffuse radio emission of ZwCl 2341+0000 was first reported by Bagchi et al. (2002) in the 327 MHz Very Large Array (VLA) image and 1.4 GHz NRAO VLA Sky Survey (NVSS) image. The two relics (denoted RN and RS) were later resolved in Giant Metrewave Radio Telescope (GMRT) 610 MHz, 241 MHz, and 157 MHz observations, where the radio halo is absent (van Weeren et al. 2009). The southern relic consists of three different components (RS1–3). By using a VLA 1.4 GHz D-configuration observation, Giovannini et al. (2010) discovered large-scale filamentary diffuse emission along the entire cluster after removing point sources, which implies the possible presence of a radio halo. In optical frequencies, the galaxy distribution is NW-SE elongated. The dynamical mass of the system was first estimated to be $\sim$ 1–3$\times 10^{15}\ M_{\odot}$ (Boschin et al. 2013). Later, Benson et al. (2017) pointed out that the dynamical mass is biased in this complex merging system, and, by using weak lensing, they reported a mass estimation of $(5.57 \pm 2.47) \times 10^{14}\ M_{\odot}$, which is consistent with the mass estimation made using the Sunyaev-Zeldovich (SZ) effect by *Planck*, $M_{\rm SZ} = (5.2 \pm 0.4) \times 10^{14}\ M_{\odot}$ (Planck Collaboration et al. 2016). Moreover, the optical analysis favors a three-subcluster model by using the Gaussian mixture model method, where a third subcluster with a different redshift ($z = 0.27432$) is spatially overlaid on the northern subcluster. The northern and southern subclusters are at redshifts of 0.26866 and 0.26844, respectively (Benson et al. 2017).

Ogrean et al. (2014) studied the radio-X-ray connection at the radio relics using *Chandra* and *XMM-Newton* observations. They detected X-ray surface brightness discontinuities at both the southern and northern radio relics. The discontinuities were believed to be shock fronts, although spectral analysis was not possible due to the shallow observations. Ogrean et al. (2014) also found that only half of the southern radio relic is associated with X-ray surface brightness discontinuities. This was the original intention of obtaining the additional observations that are presented in this paper. The deep *Chandra* observations not only unravel the previous

mystery but also reveal new striking morphological features, for example, a cone-shaped subcluster that is predicted by simulations but had never before been observed. These new discoveries are explicitly described and discussed in the subsequent sections.

In this paper we present the results of the deep *Chandra* observations of ZwCl 2341+0000. In addition, we utilized radio observations performed with the GMRT at 325 MHz as well as the Jansky Very Large Array (JVLA) L-band (1–2 GHz) B and C configurations and S-band (2–4 GHz) C and D configurations (published by Benson et al. 2017) to compute spectral index maps and probe the properties of the shock fronts. The organization of this paper is as follows. In Sect. 3.2 we present the details of the X-ray and radio observations, data reduction and data analysis. The detailed analysis results for each region of interest are presented in Sect. 3.3. We discuss and conclude the work in Sects. 3.4 and 3.5. We adopt a Lambda cold dark matter universe with cosmological parameters $\Omega_\Lambda = 0.7$, $\Omega_0 = 0.3$, and $H_0 = 70$ km s^{-1} Mpc^{-1}. At $z = 0.27$, one arcminute corresponds to a physical size of 248 kpc.

3.2 Observations and data analysis

3.2.1 Chandra X-ray data

ZwCl 2341+0000 was observed by the *Chandra* Advanced CCD Imaging Spectrometer (ACIS) five times (see Table 3.1 for details). We used the Chandra Interactive Analysis of Observations (CIAO) v4.12 (Fruscione et al. 2006) and CALDB v4.9.2 for data reduction. All level-1 event files were reprocessed by the task `chandra_repro` with VFAINT mode background event filtering. Flare state events were filtered from the level-2 event files by using `lc_clean`. The total filtered exposure time is 206.5 ks.

We used stowed background files to estimate the non-X-ray background (NXB). All stowed background event files are combined and reprocessed by the task `acis_process_events` using the latest gain calibration files. The stacked stowed background of each ACIS-I chip has a total exposure time of 1.02 Ms. For each ObsID, we scaled the NXB such that the 9-12 keV count rate matches the observation. The uncertainty of each scaling factor is calculated as the standard deviation of the scaling factors of individual ACIS-I chips, which is listed in the last column of Table 3.1.

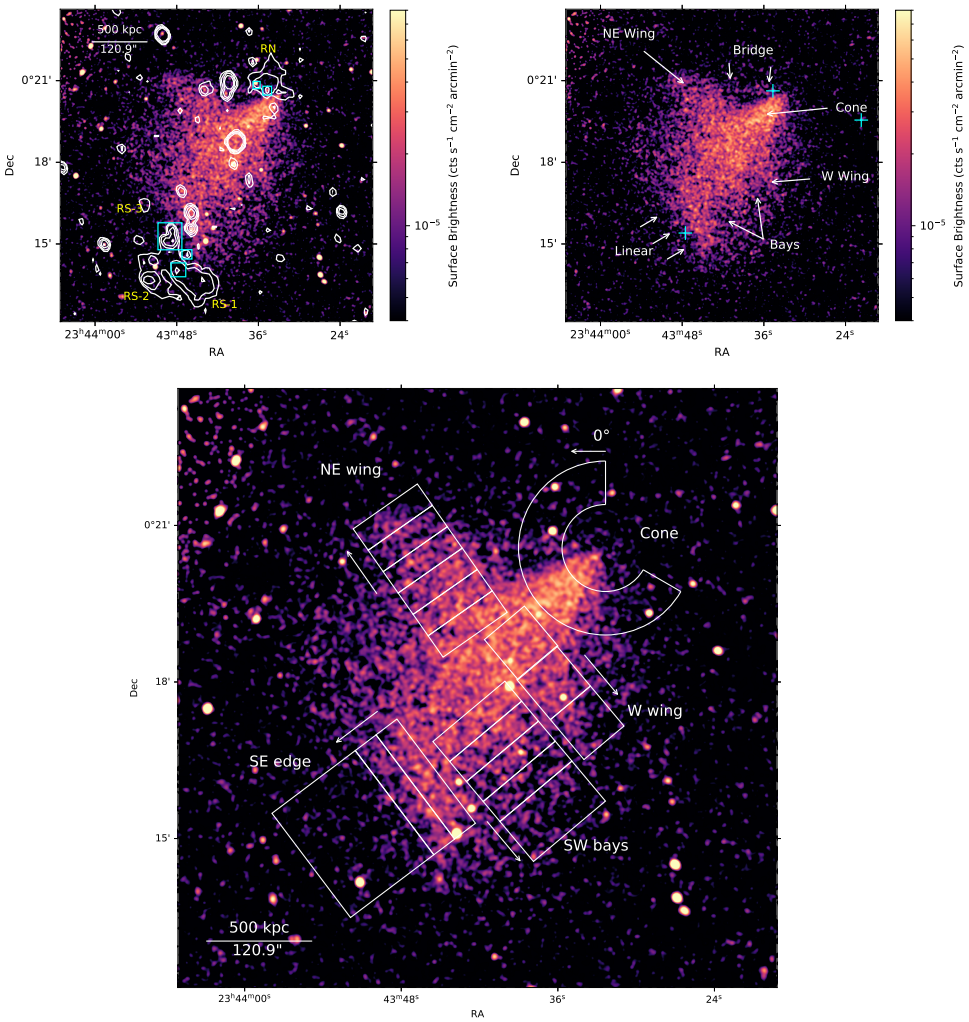

Figure 3.1: *Top left:* X-ray flux map in the 0.5–2.0 keV band convolved with a $\sigma = 1.97''$ (four pixel) Gaussian kernel. Overlaid are the JVLA C-array 1.5 GHz radio contours at $[1, 2, 4] \times 0.075$ mJy beam^{-1}. The terms of the relic sources RS-1–3 and RN are introduced by van Weeren et al. (2009). Identified point sources that overlap with the southern relic are marked by cyan boxes. *Top right:* Image from which point sources have been removed. Surface brightness features are labeled. The locations of the three brightest cluster galaxies adopted from Benson et al. (2017) are marked as cyan crosses. *Bottom:* Extraction regions used for detailed X-ray analysis in Sect. 3.3. For the regions SE edge, SW bays, western wing, and NE wing, the individual temperature bins in Fig. 3.6 are plotted. The arrows beside each bin indicate the directions of the profiles.

Table 3.1: Details of the *Chandra* observations.

ObsID	Instrument	Mode	Pointing (RA[°], Dec[°], Roll[°])	Filtered Exposure (ks)	NXB scaling factor [a]
5786	ACIS-I	VFAINT	(355.93, 0.29, 290)	26.6	0.909 ± 0.016
17170	ACIS-I	VFAINT	(355.91, 0.32, 291)	23.5	0.889 ± 0.008
17490	ACIS-I	VFAINT	(355.93, 0.28, 295)	108.2	0.832 ± 0.004
18702	ACIS-I	VFAINT	(355.91, 0.32, 291)	23.4	0.881 ± 0.017
18703	ACIS-I	VFAINT	(355.91, 0.32, 295)	24.8	0.914 ± 0.032

[a] The scaling factor is defined as $f_{\rm obs}/f_{\rm bkg}$, where the $f_{\rm obs}$ and $f_{\rm bkg}$ are the 9–12 keV count rate in the observation set and in the stacked background set, respectively

Table 3.2: Details of the radio observations.

Telescope	Project ID	Frequency (MHz)	Band width (MHz)	Configuration	Time on source (hr)	Beam size ($''$)	$\sigma_{\rm rms}$ (mJy beam^{-1})
GMRT	20-061	325	33	-	22.67	10.7×8.7	7.0×10^{-2}
JVLA	17A-083	1500	1000	C	1.59	15.1×11.1	3.0×10^{-2}
	SG0365	1500	1000	B	2.27	4.7×3.4	1.2×10^{-2}

Imaging analysis

We extracted and combined the 0.5–2.0 keV count images using `merge_obs`. The exposure maps are calculated using a weighted spectrum file generated by `make_instmap_weighted`, where the spectral model is a single Astrophysical Plasma Emission Code (APEC) model with $kT = 5$ keV, which is the averaged temperature measured by *Suzaku* (Akamatsu & Kawahara 2013). The non X-ray background (NXB) count images were generated from the stowed observation files described in Sect. 3.2.1. After applying the combined exposure map to the NXB-subtracted count image, we obtained the final X-ray flux map (see Fig. 3.1).

Point sources were detected from the unbinned count image by using the task `wavdetect` with wavelet scales of 1.0, 2.0, 4.0, 8.0, and 16.0 pixels. The parameter `sigthresh` was set to 10^{-6}. The output region file is used for masking point sources in both imaging and spectral analysis. Meanwhile, we used the task `roi` to generate background regions around detected point sources and used the task `dmfilth` to create an image containing only the diffuse emission. We note that the point source subtracted image can better illustrate the surface brightness features, but the flux in point source regions is interpolated from the ambient background regions, which is not the exact value of the ICM emission at the respective location. Therefore, in both imaging and spectroscopic analyses, we excluded the point sources using the region files from `wavdetect`.

We extracted surface brightness profiles and fitted them using the Sbfit[1] v0.2.0 package (Zhang 2021). The package uses a forward fitting strategy together with C-statistics (Cash 1979).

Spectral analysis

We used the task `specextract` to extract source and NXB spectra and create the corresponding weighted ancillary response files (ARFs) and response matrix files (RMFs). We used the spectral fitting package SPEX v3.06 (Kaastra et al. 1996; Kaastra et al. 2020b) for spectral analysis. The original format spectra and response files were converted to SPEX format by the `trafo` task. We fit the spectra in the 0.5–7.0 keV band. All spectra were optimally binned (Kaastra & Bleeker 2016) and fitted with C-statistics (Cash 1979; Kaastra 2017). The reference proto-solar element abundance table is from Lodders et al. (2009). By using Pyspextools (de Plaa 2020), the

[1] `https://github.com/xyzhang/sbfit`

Table 3.3: X-ray foreground and background components constrained by the RASS and *Chandra* offset spectra.

Spectrum	Component	Flux[a](0.1 – 2.4 keV) 10^{-2} ph s^{-1} m^{-2}	kT keV	Γ
RASS	LHB	3.1 ± 0.3	0.10 (fixed)	-
	GH	3.0 ± 0.4	0.151 ± 0.007	-
Chandra offset	LHB	3.1 (fixed)	0.10 (fixed)	-
	GH	2.4 ± 1.3	0.17 ± 0.02	
	CXB residual	0.69 ± 0.07	-	1.41 (fixed)

[a] The normalizations are scaled to a 1 arcmin^2 area.

NXB spectra were first smoothed by a Wiener filter with a window length of seven spectral channels and then subtracted from the source spectra. We fit the spectra of the five observations simultaneously.

The source spectra are modeled using a spectral component combination of $cie1 + (cie2 + pow) \times hot + cie3 \times red \times hot$, where cie 1–3 are the single temperature collisional ionization equilibrium (CIE) models for the local hot bubble (LHB), galactic halo (GH), and the ICM; for $cie3$, the abundances of elements from Li to Mn are fixed to $0.3Z_\odot$, which is the averaged value of this cluster (see Sect. 3.3.1). While for cie 1 and 2, all abundances are fixed to the proto-solar abundance. The power law model for the cosmic X-ray background (CXB) residual is denoted as "pow" and its photon index is fixed to 1.41. The model red denotes the redshift of the cluster, which is fixed to 0.27. The hot is the CIE absorption model, where the temperature is fixed to 5×10^{-4} keV to represent the absorption from the Galactic neutral gas, and the column density is fixed to $n_\mathrm{H} = 3.7 \times 10^{20}$ cm^{-2}, which is from the tool `nhtot`[2] (Willingale et al. 2013). Details of the modeling of LHB, GH, and CXB residual are described in Sect. 3.2.1.

X-ray background modeling

We used the *ROSAT* All-Sky Survey (RASS) spectra as a reference to study the X-ray foreground components. The spectrum of an $0.3°$–$1.0°$ annulus centered at the cluster was extracted using the ROSAT X-Ray Background Tool (Sabol & Snowden 2019). Similar to the source spectra, we fit the ROSAT background spectrum using a spectral model combination of $cie1 + hot \times (cie2 + pow)$. To solve the degeneracy of the LHB and GH

[2] `https://www.swift.ac.uk/analysis/nhtot/index.php`

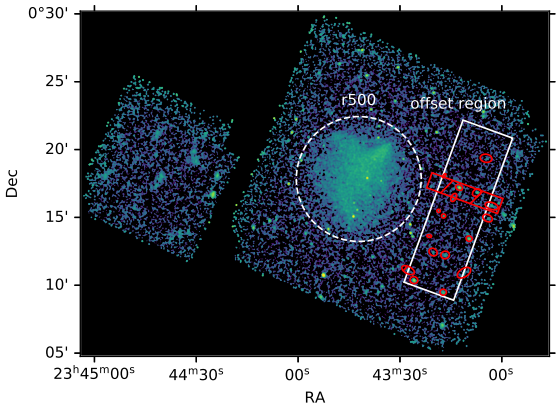

Figure 3.2: Illustration of the offset extraction region, which is the white rectangle. Point-like sources are excluded using red regions, including the red rectangle, which is used to collectively exclude a series of observed clumps. The dashed circle is the r_{500} region of the cluster, which is centered at [23:43:42.1,+00:17:49.9].

temperatures, we fixed the LHB temperature to a typical value of 0.1 keV (e.g., Kuntz & Snowden 2000). The best-fit values are listed in Table 3.3.

Meanwhile, we extracted spectra from an offset region outside the cluster's r_{500} to cross-check the foreground component (see Fig. 3.2). The spectral components are the same as those of the RASS spectrum. Because the effective area of *Chandra* drops dramatically below 1 keV, the LHB component cannot be constrained. We fixed the temperature and normalization of the LHB component to the values of the RASS spectrum. The best-fit results of the *Chandra* offset spectra are listed in Table 3.3 as well. Though with large uncertainties, the normalization as well as the temperature of the GH component are consistent to the values of the RASS spectrum fit. Therefore, in the source spectral analysis, we fixed the parameters of LHB and GH to the values of the RASS spectrum and fixed the parameters of the CXB residual to the value of the *Chandra* offset spectra.

Systematic uncertainty estimation

The GH and CXB residual components as well as the scaling factor of the NXB can introduce uncertainties in the fit results. The best-fit normalization of the GH in the *Chandra* offset spectrum is 20% different from the

value of the RASS spectrum. Therefore, we use 20% to estimate the uncertainty introduced by the GH component. For the CXB residual, converted to the 2–8 keV band, the surface brightness is 1.8×10^{-15} erg s^{-1} cm^2 arcmin^{-2}. Using Eqs. C.4 and C.5 in Zhang et al. (2020) and assuming the $\log N - \log S$ relation is identical to the *Chandra* Deep Field South (Lehmer et al. 2012), the corresponding point source exclusion limit is 3×10^{-15} erg s^{-1} cm^{-2} and the CXB residual uncertainty on a 1 arcmin^2 area is 57%. For any of the spectra in the analysis, the CXB residual uncertainty is scaled from 57% by a factor of $A^{-1/2}$, where A is the extraction area converted from the `backscal` value in the spectrum header. The largest NXB uncertainty amounts to 3% in ObsID 18073; therefore, we conservatively used 3% to estimate the NXB systematic uncertainty for all five observations.

By fitting the spectra extracted inside r_{500}, which include most of the ICM photons, we find that the statistical uncertainty is larger than the systematic uncertainties from the GH and CXB by an order of magnitude, and is larger than the NXB systematic uncertainty by four orders of magnitude. We also checked the systematic uncertainties in two smaller regions, the LK1 and HT3 regions in the thermodynamic maps (see Fig. 3.5), which are in a high and a low surface brightness, respectively. In the LK1 region, the statistical uncertainty is larger than all other systematic uncertainties by over an order of magnitude. In the HT3 region, the systematic uncertainties increase due to the low surface brightness of the ICM emission. Nevertheless, the statistical uncertainty is still a factor of four larger than the systematic uncertainty contributed by GH, and over an order of magnitude higher than other systematic uncertainties. The one-fourth of the additional uncertainty will result in a 3% increase after uncertainty propagation. Therefore, in this work, we only present statistical uncertainties.

Thermodynamic maps

To create spatial bins for temperature, pseudo pressure, and entropy maps, we used the tool `contbin`[3] (Sanders 2006). The signal to noise ratio was set to 30 and the geometric constraint was set to 1.3. The spectra in each spatial bin were fitted following the method in Sect. 3.2.1. Assuming the depth along the line of sight of each bin is 1 Mpc and $n_e/n_{\rm H} = 1.2$, we calculated the ICM number density from the best-fit emission measure. The pseudo pressure is the product of the averaged gas density and the temperature of

[3] `https://github.com/jeremysanders/contbin`

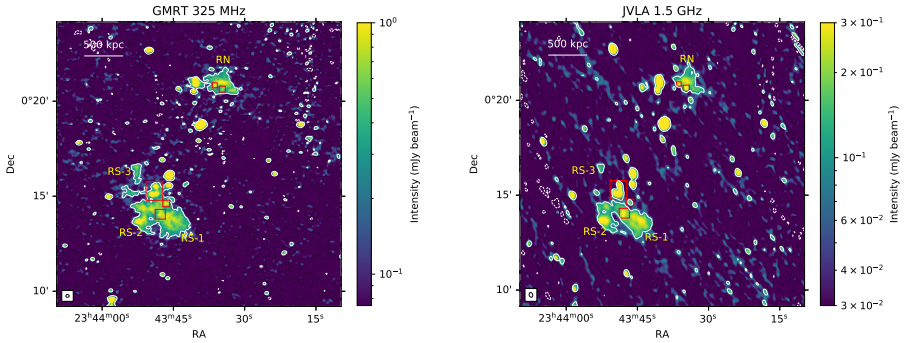

Figure 3.3: GMRT 325 MHz (left) and JVLA 1.5 GHz C-configuration (right) radio maps of ZwCl 2341+0000, overlaid with contours at the $3\sigma_{\rm rms}$ (solid) and $-3\sigma_{\rm rms}$ (dashed) levels. The beam sizes are plotted at the bottom-left corner of each image. Identified point sources that overlap with the southern relic are marked by red boxes.

each bin. The entropy is calculated using the definition $K = kTn_e^{-2/3}$.

3.2.2 GMRT and JVLA radio data

We use the GMRT 325 MHz observations (project ID 20-061) and the JVLA L-band observations (1-2 GHz band and 1.5 GHz central frequency) in B (project ID SG0365) and C (project ID 17A-083) configurations. The details of the observations are listed in Table 3.2.

Data reduction

The GMRT data were reduced and imaged by using the SPAM package (Intema 2014), which is a set of AIPS-based data reduction scripts that includes ionospheric calibration (Intema et al. 2009). The JVLA data were reduced using the Common Astronomy Software Applications (CASA) package 5.6.2. The B-configuration data were calibrated following the procedures of van Weeren et al. (2016b). The C-configuration data were preprocessed by the VLA CASA calibration pipeline, which performs basic flagging and calibration optimized for Stokes I continuum data. Then, we extracted uncalibrated data and we manually derived final delay, bandpass, gain, and phase calibration tables and applied them to the target. We used the source 3C138 as amplitude calibrator and we imposed the Perley

& Butler (2013) flux density scale. J0016-0015 was chosen as phase calibrator. We removed radio frequency interference (RFI) with CASA statistical flagging algorithms.

The two JVLA data sets were imaged using the multi-scale multifrequency deconvolution algorithm of the CASA task `tclean` (Rau & Cornwell 2011) for wide-band synthesis-imaging. We also used the w-projection algorithm to correct for the wide-field non-coplanar baseline effect (Cornwell et al. 2008). We subtracted out from the visibilities all the sources external to the field of interest ($\sim 15' \times 15'$) to exclude bright sources that could increase the image noise. In order to refine the antenna-based phase gain variations, several cycles of self-calibration were performed. During the last self-calibration cycle, amplitude gains were also computed and applied. In the final images we used a Briggs weighting scheme with the robust parameter set to 0.5. The final images were corrected for the primary beam attenuation using the `widebandpbcor` task in CASA. The residual calibration errors on the amplitude are estimated to be $\sim 5\%$.

The radio relics are visible in the GMRT 325 MHz image and the JVLA L-band C-configuration image (see Fig. 3.3), but are barely detected in the JVLA B-configuration image. Therefore, we only use the B-configuration image for point source identification. In the GMRT 325 MHz image, the component RS-3 is more extended and another diffuse component emerges between the RS-3 and RS-2, suggesting the connection of all individual components.

Spectral index map

Combining the GMRT image at 325 MHz and the JVLA C configuration image at 1.5 GHz we made a spectral index[4] map of the cluster. We convolved the two images to the same Gaussian beam of 15.5 x 15.5 arcsec and excluded pixels below the respective $3\sigma_{\rm rms}$ detection threshold in each image. In our case, the JVLA observation is shallower; therefore, we excluded the pixels in the convolved GMRT image to match the convolved JVLA image. The spectral index image was created using the CASA `immath` task with `spix` mode. The error map image was created propagating the rms noise of each image and the calibration error with the expression:

$$\sigma_\alpha = \frac{1}{\log\left(\nu_1/\nu_2\right)} \times \left[\sigma^2_{\rm sys} + \left(\frac{\sigma_{\nu_1}}{I_{\nu_1}}\right)^2 + \left(\frac{\sigma_{\nu_2}}{I_{\nu_2}}\right)^2\right]^{1/2}, \qquad (3.1)$$

[4] $F \propto \nu^\alpha$

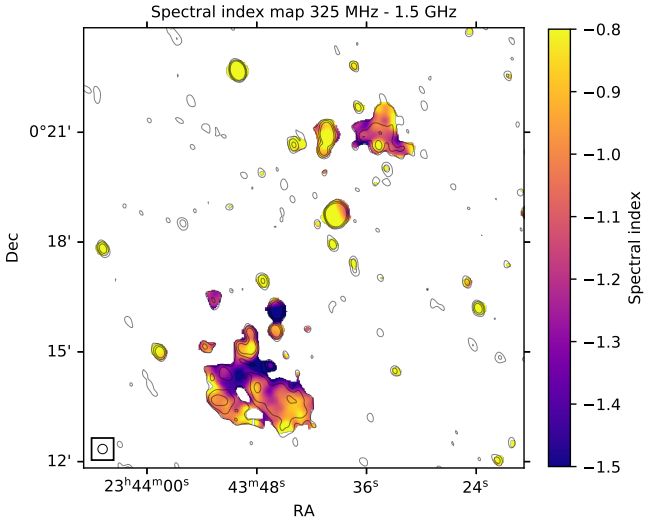

Figure 3.4: Spectral index map between 325 MHz and 1.5 GHz with a resolution of $15.5''$, overlaid with JVLA C-configuration contours.

where ν_1 and ν_2 are the frequencies of the two images, σ_ν is the rms noise of the image and I_ν is the total intensity image at the frequency ν, and $\sigma_{\rm sys}$ is the calibration uncertainty, which is 5% here. The spectral index map between 325 MHz and 1.5 GHz is shown in Fig. 3.4.

The spectral index at the SE edge of the radio relic RS-2 is -1.0. It steepens toward the cluster center down to -1.4. This is the first time the spectral steepening is resolved across the southern relic. However, the steepening in the relic RS-1 is less clear. Most of RS-1 has a flat spectral index of -0.9. The relic RN also shows spectral steepening, but with a gentle gradient. The spectral index decreases from -0.9 at the northern edge to -1.1 at the center.

We also computed a spectral index map between 325 MHz and 3.0 GHz, where the 3.0 GHz image was published by Benson et al. (2017). This map exhibits a similar spectral steepening trend as the spectral map between 325 MHz and 1.5 GHz, but with a lower spatial resolution.

3.3 Results

3.3.1 General X-ray properties

We fit a global spectrum in a circular region with radius r_{500}, derived from the SZ mass ($M_{500,\mathrm{SZ}} = 5.2 \pm 0.4\ M_{\odot}$, Planck Collaboration et al. 2016), and centered at [23:43:42.1, +00:17:49.9], which is close to the pressure peak and the X-ray centroid (see the dashed circle in Fig. 3.2). We obtained $kT = 5.32 \pm 0.18$ keV and $Z = 0.29 \pm 0.07\ Z_{\odot}$, which are consistent with the results of previous Suzaku observation (Akamatsu & Kawahara 2013).

The previous shallow observation already shows that the X-ray emission is NW-SE elongated with substructures of an outbound bullet-like structure at the NW, a tail-like structure at the SE, and an excess emission toward the NE (Ogrean et al. 2014). The deep *Chandra* observations reveal new surface brightness features, which are marked in the top right panel of Fig. 3.1. The NE subcluster is actually a cone-shaped structure, where linear surface brightness edges are on the both sides of the cone. Below the cone, two wings stretch out toward the NE and SW directions, respectively. The apex of the cone is connected to the NE wing by a slim X-ray bridge. A linear surface brightness edge is in the SE direction, which was believed to be associated with the southern radio relic. In the SW direction, different from the SE linear structure, two surface brightness deficit regions are repeatedly shown.

Thermodynamic maps are plotted in Fig. 3.5. We also provide the temperature uncertainty map as in Fig. 3.13. Limited by total counts and the size of the object, the spatial bins are coarse. Nevertheless, the thermodynamic maps still imply possible merging features, for example, shocks, cold fronts, and core remnants, for which we customize the surface brightness and spectral extraction regions for detailed investigation in the following subsections. In the temperature map, there are four regions where the temperatures are higher than the ambient regions, which are labeled as HT1–4. The region HT1 is close to the geometric center of the merging system, while HT1–3 are in relatively low density regions. HT2 is between the NW comet and NE wing, HT3 is outside the SE linear surface discontinuity, and HT4 is coincident with the two bays. In the pseudo pressure map, the pressure smoothly decreases from the HT1 to outer regions. There is no significant pressure jump across the inner edge of the HT2 and HT3 regions. There might be a sharp pressure gradient at the outer edge of the HT4 region and need to be further inspected. The entropy map shows three

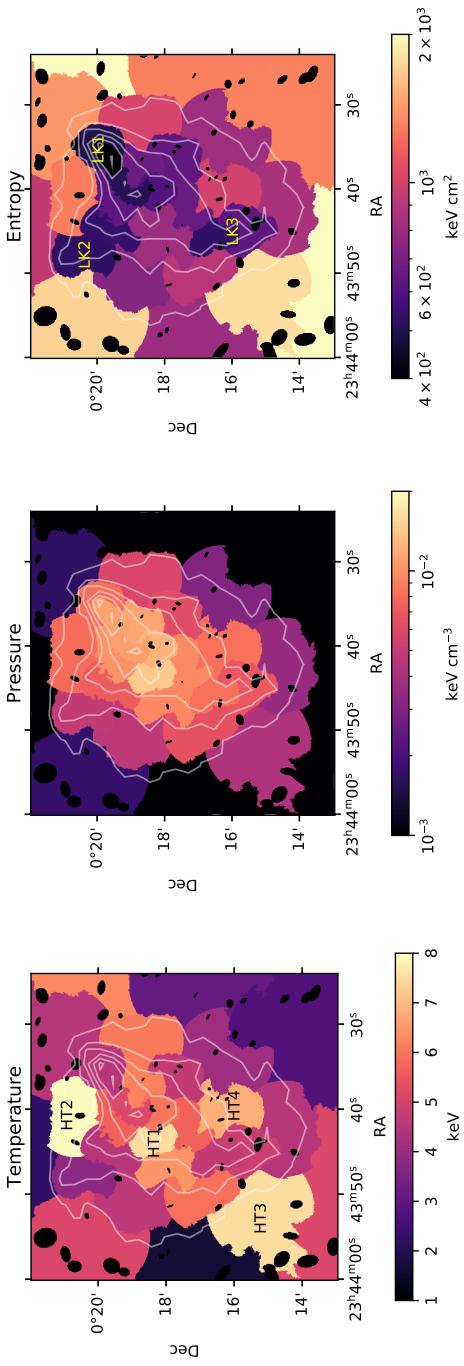

Figure 3.5: Temperature, pseudo pressure, and entropy maps of ZwCl 2341+0000, overlaid with the X-ray surface brightness contours. High temperature and low entropy regions are labeled as HT1–4 and LK1–3, respectively.

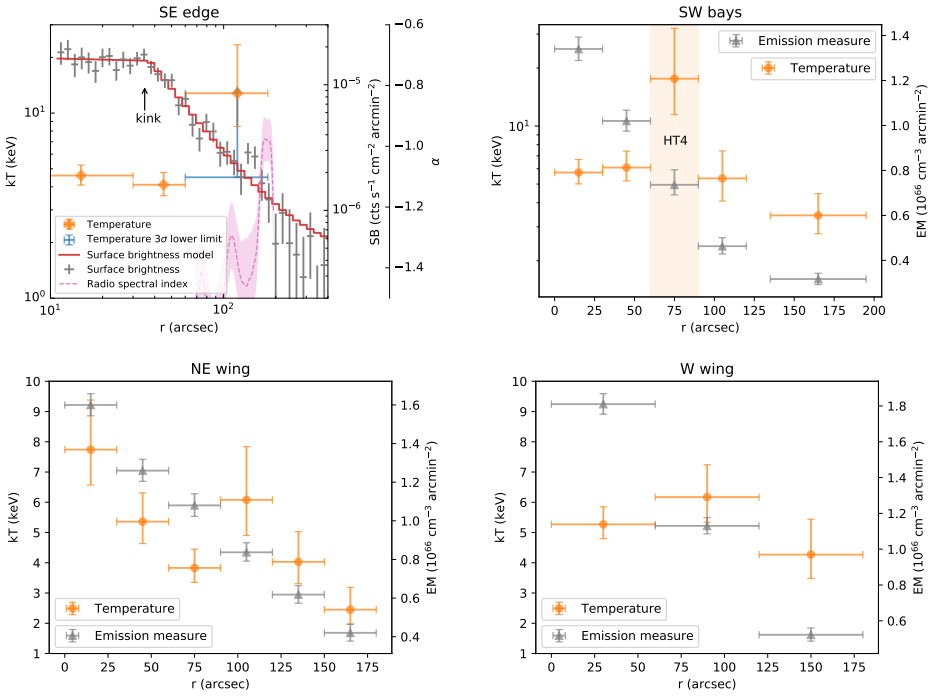

Figure 3.6: Temperature and surface brightness (or emission measure) profiles in the SE edge, SW bays, NE wing, and western wing extraction regions. The region definitions are shown in the bottom panel of Fig. 3.1.

low entropy area, which correspond to the NW outbound cone (LK1), NE wing (LK2), and part of the SE linear structure (LK3). Because convection within clusters transfers low entropy gas to the bottom of gravitational potential wells and high entropy gas to the outskirts (e.g., Voit et al. 2002), low entropy gas is found in the cores of relaxed clusters. Therefore, the low entropy in those regions implies that the origin of the gas is related to cores of subclusters before the merger. The NW cone is a subcluster core being stripped. The SE linear structure is the remnant of a totally disrupted core, which is associated with the subcluster moving toward the SE.

3.3.2 SE edge

We extracted a 0.5–2.0 keV surface brightness profile across the SE linear structure using the region shown in the bottom panel of Fig. 3.1. The surface brightness profiles are plotted in the top left panel of Fig. 3.6. The surface brightness profile is similar to the profile in fig. 3 of Ogrean et al. (2014), but with a factor of 2.4 higher signal to noise ratio. The deep observations reveal that the SE edge does not resemble other textbook examples of surface brightness discontinuities. The surface brightness profile is flat before a kink at $\sim 40''$. After the kink, the surface brightness continuously decreases in a power law until a bump between the radii of $120''$ and $160''$. Although there is a significant change of the slope, there is no clear associated jump of density (see Markevitch & Vikhlinin 2007 for examples with sharp density jumps). The profile can be well fitted by a unprojected broken power law model with $\mathrm{C_{stat}/d.o.f} = 35.4/38$. The best-fit model was plotted as well. While using a single power law model, the fitting statistics is $\mathrm{C_{stat}/d.o.f} = 179.2/40$, which is much worse than using a broken power law, indicating an excess of X-ray emission contributed by a gas clump above the underlying density profile.

Previous work on short observations was unable to explore temperature structures across the edge. With the deep observations, we tentatively search for potential temperature jumps. We plotted the temperature profile in the same panel as the surface brightness profile in Fig. 3.6. The temperature in the $0''$–$30''$ and $30''$–$60''$ bins are 4.6 ± 0.5 keV and 4.1 ± 0.5 keV, respectively, which are slightly below the averaged $kT_{500} = 5.32 \pm 0.18$ keV. After that, it reaches $12.8^{+10.6}_{-4.8}$ keV in the $60''$–$180''$ bin. Outside this bin, the temperature cannot be constrained due to the fast decreasing surface brightness. Based on the temperature profile, there is no evidence for shock heating on the inner side of the kink, which disfavors the previous speculation by Ogrean et al. (2014) that the edge is a shock front.

The existence of an additional gas clump as well as its relatively low temperature suggest that it is the remnant of the core of the southern subcluster, which agrees with the low entropy in the region LK3 (see Fig. 3.5). The high temperature outside the cool clump is likely to be heated by the leading shock. The pattern of a hot post shock region followed by a cool gas clump has been found in many post merger systems, where the cool component could be a remnant core either remains compact (e.g., Bullet Cluster, Markevitch et al. 2002; Markevitch 2006) or has been broken up (e.g., Abell 520, Wang et al. 2016a). In our case, the core remnant is more

diffuse, implying that either the progenitor is not a strong cool core or the diffusion processes has already taken place. We also estimated the 3σ lower limit of the temperature in $60''$–$180''$ bin by using the $\Delta C_{\rm stat} = 9$ criterion. The 3σ lower limit is 4.5 keV. We use this lower limit to constrain the Mach number of the undetected shock that is possible accelerating particles at the outer edge of the southern relic in Sect. 3.4.1.

The location of the shock front is unable to be resolved in X-rays due to the limited photons. Nevertheless, the functions of shocks in terms of particle acceleration shed light on the possible location. We plot the spectral index of the radio relic in the same panel. The radio relic has a relative flat spectrum at the outer edge ($r \sim 200''$) and the spectral index decreases toward the cluster center. Based on the shock-relic connection established for most radio relics (e.g., Finoguenov et al. 2010), the position of the shock coincides with the flat edge, which is about $160''$ (640 kpc) away from the cool gas clump.

3.3.3 SW bays

The locations of the two bays are coincident with a high temperature region in the temperature map (HT4). The gas outside this region has a lower temperature (<4 keV). To locate the hot region in the NE-SW direction and search for possible temperature jumps, we extracted temperature profiles from the merging axis to the SW outskirts, the region configuration is defined in the bottom panel of Fig. 3.1. In addition, we extracted an emission measure profile that presents the trend of surface brightness (see the top right panel of Fig. 3.6). The third bin, ranging from $60''$ to $90''$ and covering most of the area of the two bays, has an extreme high temperature of $17.6^{+14.5}_{-6.1}$ keV, which is a factor of $2.9^{+2.4}_{-1.2}$ higher than the second bin. After this bin, the temperature decreases to the average value of the cluster and reaches 3.4 ± 0.8 keV in the outermost bin.

The third temperature bin in the top right panel of Fig. 3.6 includes both bays. The profile in the NE-SW direction is unable to probe the origin of the hot gas and distinguish the thermodynamic properties of the individual bays. Therefore, we define perpendicular extraction regions along the NW-SE direction (see the left panel of Fig. 3.7). It starts from the western wing and goes through two bays and the remnant of the southern subcluster. The surface brightness and temperature profiles in the western slit region are shown in the right panel of Fig. 3.7. The temperature profile presents entirely different thermodynamic properties of the two bays. While the

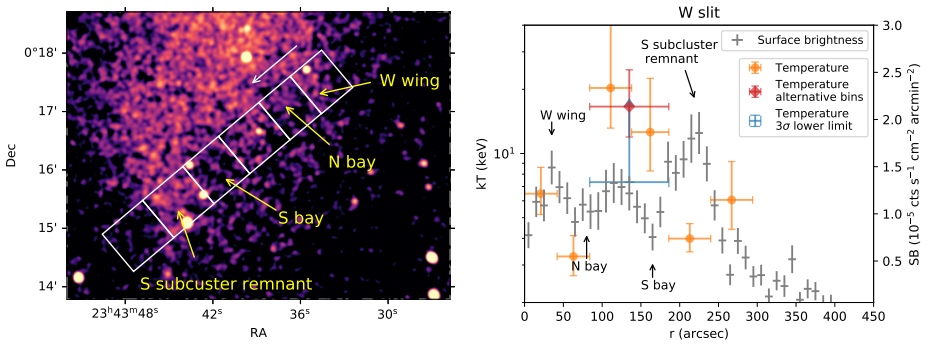

Figure 3.7: *Left:* Zoomed-in view of the western flank of the cluster. Individual temperature bins are plotted in white. The arrow indicates the direction of profiles. *Right:* Temperature and surface brightness profiles extracted from the western slit region.

ICM in the northern bay is 3.3 ± 0.7 keV, the southern bay temperature is $12.6^{+10.0}_{-4.3}$ keV. Furthermore, the ridge between the two bays has the highest temperature in the profile. Considering that the ridge has higher surface brightness than the two bays, which indicates a higher density, together with the high temperature, the gas in the two bays and the ridge does not hold pressure equilibrium. We measure the temperature by combining the two hot bins and obtain a $16.6^{+8.1}_{-4.7}$ keV temperature. Similar to the hot bin in the SE post shock region, we put a 3σ lower limit of 7.3 keV for this bin, which is still a factor of two higher than the temperature in the northern bay.

3.3.4 NE and western wings

The temperature and emission measure profiles of the NE and western wing regions are plotted in the bottom left and bottom right panels of Fig. 3.6, respectively. The spectral extraction regions are designed to ensure at most 20% uncertainty for each temperature measurement. Therefore, we have six bins for the NE wing but only three bins for the western wing.

By visual inspection, we find no significant surface brightness jump across the NE wing, which is supported by the monotonously decreasing emission measure profile. However, the temperature profile exhibits features that are not seen in the surface brightness. The temperature in the

innermost bin is 7.7 ± 1.2 keV, which is consistent with the HT1 region in the temperature map. Until $r = 90''$, the temperature drops monotonously, after which there is a sudden rise from 3.8 ± 0.5 keV to 6.1 ± 1.2 keV, where the jump has a significance of 1.8σ. This plausible temperature enhancement does not correspond to any surface brightness jump. After the jump, the temperature continuously decreases to 2.5 ± 0.5 keV at the wingtip.

On the contrary, the western wing does not show strong temperature variation, though the spatial bins are coarse due to the small size. The temperature at the wingtip is 4.7 ± 0.9 keV, which is closer to the averaged temperature of the cluster than the NE wingtip.

3.3.5 NW cone

The low entropy of the gas in the cone, the higher temperature of the ambient gas, and the equilibrium of the pressure across the cone show that this is an outbound subcluster core. Unlike any other observed remnant core cold front, this remnant core is not in a blunt-body shape, but in a cone shape. On both side of the cone, the cold fronts are linear and with projected lengths of ~ 400 kpc. Unlike typical radial profiles, we extract a radially averaged surface brightness profile using sectors of annulus centered on the apex of the cone. The inner and outer radius are $50''$ and $100''$, respectively (see the bottom panel of Fig. 3.1). We define the azimuthal angle starting from the north and increasing eastward. The 2° binned profile is plotted in the left panel of Fig. 3.8. The bump centered at $\sim 85^\circ$ is the "bridge" connecting the cone and the eastern wing. The surface brightness continuously increases from 100° to 115°. From 115°, which is the left edge of the cone, the surface brightness is relatively flat until a sudden drop at $\sim 150^\circ$. After the drop, the surface brightness is in a plateau for $\sim 15^\circ$ then gradually fades away.

To probe the gas density inside the cone, we tentatively fit the profile using a projected broken power law model. The detailed description of the model and the projection of the conic body is in Appendix 3.D. We first fit the entire profile from 100° to 200° to measure the width of the cone and the position angle of the axis. The center of the cone is at $\theta_{\rm axis} = 135^\circ.6 \pm 0.6$ and the gas density has a break at $\phi_{\rm b} = 19^\circ.9^{+0.7}_{-1.3}$. However, a single component model cannot fit both sides of the conic subcluster well. The left side has a steeper gradient than the right side. Meanwhile, the best-fit power law index inside the cone α_1 is negative, which indicates that the gas density at the edge is higher than the center. Therefore, we fit the

Table 3.4: Best-fit parameters of the surface brightness profiles across the cone.

	$n_{\rm e}$ $10^{-3}{\rm cm}^{-3}$	α_1	α_2	$\phi_{\rm b}$ $^\circ$	C	$\theta_{\rm axis}$ $^\circ$	C-stat / d.o.f
100°–200°	1.71 ± 0.14	-0.22 ± 0.15	0.92 ± 0.13	$19.9^{+0.7}_{-1.3}$	1.56 ± 0.23	135.6 ± 0.6	54.2/44
100°–136°	$1.60^{+0.06}_{-0.10}$	0 (fixed)	1.70 ± 0.4	$20.5^{+3.2}_{-0.6}$	$1.12^{+0.27}_{-0.12}$	136 (fixed)	12.1/14
136°–200°	1.46 ± 0.08	0 (fixed)	0.89 ± 0.12	19.5 ± 1.7	$1.26^{+0.07}_{-0.26}$	136 (fixed)	27.9/28

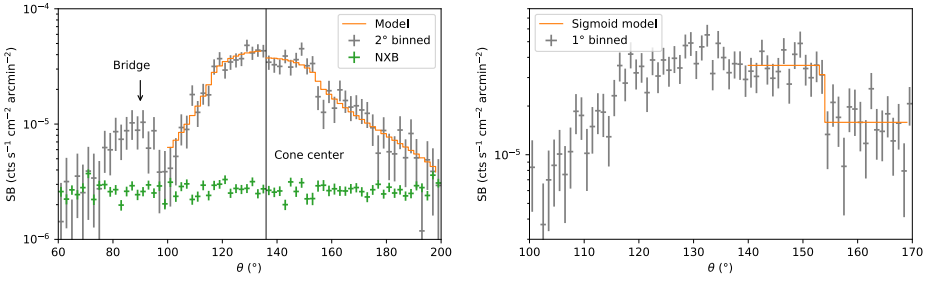

Figure 3.8: *Left:* Azimuthal surface brightness profile with a bin width of 2°. The vertical line is the axis of the cone. The 100°–136° and 136°–200° profiles are fitted separately. *Right:* Zoomed-in view of the profile with a bin width of 1° together with the best-fit sigmoid model from 140°–170°.

$100°$–$136°$ and $136°$–$200°$ profiles separately. The parameter α_1 is fixed to zero to investigate how much the observed profile deviates from a uniform gas distribution. The best-fit parameters of each profile are listed in Table 3.4. The left part can be well fitted with a uniform gas density in the cone. On the right part, the model cannot fit the profile at the jump well. The surface brightness enhancement before the jump indicates a high density shell at the cone edge.

We note that the surface brightness discontinuity on the right side of the axis is sharp. To further quantify the location of the jump, we binned the profile with a width of $1°$ (see the right panel of Fig. 3.8). The jump is at $\sim 154°$ in the $1°$ binned profile. On both sides of the jump, the profiles are flat. We tentatively fit the profile in the $140°$ – $170°$ range to determine the jump location as well as the jump width using a sigmoid model. We adopted the form of error function, which is naturally a Gaussian convolved box function. In our case, the model is

$$S(\theta) = S_0 - \frac{S_{\rm jump}}{2} \times \Phi\left(\frac{\theta - \theta_{\rm jump}}{\sqrt{2}\sigma}\right), \tag{3.2}$$

where S_0 and $S_{\rm jump}$ are profile normalization and jump strength, Φx the error function, $\theta_{\rm jump}$ the jump location, and σ the width of the Gaussian smooth kernel. The best-fit jump location is $154°.2 \pm 0.8$ and the best-fit kernel width is $0°.07^{+2.28}_{-0.07}$.

3.3.6 Bridge and northern outskirts

We extracted the surface brightness profile across the bridge from the white narrow box region (the left half of the yellow broad region) in the left panel of Fig. 3.9. The surface brightness profile is plotted in the right panel of Fig. 3.9. The bridge is located at $r \sim 20''$, after which the surface brightness keeps flat until a plausible jump at $r \sim 100''$. To check the significance of the bridge and the jump, we fit the profile using a compound model that consists of a Gaussian profile and a projected double power law density profile. The best-fit surface brightness of the Gaussian component is $(9.1 \pm 3.0) \times 10^{-6}$ cts s^{-1} cm^{-2} arcmin^{-2}, which means that the gas bridge has a 3σ detection. The best-fit density jump is 1.6 ± 0.6, which is unconstrained due to the limit of counts. However, the best-fit power law index changes from 0.0 ± 0.1 before the jump to $0.8^{+1.0}_{-0.1}$ after the jump. We extracted a surface brightness profile using a broad region (the yellow box in the left panel of Fig. 3.9) to check whether the potential jump is associated with

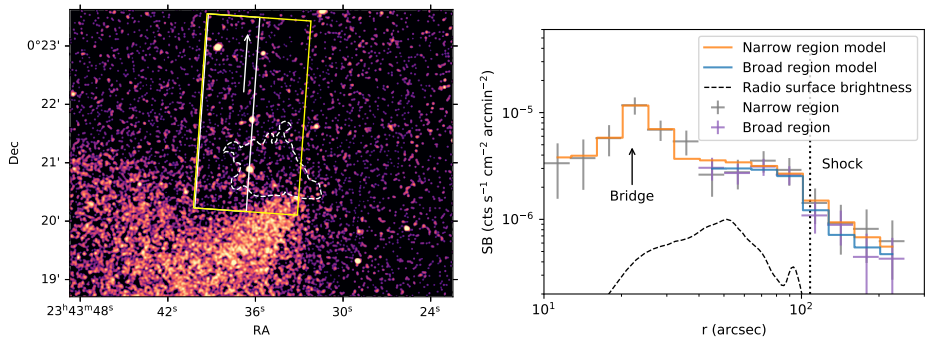

Figure 3.9: *Left:* Narrow (white) and broad (yellow) extraction regions for surface brightness profiles in the northern outskirts. The dashed contour is the northern relic in the GMRT 325 MHz image at the $3\sigma_{\rm rms}$ level. *Right:* Surface brightness profiles and their best-fit model in the narrow and broad regions. The bridge and the surface brightness jump are located at $r = 23''$ and $r = 108''$, respectively. The GMRT 325 MHz profile is plotted with a dashed curve, the outer edge of which is associated with the potential X-ray jump.

the northern relic. The surface brightness in the broad region is plotted in the right panel of Fig. 3.9 as well. The profile has a similar trend as that in the narrow region and the best-fit jump location is $108'' \pm 4$, which is close to the outer edge of the northern relic. The best-fit density jump of the broad region profile is 1.8 ± 1.1, which means that the density jump still cannot be constrained.

3.4 Discussion

3.4.1 Shock fronts and radio relics

By measuring the temperature profile, we discovered that the previous SE surface brightness jump reported by Ogrean et al. (2014) is not a shock but rather a kink contributed by cool gas from the remnant core. Outside the kink, the X-ray surface brightness drops dramatically, preventing us from investigating the exact location of the shock in the X-rays. Nevertheless, at radio frequencies, the 325 MHz - 1.5 GHz spectral index map clearly shows the spectral steepening from the edge toward the cluster center. It is the first time that we see the evidence of shock acceleration and subsequent

radiative cooling of the relativistic plasma in the radio relic of this cluster. The spectrally flat edge of the southern relic, which is $\sim 160''$ away from the kink, is the possible location of the southern shock.

In the northern relic, the spectral index is flat at the northern edge, where the X-ray surface brightness changes its gradient. Although the density jump cannot be constrained, the variation in the gradient at this position suggests that the northern shock that is responsible for (re)accelerating the northern relic is at this position.

Based on the DSA theory, the radio injection spectral index is a function of the Mach number,

$$\alpha_{\rm inj} = \frac{\mathcal{M}^2 + 3}{2\left(\mathcal{M}^2 - 1\right)}. \tag{3.3}$$

Since the spectral index is spatially resolved, this relation can be directly applied to the southern relic, where the injection spectral index is 1.00 ± 0.06. We obtain a radio Mach number $\mathcal{M}_{\rm radio,S} = 2.2 \pm 0.1$. This number is lower than using the integrated spectral index $\alpha_{\rm S,int} = -1.20 \pm 0.18$ (Benson et al. 2017) and assuming the relation between the injection and integrated spectral indices is $\alpha_{\rm int} = \alpha_{\rm inj} - 0.5$ (Kardashev 1962). A theoretical investigation shows that this simple assumption does not hold when the shock is nonstationary, which is the case of cluster merger shocks (Kang 2015). We also applied Eq. 3.3 to the northern relic. The updated radio Mach number $\mathcal{M}_{\rm radio,N} = 2.4 \pm 0.4$.

Meanwhile, the Mach number can be estimated by using the temperature jump based on the Rankine-Hugoniot condition (Landau & Lifshitz 1959),

$$\frac{kT_{\rm post}}{kT_{\rm pre}} = \frac{5\mathcal{M}^4 + 14\mathcal{M}^2 - 3}{16\mathcal{M}^2}. \tag{3.4}$$

The pre-shock region is too faint to measure the temperature. Therefore, we tentatively extrapolate it by using a universal temperature profile (Burns et al. 2010), which remarkably agrees with *Suzaku* observations of galaxy cluster outskirts. The profile is

$$\frac{kT(r)}{kT_{\rm ave}} = (1.74 \pm 0.03) \times \left[1 + (0.64 \pm 0.10) \times \left(\frac{r}{r_{200}}\right)\right]^{-3.2 \pm 0.4}. \tag{3.5}$$

The spectrally flat boundary of the relic is located at $r \sim 0.7 r_{200}$, at which the predicted pre-shock temperature is 2.8 ± 0.6 keV. Because the temperature measurement in the post shock region has a large error bar, we only

put a lower limit for that Mach number. By combining the 3σ lower limit of the post-shock temperature 4.5 keV, we obtain the 3σ lower limit of the X-ray Mach number 1.6. The estimated lower limit of the X-ray Mach number matches the value of the radio Mach number. Because we can only put a lower limit of the X-ray Mach number, it is not clear whether this shock is another case with Mach number discrepancy between the X-ray and the radio. Unfortunately, in the X-ray, the temperature between the bridge and the potential jump in the northern outskirts (see Fig. 3.9) is not constrained.

3.4.2 Conic subcluster

The shapes of the subclusters in other merging systems usually show a spheroid core, and the surface brightness decreases radially from the center of the core. As an exception, the subcluster in ZwCl 2341+0000 does not have a concentrated surface brightness peak and the radius of curvature at the apex can be limited to be less than 30 kpc. As a comparison, the straight cold fronts on both sides have lengths of 400 kpc. Meanwhile, by using a surface brightness profile fit, we estimated that the gas density at the center of the cone is about 10^{-3} cm^{-3}, which is relatively low among all cool core and non cool core clusters (e.g., Hudson et al. 2010). The corresponding cooling time is about 27 Gyr, which is much larger than the Hubble time, implying an expansion of the core after the collision with another subcluster.

An analogy of the cone-shaped subcluster in simulations is presented in fig. 9 of Zhang et al. (2019a) at $t = 0.03$ Gyr. As a bullet-like subcluster leaves the atmosphere of the main cluster, due to the decrease in pressure, the far end starts to expand while the two sides are still under ram pressure stripping. Thus, the bullet-like subcluster is elongated and deformed. A cone-shaped subcluster with a narrow aperture appears at a certain stage of the merging process. We note that in ZwCl 2341+0000, the projected brightest cluster galaxy position is outside but very close to the apex of the cone, indicating that the dark matter sub-halo is still leading the gaseous subcluster. As the merger goes on, the tip of the cone will be continuously expanding to form a slingshot cold front (e.g., Abell 168 Hallman & Markevitch 2004). Another similar analogy is the $R = 1 : 3$ and $b = 0$ kpc simulation set in ZuHone (2011)[5]. At $t = 1.6$ Gyr, the subcluster evolves to

[5] http://gcmc.hub.yt/fiducial/1to3_b0/index.html

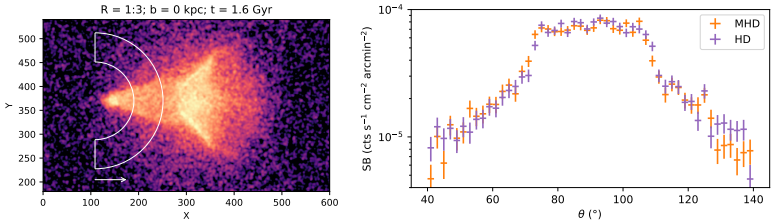

Figure 3.10: *Left:* Mock X-ray image of a cone-shaped subcluster in the $\beta = 100$ MHD simulation, whose merger configuration is the same as in ZuHone (2011) and Brzycki & ZuHone (2019). In this snapshot, two wing-like structures in addition to the cone are reproduced as well. *Right:* Azimuthal surface brightness profiles extracted from the mock observations of the MHD (orange) and HD (purple) simulations.

be a cone with an aperture of $40°$, which is similar with the observed conic structure. The fate of the conic subcluster in this simulation is the same as the one in Zhang et al. (2019a). After this epoch, the tip of the cone starts to expand in the low density outskirts. This simulation also produces a dense gas shell at the cone boundary, which is similar to the right part of the cone in ZwCl 2341+0000.

Effect of magnetic fields

During a merger, the magnetic field in the cluster can be amplified through multiple processes and could produce observable features such as plasma depletion layers (see Donnert et al. 2018, for a review). We investigate the effect of magnetic field in forming such conic subclusters by comparing a pure hydrodynamic (HD) simulation and a magnetohydrodynamic (MHD) simulation. Brzycki & ZuHone (2019) carried out MHD simulations with the same merger configurations as ZuHone (2011), where the initial magnetic field condition is $\beta = 200$ [6]. Similarly, we ran a new MHD simulation of the $1:3$ mass ratio with $\beta = 100$, where the effect of magnetic field should be more significant than the $\beta = 200$ simulation. We created mock images by putting both the HD and MHD simulations at $z = 0.27$ with ACIS configuration and 200 ks exposure time. The mock image of the MHD simulation is shown in the left panel of Fig. 3.10.

We extracted azimuthal surface brightness profiles for the simulated

[6] $\beta \equiv p_{\rm th}/p_{\rm B}$

conic subclusters. The profiles are plotted in the right panel of Fig. 3.10. The MHD simulation has a similar profile as the pure HD simulation, which means that the magnetic field with a $\beta = 100$ initial condition does not play a significant role in shaping the conic subcluster. Moreover, we do not find significant plasma depletion layers that push gas out and exhibit dark streaks in the image (as was found by, e.g., Werner et al. 2016 in a deep observation of the Virgo sloshing cold front). Therefore, the observed conic structure is consistent with both HD and MHD simulations and the effect of magnetic fields cannot yet be ascertained with the current data.

Gas bridge and ICM viscosity

In addition to the rare conic subcluster, the X-ray bridge structure is seldom discovered. The temperature of the bridge itself is 4.3 ± 1.1 keV and that of the combination of the bridge and the dark pocket below the bridge is 8.6 ± 2.4 keV. The similar temperature of the bridge and the cone indicates that the bridge could be the stripped gas trail from the cone. A similar structure has been found in M89, where two horns are attached to the front of the remnant core (Machacek et al. 2006). Kraft et al. (2017) argues that the horns could either be Kelvin-Helmholtz instability (KHI) eddies with a viewing angle of 30° or be due to the previous active galactic nucleus activities. Another similar case is galaxy group UGC12491 (Roediger et al. 2012), where the stripped tails split from the core. Although our cluster has an order of magnitude larger physical scale than the cases of M 89 and UGC 12491, because HD is scale-free, the KHI could still be responsible for the stripped gas trail in our system. If this gas trail is from a KHI eddy, based on its 400 kpc length, it should be stripped at the time when the stagnation point of the subcluster was about 400 kpc closer to the system centroid, and then evolves together with the subcluster.

Viscosity suppresses the development of KHI eddies that are smaller than a critical scale. In turn, with the existence of an eddy at a certain scale, we are able to constrain the upper limit of the viscosity μ, whose expression

is given by Ichinohe et al. (2021):

$$\begin{aligned}\mu \lesssim & \frac{\rho\lambda V}{a\sqrt{\Delta}} \\ \sim & 6300 \text{ g cm}^{-1}\text{s}^{-1} \left(\frac{n_{\rm out}}{3\times10^{-3}\text{ cm}^{-3}}\right)\left(\frac{\lambda}{100\text{ kpc}}\right)\left(\frac{V}{1700\text{ km s}^{-1}}\right) \\ & \times \left(\frac{a}{10}\right)^{-1}\left(\frac{2.5}{\sqrt{\Delta}}\right), \end{aligned} \tag{3.6}$$

where $n_{\rm out}$ is the ICM density outside the cold front, λ the scale of the eddy, V the shear velocity, a a coefficient to be 10 for a conservative estimation, $\Delta \equiv (\rho_1+\rho_2)^2/(\rho_1\rho_2)$ calculated using the gas densities inside and outside the cold front. In our case, $n_{\rm out} \sim 5\times10^{-4}$ cm^{-3}, which is about a factor of three lower than that in the cone. The scale of eddy is 400 kpc. We take the collision speed at pericenter 1900 km s^{-1} (Benson et al. 2017) to be an upper limit of the shear velocity. We obtain an upper limit of viscosity of ~ 5000 g cm^{-1} s^{-1}. The full isotropic Spitzer viscosity is

$$\mu_{\rm SP} = 21000 \times \left(\frac{kT}{14.7\text{ keV}}\right)^{5/2} \text{ g cm}^{-1}\text{ s}^{-1}, \tag{3.7}$$

assuming Coulomb logarithm $\ln\Lambda = 40$ (Spitzer 1956; Sarazin 1988). A ~ 9 keV ICM has $\mu_{\rm SP} \sim 6200$ g cm^{-1} s^{-1}, which means the viscosity is suppressed at least by a factor of 1.2 if the gas trail has a KHI origin. With only this long gas trail, we cannot place strict constraints on the viscosity suppression factor, which is at least three in other systems, for example, three for Abell 2319 (Ichinohe et al. 2021), five for Abell 2142 (Wang & Markevitch 2018), and 20 for Abell 3667 (Ichinohe et al. 2017).

Suppression of diffusion

We note that the western side of the cone has a sharp surface brightness jump, whose width has 1σ upper limit of $2.4°$ azimuth. Though this cluster has a relatively high redshift of 0.27, at which the projected linear scale corresponding to a $2.4°$ bin at the radius of $100''$ is 17 kpc, it is still worthwhile to inspect whether the diffusion is suppressed to form the observed sharp edge. Assuming the ICM is in thermal equilibrium, the mean free path of electrons is given by Sarazin (1988),

$$\lambda_e = 31\text{ kpc}\left(\frac{kT}{10\text{keV}}\right)^2\left(\frac{n_e}{10^{-3}\text{cm}^{-3}}\right)^{-1}. \tag{3.8}$$

The mean free path is about 4.1 kpc for a $kT = 4.5$ keV and $n_e = 1.5 \times 10^{-3}$ cm^{-3} ICM inside the cold front, and is about 13.1 kpc for a $kT = 6.5$ keV and $n_e = 1 \times 10^{-3}$ cm^{-3} ICM outside the cold front. Meanwhile, the mean free path of the particles moving from one side of the cold front to the other side is given by Vikhlinin et al. (2001),

$$\lambda_{\mathrm{A}\to\mathrm{B}} = \lambda_{\mathrm{A}} \frac{kT_{\mathrm{A}}}{kT_{\mathrm{B}}} \frac{G(1)}{G\left(\sqrt{kT_{\mathrm{A}}/kT_{\mathrm{B}}}\right)}, \tag{3.9}$$

where $G(x) = \left[\Phi(x) - x\Phi'(x)\right]/2x^2$ and $\Phi(x)$ is the error function, the subscripts A and B represent inside and outside of the cold front, and vice versa. The mean free path for particles moving from inside to the outside is $\lambda_{\mathrm{in}\to\mathrm{out}} = 9.2$ kpc. The unsuppressed Coulomb diffusion will smear the density discontinuity by several mean free paths, which is comparable with the 1σ upper limit of the projected jump width. Therefore, without future deeper high spatial resolution observations, we cannot draw a solid conclusion whether the diffusion is suppressed.

3.4.3 The origin of the NE wing

In some head-on mergers, gas plumes perpendicular to the merging axis are observed, for example Abell 168 (Hallman & Markevitch 2004), Abell 2146 (Russell et al. 2010, 2012). Russell et al. (2012) suggest that the structure in Abell 2146 is likely to be part of the remnant core of the primary subcluster, which was pushed forward and laterally by the collision. This scenario can also be applied to this merging system where we observe two wings behind the outbound NW subcluster.

However, the size of NE wing is considerable and is even larger than the NW conic subcluster. Thus, it may have a different origin. The optical analysis suggests that in addition to the $z = 0.2687$ northern subcluster that is associated with the cone in X-ray and the $z = 0.2684$ southern subcluster that is associated with the southern linear structure, a third subcluster at $z = 0.2743$ is spatially overlaid with the northern subcluster (Benson et al. 2017). The large NE wing may belong to the third subcluster and was displaced to the NE direction. To prove this scenario, we search for galaxies that around the NE wing tip in the redshift catalog of Benson et al. (2017). We find several galaxies there, but all of them are at $z \sim 0.270$. If the NE wing is associated with those galaxies, it is more likely to be from the either the $z = 0.2687$ northern subcluster or the $z = 0.2684$ southern subcluster.

Therefore, we prefer the scenario of a displaced gas clump due to the head-on collision. The mystery of the remarkable size of the NE wing needs to be further investigated by numerical simulations with specific merging parameters.

3.5 Conclusion

We analyzed the deep *Chandra* observations of merging galaxy cluster ZwCl 2341+0000. The cluster is elongated in the NW-SE direction. Meanwhile, we used GMRT and JVLA data to investigate the properties of the radio shocks. We summarize the main results as follows:

1. The SE linear surface brightness edge is a kink in the new observations. It is the disrupted core of the southern subcluster. The shock front that is possibly responsible for the southern radio relic is revealed by the radio spectral index maps and is located at the SE edge of the relic component S2, which is $\sim 160''$ (640 kpc) away from the SE surface brightness kink.

2. At radio wavelengths, the Mach numbers of the southern and northern shocks are 2.2 ± 0.1 and 2.4 ± 0.4, based on injection spectral indices and the assumption of DSA. In X-rays, assuming the pre-shock ICM temperature follows a universal profile of relaxed clusters, we obtain a 3σ lower limit of the southern shock Mach number of 1.6.

3. The NW subcluster has a cone shape with two linear ~ 400 kpc cold fronts on the two sides. We searched for analogies of the cone-shaped subcluster in numerical simulations and found that the cone is a certain stage of an outbound subcluster in the head-on merger, which happens between a bullet-like morphology and a slingshot phase. This stage is short-lived, and no other example has been discovered to date.

4. Behind the NW conic subcluster, there are two wing structures stretching out in the NE and western directions. The NE wing is broad and has a low temperature and entropy at the tip. The redshift of galaxies around the wingtip suggests that this structure is unlikely to be associated with the third subcluster discovered in the previous optical analysis. This may thus represent an unexpectedly large gas plume expanding perpendicular to the merger axis.

5. A 400 kpc cool (~ 4 keV) gas bridge connects the apex of the NW cone and the NE wing. The low temperature suggests that this is a stripped gas trail from the NW subcluster. Why it is split from the subcluster is unclear. It could have evolved from a KHI eddy.

6. There are two surface brightness bays located in the SW periphery. The southern bay and the ridge between the two bays have a > 10 keV temperature, while the northern bay has a 3.3 ± 0.7 keV temperature. There is no pressure equilibrium between the ridge and the northern bay. The physical origin of these features is still unclear.

In summary, ZwCl 2341+0000 is an exciting galaxy cluster merger that exhibits several unique morphology features. It is likely in a short-lived phase that is rarely observed and offers an example of the complex transition between a bullet-like morphology and the development of a slingshot tail.

Acknowledgments

We thank the anonymous referee for useful comments and suggestions that helped improve this paper. X.Z. acknowledges support from Chinese Scholarship Council (CSC). A.S. is supported by the Women In Science Excel (WISE) programme of the Netherlands Organisation for Scientific Research (NWO), and acknowledges the World Premier Research Center Initiative (WPI) and the Kavli IPMU for the continued hospitality. SRON Netherlands Institute for Space Research is supported financially by NWO. R.J.vW. acknowledges support from the ERC Starting Grant ClusterWeb 804208. C.S. and A.B. acknowledge support from ERC-Stg DRANOEL n. 714245. This research has made use of data obtained from the Chandra Data Archive and the Chandra Source Catalog, and software provided by the Chandra X-ray Center (CXC) in the application package CIAO. The National Radio Astronomy Observatory is a facility of the National Science Foundation operated under cooperative agreement by Associated Universities, Inc. We thank the staff of the GMRT who have made these observations possible. The GMRT is run by the National Centre for Radio Astrophysics of the Tata Institute of Fundamental Research. This work made use of data from the Galaxy Cluster Merger Catalog. This research made use of Astropy,[7] a community-developed core Python package for Astronomy (Astropy Collaboration et al. 2013, 2018)

[7] `http://www.astropy.org`

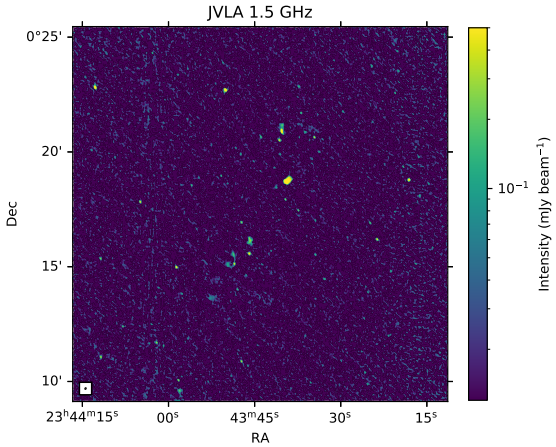

Figure 3.11: JVLA 1.5 GHz B-configuration radio map of ZwCl 2341+0000.

3.A JVLA B-configuration radio map

The JVLA L-band B-configuration image is plotted in Fig. 3.11, where most of the relics are not visible.

3.B Radio spectral index uncertainty map

The spectral index uncertainty map between 325 MHz and 1.5 GHz is plotted in Fig. 3.12. We also plot the spectral index map between 325 MHz and 3.0 GHz as well as its uncertainty map.

3.C Temperature uncertainty map

The uncertainties of the pseudo pressure and entropy are dominated by the uncertainty of the temperature. The temperature uncertainty map (Fig. 3.13) shows that most regions of interests have an uncertainty less than 20%. Only the region HT3 has an uncertainty about 35%.

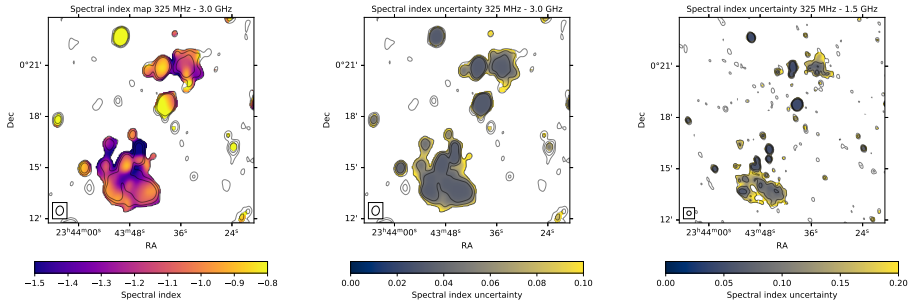

Figure 3.12: *Left and Middle:* Spectral index map and the uncertainty between 325 MHz and 3.0 GHz. *Right:* Spectral index uncertainty map between 325 MHz and 1.5 GHz.

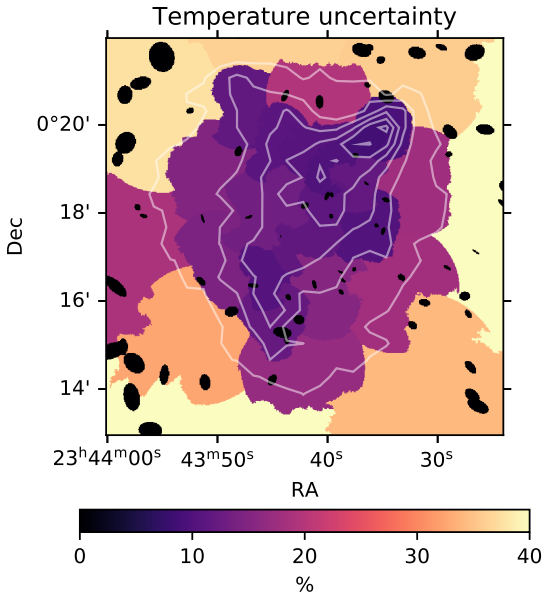

Figure 3.13: Temperature uncertainty map of ZwCl 2341+0000 in units of percent, overlaid with the X-ray surface brightness contours.

3.D Projected surface brightness profile for a cone-shaped cold front

We assume the core remnant is in a right circular cone shape. For a given point in the space, the electron density can be expressed as a function of the distance to the apex ρ and the angle with respect to the cone axis ϕ (i.e., $n_e = n_e(\rho, \phi)$). Similar to the broken power law model applied on a spheroid (Owers et al. 2009), we define a broken power law density profile across a cone-shaped cold front,

$$n_e(\rho,\phi) = \begin{cases} n_0 \left(\frac{\phi}{\phi_b}\right)^{-\alpha_1} \left(\frac{\rho}{\rho_0}\right)^{-\alpha_\rho}, & \phi \leqslant \phi_b \\ \frac{n_0}{C} \left(\frac{\phi}{\phi_b}\right)^{-\alpha_2} \left(\frac{\rho}{\rho_0}\right)^{-\alpha_\rho}, & \phi_b < \phi \leqslant \phi_{\max} \end{cases}, \tag{3.10}$$

where n_0 is the electron density normalization, ϕ_b the angle of the discontinuity, C the density jump, α_1 and α_2 the power law index inside and outside the discontinuity, the term $(\rho/\rho_0)^{-\alpha_\rho}$ is the density variation along the axis, which is approximately negligible since the radial surface brightness is averaged. We assume the gas density is zero where $\phi > \phi_{\max}$.

The cone is projected to the plane of the sky. Assuming the axis is parallel to the sky plane, the integrated surface brightness at any point of the sky plane (r, θ) is

$$S(r,\theta) \propto \int_{-l_{\max}}^{l_{\max}} n_e^2 \mathrm{d}l,\ \theta \leqslant \phi_{\max}, \tag{3.11}$$

where $l_{\max} = r \times \left[1 - (\cos\phi_{\max}/\cos\theta)^2\right]^{1/2}$ is the boundary of the integration. Therefore, the radially averaged surface brightness is

$$S_\theta(\theta) = \frac{2}{r_{\max}^2 - r_{\min}^2} \int_{r_{\min}}^{r_{\max}} S(r,\theta) r \mathrm{d}r, \tag{3.12}$$

where $r_{\min}$ and $r_{\max}$ are the inner and outer radii of the extraction sector.

4 ClG 0217+70: A massive merging galaxy cluster with a large radio halo and relics

X. Zhang, A. Simionescu, J.S. Kaastra, H. Akamatsu, D.N. Hoang, C. Stuardi, R.J. van Weeren, L. Rudnick, R.P. Kraft and S. Brown

(Astronomy & Astrophysics, Volume 642, L3)

Abstract

We present an analysis of archival *Chandra* data of the merging galaxy cluster ClG 0217+70. The Fe XXV Heα X-ray emission line is clearly visible in the 25 ks observation, allowing a precise determination of the redshift of the cluster as $z = 0.180 \pm 0.006$. We measure $kT_{500} = 8.3 \pm 0.4$ keV and estimate $M_{500} = (1.06 \pm 0.11) \times 10^{15}\ M_{\odot}$ based on existing scaling relations. Correcting both the radio and X-ray luminosities with the revised redshift reported here, which is much larger than inferred previously based on sparse optical data, this object is no longer an X-ray underluminous outlier in the $L_{\rm X} - P_{\rm radio}$ scaling relation. The new redshift also means that, in terms of physical scale, ClG 0217+70 hosts one of the largest radio haloes and one of the largest radio relics known so far. Most of the relic candidates lie in projection beyond r_{200}. The X-ray morphological parameters suggest that the intracluster medium is still dynamically disturbed. Two X-ray surface brightness discontinuities are confirmed in the northern and southern parts of the cluster, with density jumps of 1.40 ± 0.16 and 3.0 ± 0.6, respectively. We also find a 700×200 kpc X-ray faint channel in the western part of the cluster, which may correspond to compressed heated gas or increased non-thermal pressure due to turbulence or magnetic fields.

4.1 Introduction

Galaxy cluster mergers are the most extreme events in the universe and can release energies up to 10^{64} erg. The shocks and magnetohydrodynamic (MHD) turbulence generated during these mergers heat the intracluster medium (ICM) and can also (re)accelerate particles into the relativistic regime (see Brunetti & Jones 2014 for a theoretical review). Synchrotron radiation emitted by these relativistic particles as they gyrate around intergalactic magnetic field lines leads to observed giant radio halos and radio relics (see van Weeren et al. 2019 for a review). Merging galaxy clusters therefore provide unique laboratories to study particle acceleration in a high thermal-to-magnetic pressure ratio plasma. Among the large merging galaxy cluster sample, clusters that host double relics are a rare subclass. They usually have a simple merging geometry with the merger axis close to the plane of the sky and therefore suffer less from projection uncertainties.

ClG 0217+70, also known as 8C 0212+703 (Hales et al. 1995) or 1RXS J021649.0+703552, is a radio-selected merging cluster (Rengelink et al. 1997; Rudnick et al. 2006), which hosts several peripheral radio relic candidates located on opposite sides of a central radio halo (Brown et al. 2011). Among the relic candidates, sources C, E, F and G (see Fig. 4.1 for definition) are not associated to any optical galaxy and a recent study shows that their spectral indices are steeper towards the cluster center (Hoang et al. in prep.), indicating a shock acceleration feature. This cluster appears as an X-ray underluminous outlier in the $L_{\rm X} - P_{\rm radio}$ scaling relation (e.g. Brunetti et al. 2009; Cassano et al. 2013). One possible explanation for this is the misestimation of the redshift which, lacking deep optical data, was believed to be $z = 0.0655$ (Brown et al. 2011). An accurate redshift is essential to scale the physical properties of the cluster as well as those of the diffuse radio sources, e.g., size and luminosity.

Here we present an analysis of archival *Chandra* data, which allows a precise determination of the cluster redshift via the ICM Fe-K line. The high spatial resolution of *Chandra* also enables us to search for surface brightness discontinuities related to the merger. We adopt a ΛCDM cosmology, where $H_0 = 70$ km s^{-1} Mpc^{-1}, $\Omega_{\rm m} = 0.3$ and $\Omega_\Lambda = 0.7$.

4.2 Observations and data reduction

We have analyzed the 24.75 ks *Chandra* archival data (ObsID: 16293). The Chandra Interactive Analysis of Observations (CIAO)[1] v4.12 with CALDB 4.9.0 is used for data reduction. The level 2 event file is generated by the task `chandra_repro` with the VFAINT mode background event filtering. We extract the 100 s binned 9 – 12 keV light curve for the whole field and do not find flares. Therefore, we use the entire exposure period for data analysis.

4.3 Data analysis and results

For the imaging analysis, we use the task `fluximage` to extract the 1 – 3 keV count map and the corresponding exposure map with vignetting correction. The non X-ray background (NXB) map is generated from the stowed background file, which is reprojected to the observation frame by using `reproject_events` and is scaled by the 9 – 12 keV count rate. The exposure map is applied to the count map after the NXB subtraction to produce the flux map (see Fig. 4.1). For the spectral analysis, we use the task `blanksky` to create the tailored blank sky background. Source and background spectra are created using the script `specextract`, where the weighted redistribution matrix files and ancillary response files are created by `mkwarf` and `mkacisrmf`, respectively. The background spectra are scaled by the 9 – 12 keV count rate. We use SPEX v3.06 (Kaastra et al. 1996; Kaastra et al. 2018b) to fit the spectra. The reference protosolar element abundance table is from Lodders et al. (2009). The 0.5–7.0 keV energy range of all spectra are used and optimally binned (Kaastra & Bleeker 2016). The C-statistics (Cash 1979) is adopted as the likelihood function in the fit. We use spectral models $red \times hot \times cie$ to fit the spectra of the ICM, where red represents the cosmological redshift, cie is the emission from hot cluster gas in collisional ionization equilibrium, and we fix the temperature of the hot model to 5×10^{-4} keV to mimic the absorption from neutral gas in our Galaxy. In the cie model, we couple the abundances of all metals (Li to Zn) with Fe.

[1] `https://cxc.harvard.edu/ciao/`

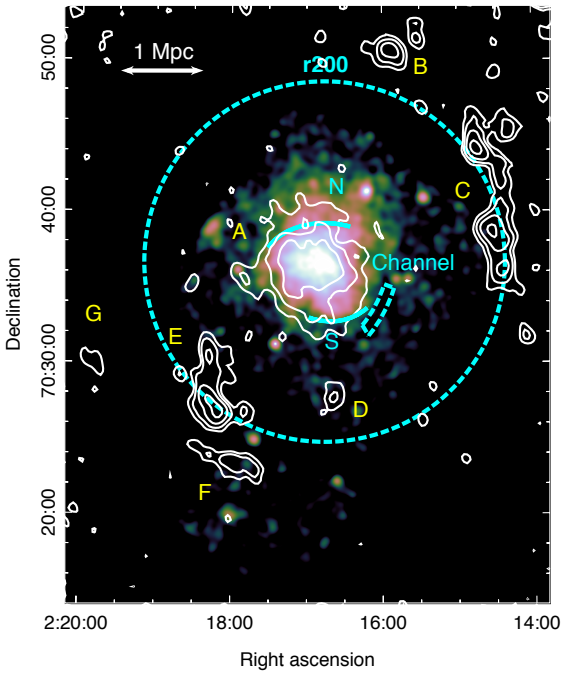

Figure 4.1: Multi-wavelength view of the merging cluster CIG 0217+70. The color image is the NXB subtracted, vignetting corrected, and adaptively smoothed 1–3 keV *Chandra* flux map. The white contours are compact source subtracted VLA L-band D configuration radio intensities at $3\sigma_{\rm rms} \times [1, 2, 4, 8]$ levels, where $\sigma_{\rm rms} = 70$ μJy. Individual diffuse radio sources are labelled following the terms of Brown et al. (2011), where source A is the giant radio halo and B–G are relic candidates. The dashed circle represents r_{200}. The northern and southern X-ray surface brightness discontinuities as well as the western "channel" are marked using cyan arcs and an annulus sector.

Table 4.1: Best-fit parameters and auxiliary information for the spectra extracted from different annuli.

Region	z	$n_{\rm H}$ (10^{21} cm^{-2})	kT (keV)	Z ($Z_\odot$)	S/B	C-stat / d.o.f.
0″–100″	0.190 ± 0.010	8.2 ± 0.5	$10.0^{+1.6}_{-1.1}$	0.52 ± 0.15	11.6	136.9/126
100″–200″	0.184 ± 0.011	8.1 ± 0.4	7.8 ± 0.8	0.35 ± 0.11	4.5	128.5/126
200″–300″	0.174 ± 0.009	6.8 ± 0.7	6.8 ± 1.1	0.60 ± 0.21	1.0	122.9/124
0″–500″	0.180 ± 0.006	7.3 ± 0.3	8.3 ± 0.7	0.43 ± 0.09	1.7	145.1/142

4.3.1 Spectral properties and X-ray redshift

This object is at a low Galactic latitude and has high Galactic absorption. The tool `nhtot`[2], which includes the absorption from both atomic and molecular hydrogen (Willingale et al. 2013), suggests $n_{\rm H,total} = 4.77 \times 10^{21}$ cm^{-2}. However, fixing the $n_{\rm H}$ to this value leads to significant residuals in the soft band. The best-fit $n_{\rm H}$ from three annuli centered at the X-ray peak and having different source-to-background ratios (S/B) are consistent with each other and all imply a Galactic $n_{\rm H}$ that is higher than the `nhtot` database value (see Table 4.1). This suggests the low-energy residuals are not due to a mis-modeling of the Galactic Halo foreground.

Allowing $n_{\rm H}$ as a free parameter, the temperature in the three central annuli considered for this analysis is $kT \sim 8$ keV. The $kT - r_{200}$ scaling relation of Henry et al. (2009) then implies $r_{200} = 2.3$ Mpc. We also notice that the best fit redshift for all three annuli is $z \sim 0.18$, which is much higher then the previous estimation $z = 0.0655$ (Brown et al. 2011).

To confirm these findings we further extract a spectrum from the cluster's central r_{500} region, which we estimate as $r_{500} \approx 0.65 r_{200} = 1.47$ Mpc (Reiprich et al. 2013). For our assumed cosmology, this corresponds to $\sim 500''$ at $z \sim 0.18$. The best-fit redshift within this aperture is indeed $z = 0.180 \pm 0.006$, and the Fe emission lines are clearly visible in the X-ray spectrum (see Fig. 4.2). Other parameters are listed in the 4th row of Table 4.1. Yu et al. (2011) demonstrates that for X-ray CCD spectra, in the condition of $\Delta C_{\rm stat} \equiv C_{{\rm stat},Z=0} - C_{\rm stat,best-fit} > 9$, the X-ray redshifts agree with the optical spectroscopic redshifts well, and the value of our data $\Delta C_{\rm stat} = 20$ corresponds to an accuracy of $\sigma_z = 0.016$. We note that the WHL galaxy cluster catalog (Wen et al. 2012), compiled based on Sloan Digital Sky Survey (SDSS) -III photometric redshifts, does contain a source WHL J021648.6+703646 which overlaps spatially with ClG 0217+70. The brightest cluster galaxy (BCG) of this source is located $20''$ from the X-ray peak and has $z = 0.24 \pm 0.05$. Therefore, although the quality of the SDSS photometric redshift is poor due to the high Galactic extinction, it is consistent with the presence of a cluster at $z = 0.18$.

With the updated redshift, the largest linear size (LLS) of the radio halo detected by the Very Large Array (VLA) (Brown et al. 2011) reaches 1.6 Mpc, making this cluster the 6th largest known radio halo (see Feretti et al. 2012 for comparison). The LLS of the western relic candidate (source

[2] `https://www.swift.ac.uk/analysis/nhtot/index.php`

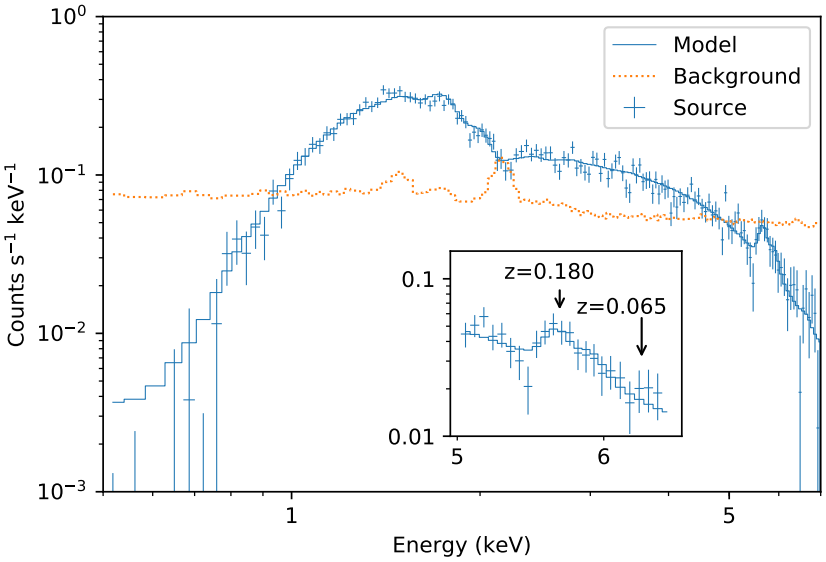

Figure 4.2: Spectrum inside r_{500}. The dotted line is the blank sky background that is subtracted. The box is a zoomed-in view of the bump that consists of Fe XXV Heα and Fe XXVI Lyα lines. The positions of the Fe XXV Heα line at different redshifts are marked.

C in Fig. 4.1) reaches 2.3 Mpc, becoming the second largest among the radio relics detected to date (see de Gasperin et al. 2014 for comparison). Recent Low Frequency Array (LOFAR) data shows that this relic candidate extends even further to a size of 2.9 Mpc at 150 MHz (Hoang et al. in prep.). Additionally, if we assume the X-ray peak as the cluster center, the projected distance $D_{\mathrm{projected,rc}}$ of the western relic candidate is 2.2 Mpc, which is the second largest among the currently known sample. The easternmost candidate (source G in Fig. 4.1), whose distance reaches 2.9 Mpc, becomes the record-holder for the farthest radio relic known with respect to the center of any galaxy cluster, surpassing the south-eastern relic in PSZ1 G287.00+32.90 (Bonafede et al. 2014) with $D_{\mathrm{projected,rc}} = 2.8$ Mpc.

Importantly, all relic candidates have a $D_{\mathrm{projected}} > r_{500}$. Except source D, all candidates are located at $\gtrsim r_{200}$ (see Fig. 4.1). This cluster may thus provide a good example of runaway merging shocks (Zhang et al. 2019b), which are long-lived in the habitable zone in the cluster outskirts.

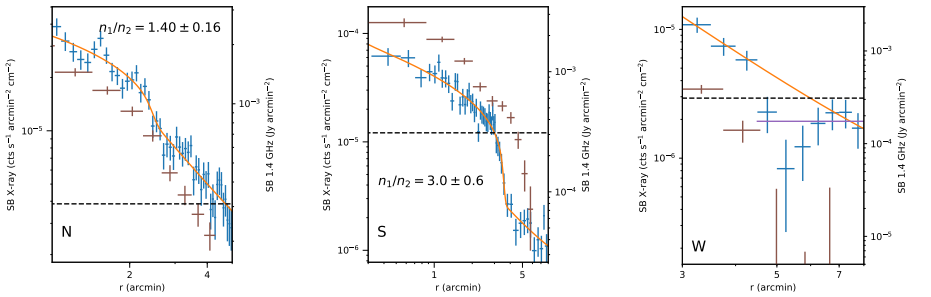

Figure 4.3: X-ray surface brightness profiles (blue) as well as the best-fit model (orange) in each extraction regions. The radio surface brightness profiles are plotted as brown points. The horizontal dashed line is the $3 \times \sigma_{\rm rms}$ level of the radio map. In the western channel region, In addition to the best-fit power law model (orange), the constant model after the jump is plotted as the purple line.

4.3.2 X-ray morphology and surface brightness discontinuities

The X-ray flux map (Fig. 4.1) shows a single-peaked and irregular morphology inside r_{2500}. The X-ray core is elongated in the NW-SE orientation, and its location matches the peak of the radio halo. Unlike some other typical binary on-axis merging systems with double relics e.g., Abell 3376 (Bagchi et al. 2006), ZwCl 0008.8+5215 (Di Gennaro et al. 2019) and El Gordo (Menanteau et al. 2012), the morphology of this cluster does not show an outbound subcluster, perhaps indicating a later merger phase.

Previous work shows that the presence of a radio halo is related to the dynamical state of a cluster, which can be quantified by X-ray morphological parameters (Cassano et al. 2010). Following the methods in Cassano et al. (2010), we calculate the centroid shift w (Mohr et al. 1993; Poole et al. 2006) and the concentration parameter c (Santos et al. 2008). The result $(w, c) = (0.046, 0.11)$ is located in the quadrant where most of the clusters host a radio halo (see Fig. 1 in Cassano et al. 2010).

In addition, we find two X-ray surface brightness discontinuities about 460 kpc and 680 kpc toward the north and south of the core (see Fig. 4.1). We extract and fit the surface brightness profiles assuming an underlying spherically projected double power-law density model (Owers et al. 2009). To account for a possible mismatch between the extraction regions and the actual curvature of the edge, we smooth the projected model profile with a $\sigma = 0.1'$ Gaussian kernel. The cosmic X-ray background is modeled as

a constant $S_{\rm bg} = 4 \times 10^{-7}$ count s^{-1} arcmin^{-2} cm^{-2}, obtained by fitting the azimuthally averaged radial surface brightness profile using a double β-model (Cavaliere & Fusco-Femiano 1976) plus a constant model.

The profiles and best-fit models are plotted in Fig. 4.3. The best-fit density jump of the southern and northern edges are $C = 3.0 \pm 0.6$ and $C = 1.40 \pm 0.16$, respectively. We also over-plot the VLA L-band D configuration (Brown et al. 2011) radio surface brightness profiles. In the northern region, the slope of the radio surface brightness profile changes from 0.85 ± 0.05 to 2.4 ± 0.3 at the radius of 400 kpc. The southern region shows a marked X-ray jump that is, however, misaligned with a steep drop-off in the radio brightness profile, which occurs $\sim 2' = 370$ kpc further out. This sharp drop is unlikely due to the flux loss in interferometric observations. The largest angular scale of D configuration is $\sim 16'$. Only emission that is smooth on scales $> 10'$ is subject to significant flux loss (on the order of 10% or greater, Brown et al. 2011), while the features discussed here are on much smaller scales.

The thermodynamic properties of these edges are still unclear due to the short exposure time; however, for the southern edge to be a cold front, the temperature on the faint side would have to be very high, 16 keV. If any of the two edges is confirmed as a shock front, this cluster could be another rare case where the X-ray shock is associated with the edge of a radio halo, e.g. Abell 520 (Hoang et al. 2019), Bullet Cluster (Shimwell et al. 2014), Coma Cluster (Brown & Rudnick 2011; Planck Collaboration et al. 2013) and Toothbrush Cluster (van Weeren et al. 2016a).

Apart from the two surface brightness discontinuities, we also find a large scale X-ray "channel" in the south-western part of the cluster (the dashed region in Fig. 4.1). The length is at least 700 kpc and the width can be over 200 kpc. We use a single power law density model to fit this profile, where we ignore the data points from 4.5 to 6 arcmin. The lowest point is below the power law model by 5.3σ. Alternatively, the large difference between $4'$ and $5'$ can be interpreted as a surface brightness edge, with the channel being right outside the edge. In this case, if we use a constant model to fit the data points from 4.5 to 8 arcmin excepting the dip, the lowest point is 2.0σ below the model. The density in the channel region is $< 50\%$ of the power law model and is 65% of the constant model. The radio surface brightness also decreases sharply before the channel. Inside the channel, the upper limit of the radio emission is 7×10^{-5} Jy arcmin^{-2}.

4.4 Discussion

4.4.1 Radio halo scaling relations

This cluster was believed to be an X-ray underluminous or a radio overluminous source in the radio halo $L_{\rm X} - P_{1.4\ \rm GHz}$ diagram (Brown et al. 2011). Meanwhile, using the $M_{500} - L_X$ scaling relation (Pratt et al. 2009), Bonafede et al. (2017) found this object to be an outlier in the $M_{500} - P_{1.4\ \rm GHz}$ relation. The new redshift reported here leads to an updated 1.4 GHz radio power of $(5.33 \pm 0.08) \times 10^{24}$ W Hz^{-1} and an X-ray luminosity inside r_{500} of $L_{0.1-2.4\rm keV} = (7.19 \pm 0.12) \times 10^{44}$ erg s^{-1}, bringing this cluster into agreement with the expected radio halo $L_{\rm X} - P_{1.4\ \rm GHz}$ relationship. Furthermore, using the M_{500}–kT scaling relation of Arnaud et al. (2007) we obtain $M_{500} = (1.06 \pm 0.11) \times 10^{15}\ M_{\odot}$. This cluster then also follows the $M_{500} - P_{1.4\ \rm GHz}$ scaling relation (Cassano et al. 2013) (see Fig. 4.4). The Sunyaev-Zeldovich (SZ) effect of such a massive cluster should be detected by *Planck*. However, due to its low galactic latitude, it is not in the second *Planck* SZ catalog (Planck Collaboration et al. 2016).

The remaining two outliers on the $L_{\rm X} - P_{\rm radio}$ scaling relation are Abell 1213 and Abell 523. In Abell 1213, the diffuse emission is on scales of only 200 kpc and is dominated by bright filamentary structures (Giovannini et al. 2009). Abell 523 has a unique linear structure unlike other radio halos (Giovannini et al. 2011). With the results presented here, there may thus be no known regular radio halo that doesn't follow these scaling relations.

4.4.2 The western X-ray "channel"

We observe an X-ray deficit in the western part of the cluster, where the gas density is about half of that in the inner region. This channel-like structure can be a compressed heated region between the main cluster and an in-falling group, as has been seen in e.g. Abell 85 (Ichinohe et al. 2015), or between colliding subclusters (e.g., Abell 521 Bourdin et al. 2013). Although no significant X-ray substructure is seen outside the channel in ClG 0217+70, an infalling group that has been stripped of its gas content early during the merger could still produce the observed feature.

Alternatively, non-thermal pressure, either in the form of turbulent motions or enhanced magnetic fields that push out the thermal gas, may play a role. This explanation has been proposed for similar substructures observed along a cold front in the Virgo Cluster (Werner et al. 2016), and in

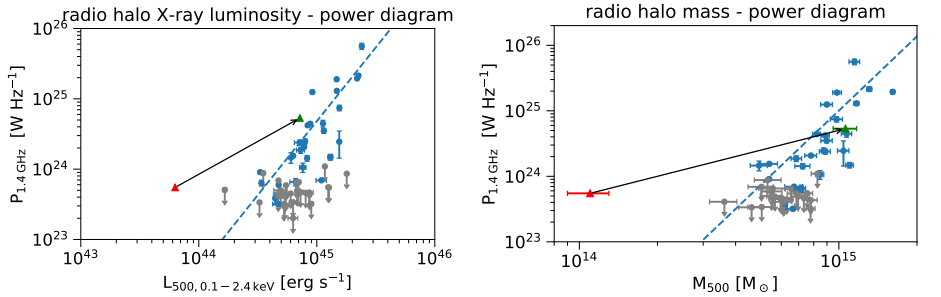

Figure 4.4: $L_{\rm X} - P_{1.4\ \rm GHz}$ (left) and $M_{500} - P_{1.4\ \rm GHz}$ (right) diagrams of radio halos. Figures are modified based on the version in van Weeren et al. (2019), where the data samples are from Cassano et al. (2013); Kale et al. (2015); Cuciti et al. (2018). Blue points are clusters with radio halos and gray upper limits are clusters without radio halos. Blue dashed lines are the best-fit scaling relations from (Cassano et al. 2013). The red triangle is CIG 0217+70 using the previous redshift, the green triangle is the corrected value. The error bars of $L_{\rm X}$ and $P_{1.4\ \rm GHz}$ of CIG 0217+70 are smaller than the plot symbols.

Abell 520 (Wang et al. 2016a) and Abell 2142 (Wang & Markevitch 2018). Assuming the ICM is isothermal across the channel, to compensate the at least 35% pressure deficit, the non-thermal pressure should be equal to the thermal pressure. If the magnetic field enhancement is alone responsible for this non-thermal pressure, $B \sim 15\ \mu$G is required and the corresponding thermal-to-magnetic pressure ratio reaches $\beta \sim 2$. Such considerable local magnetic field enhancement is indeed seen in MHD simulations of sloshing cold fronts (ZuHone et al. 2011). One might expect that this high magnetic field would lead to a detectable level of radio emission in the channel, which is disfavored by the current VLA observation. However, since the exact underlying relativistic electron distribution is unknown, this scenario cannot be ruled out. If on the other hand the non-thermal pressure is entirely due to turbulent motions, the turbulent Mach number $\mathcal{M}_{\rm turb} = \sqrt{2/\gamma \times (\epsilon_{\rm turb}/\epsilon_{\rm therm})}$ (Werner et al. 2009) should be close to one, which is also very unlikely. In reality of course a combination of all the above factors is also possible.

4.4.3 Possible merging scenario

The western relic candidate C as well as the eastern relic candidates E, F and G are likely to be accelerated by two spherical shocks that are centrally symmetric and moving towards NW and SE, respectively. The two spherical shocks are presumably created by the first core passage and then propagate to the outskirts of this system. The two discovered surface brightness jumps are in the N-S orientation, which is almost perpendicular to the previous merging axis. Additionally, the projected distance between the cluster center and the two surface brightness discontinuities is $\lesssim 700$ kpc, which is much less than the $D_{\rm projected}$ of the outermost relics. Both the orientation and the short $D_{\rm projected}$ of the surface brightness discontinuities suggest that they are not related to the first core passage event. A possible explanation of this merger might be that it starts as an off-axis merger, after which the two (or more) dark matter halos, as well as the ionized gas, move back to the centroid of the system again. The collision of the ICM produces new shocks or cold fronts, but the orientation is different from the first passage.

4.5 Conclusion

We analyzed the 25 ks archival *Chandra* data of the merging galaxy cluster ClG 0217+70. The *Chandra* X-ray data allow us to measure the redshift of the system, which is $z = 0.180 \pm 0.006$. With the updated redshift, the projected physical sizes of the radio halo and radio relic candidates make them some of the largest sources discovered so far. Most of the radio relic candidates have projected distances $\gtrsim r_{200}$. We measure the averaged temperature inside r_{500} as $kT_{500} = 8.3 \pm 0.6$ keV. Using the $kT - M_{500}$ scaling relation, we estimate $M_{500} = (1.06 \pm 0.11) \times 10^{15}\ M_{\odot}$. The centroid shift w and the concentration parameter c show that the ICM is still dynamically disturbed. Two surface brightness discontinuities are detected with density jumps of 1.40 ± 0.16 in the north and 3.0 ± 0.6 in the south. The southern edge has one of the largest density jumps ever detected in galaxy clusters. We also find a 700 kpc long and > 200 kpc wide surface brightness channel in the western part of the cluster, which may be indicative of significant compressed heated gas or non-thermal pressure from magnetic fields or turbulence.

In this work, X-ray spectroscopy shows its power of measuring the ICM

redshift directly. Its strength will be remarkably exploited in future missions with X-ray microcalorimeters e.g., *XRISM* and *Athena*.

Acknowledgements

X.Z. acknowledges support from China Scholarship Council. SRON is supported financially by NWO, The Netherlands Organization for Scientific Research. D.N.H. acknowledges support from the ERC-Stg17 714245 DRANOEL. C.S. acknowledges support from the ERC-StG DRANOEL, n. 714245. R.J.vW. acknowledges support from the VIDI research programme with project number 639.042.729, which is financed by the Netherlands Organisation for Scientific Research (NWO). Partial support for L.R. comes from US National Science Foundation grant AST17-14205 to the University of Minnesota. This research has made use of data obtained from the Chandra Data Archive and the Chandra Source Catalog, and software provided by the Chandra X-ray Center (CXC) in the application package CIAO.

5 The *Planck* clusters in the LOFAR sky: Dynamic states and density fluctuations of the intracluster medium

X. Zhang, A. Simionescu, F. Gastaldello, D. Eckert, L. Camillini, R. Natale, H. Akamatsu, A. Botteon, R. Cassano, V. Cuciti, L. Bruno, T.W. Shimwell and J.S. Kaastra

(To be submitted)

Abstract

Context: The recent second data release of the LOFAR Two-metre Sky Survey (LoTSS-DR2) contains detections of 83 radio halos in *Planck* Sunyaev-Zeldovich (SZ) selected galaxy clusters, providing an excellent opportunity to statistically study the properties of radio halos.

Aims: We aim to investigate the relation between cluster dynamic state and radio halo power. Meanwhile, we attempt to search for connections between thermal and non-thermal characteristics of radio halos in LoTSS-DR2.

Methods: We analyzed *XMM-Newton* and *Chandra* archival X-ray data of all *Planck* SZ clusters in the footprint of LoTSS-DR2. We computed concentration parameters and centroid shifts that indicate the dynamic states of the clusters. Furthermore, we performed power spectral analysis of the X-ray surface brightness fluctuations to investigate large scale density perturbations and estimate the turbulent velocity dispersion.

Results: The concentration parameters measured by the two telescopes are in good agreement, while the centroid shift has a larger scatter. The telescope point spread function and limited count number can both contribute to the discrepancy of morphological parameters. Meanwhile, uncertainties in X-ray background evaluation also worsen the accuracy of the concentration parameter. The cluster relaxation state is marginally anti-correlated with the amplitude of surface brightness

and density fluctuations on large scales, while we do not find a correlation between the amplitude of density fluctuations and radio halo power or emissivity at 150 MHz. Nevertheless, the injected power for particle acceleration calculated from turbulent dissipation is correlated with the radio halo power, where the best-fit unity slope implies that the injected power from turbulence is proportional to the radiative loss that is observed at 150 MHz.

5.1 Introduction

Radio halos are extended radio sources widely observed at the centers of galaxy clusters. They are unpolarized, with size of ∼Mpc and having steep spectra with spectral index[1] smaller than -1 (see the review of van Weeren et al. 2019). The synchrotron nature of radio halos indicates relativistic cosmic rays (CRs) and magnetic fields permeating the intracluster medium (ICM). Among all proposed origins of CRs for radio halos, ICM turbulent acceleration is the most plausible in-situ mechanism (see the review of Brunetti & Jones 2014). Radio halos have been found to be associated with a number of cluster X-ray properties. Their radio power $\mathcal{P}_\nu$ is correlated with cluster X-ray luminosities $L_{\rm X}$ (Giovannini et al. 1999; Kempner & Sarazin 2001; Cassano et al. 2013; Kale et al. 2015). The presence of radio halos is statistically higher in dynamically disturbed clusters (Cassano et al. 2010). Moreover, the dynamic state of clusters can partially explain the scatter in the $\mathcal{P}_\nu$–$L_{\rm X}$ diagram (Yuan et al. 2015).

To better understand the role that turbulence plays in accelerating CRs in galaxy clusters, one approach is to map turbulent velocity dispersions in the ICM and search for their correlations with radio properties. The direct way of mapping ICM turbulent velocity fields in galaxy clusters uses X-ray emission line broadening (Zhuravleva et al. 2012), which requires high spectral resolution and is beyond the capability of current X-ray imaging spectrometers. The alternative way is using power spectra to measure density fluctuations as a proxy of the turbulent velocity dispersion (e.g. Churazov et al. 2012; Gaspari et al. 2014; Zhuravleva et al. 2014a). The first attempt of connecting turbulent velocity dispersion and radio halo properties was made by Eckert et al. (2017, hereafter E17), who used the power spectral method to measure the velocity dispersion σ_v for 51 galaxy clusters and studied the turbulent Mach number distribution, concluding that $\mathcal{P}_\nu$ is strongly correlated with σ_v.

[1] $S_\nu \propto \nu^\alpha$

The ongoing Low Frequency Array (LOFAR) Two-meter Sky Survey (LoTSS) (Shimwell et al. 2017) is powerful for systematic detection of radio halos in the northern hemisphere. In the footprint of the second LoTSS Data Release (LoTSS-DR2) (Shimwell et al. 2022), which covers 27% of the northern sky, we found 83 *Planck*-Sunyaev-Zeldovich DR2 (PSZ2) clusters (Planck Collaboration et al. 2016) hosting radio halos (Botteon et al. 2022, hereafter Paper I). The LoTSS-DR2-PSZ2 sample provides an excellent opportunity to systematically study the properties of radio halos in a mass-selected cluster sample. This is the sixth paper of the series. In this work, we focus on the X-ray properties and their connections to the radio halo properties of the PSZ2 clusters in the LoTSS-DR2 footprint. The data analysis includes two major parts. In the first part, we will compute two morphological parameters that indicate cluster dynamic states and discuss the discrepancy of measurements from different X-ray telescopes. The morphological parameters will be used in Cassano et al. (in prep.) for studying the radio halo occurrences and Cuciti et al.(in prep.) for studying the radio halo scaling relations. In the second part, we will compute large scale surface brightness (SB) and ICM density fluctuations. Using the density fluctuations, we estimate the turbulent velocity dispersion and explore its connection with radio halo power.

In this paper, we adopt a Lambda cold dark matter cosmology model with cosmological parameters $\Omega_{\rm M} = 0.3$, $\Omega_{\Lambda} = 0.7$ and $h_0 = 0.7$.

5.2 X-ray sample

The LoTSS-DR2 footprint covers 309 PSZ2 clusters. We use archival *XMM-Newton* European Photon Imaging Camera (EPIC) and *Chandra* Advanced CCD Imaging Spectrometer (ACIS) data for X-ray analysis. There are 115 and 110 PSZ2 clusters with *Chandra* and *XMM-Newton* observations, respectively. The data availability of individual PSZ2 clusters are listed in table 1 of Paper I, while image products are available on the project website[2]. The locations of clusters with available data are plotted in Fig. 5.1 and the sample sizes for different analysis are summarized in Table 5.1.

[2] `https://lofar-surveys.org/planck_dr2.html`

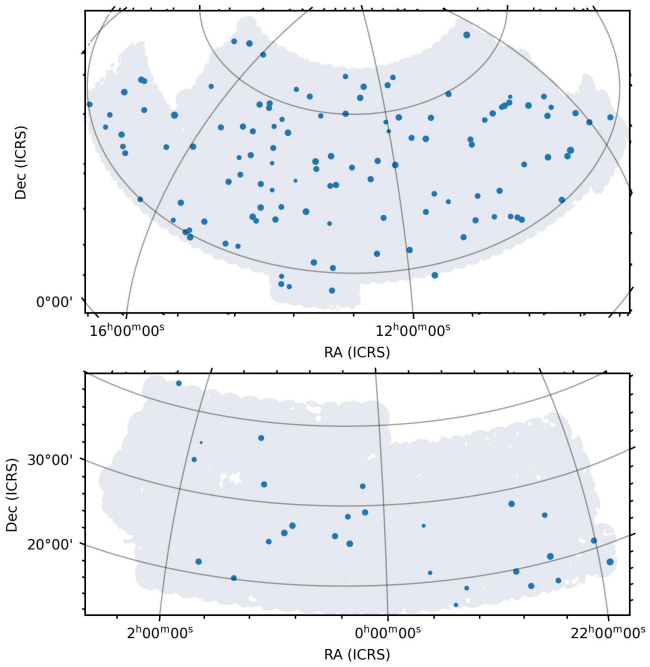

Figure 5.1: Footprint of the LoTSS-DR2 overlaid with locations of the PSZ2 clusters with available X-ray data. The marker size indicates the cluster mass.

Table 5.1: Summary of sample size in different steps.

Step	*Chandra*	*XMM-Newton*	Both	Total
A	115	110	72	153
B	105	98	63	140
C	107	109	66	150
D	–	64	–	64
E	–	36	–	36

[A] has archival data;
[B] has morphological parameter measurements;
[C] counting subclusters as individual clusters;
[D] meets criteria for power spectral analysis;
[E] has power spectra covering $k = (0.4 \times r_{500})^{-1}$.

5.2.1 Sample for morphological analysis

The summary of the X-ray sample used for morphology analysis is described in sect. 3.4 of Paper I. In short, we applied several criteria including field of view coverage, observation mode and image data quality to select the subsample for analysis. There are 140 clusters for which we derived morphological parameters. Among these clusters, 105 were observed by *Chandra*, and 98 by *XMM-Netwon*. Some PSZ2 objects are composed of multiple separate subclusters in X-rays. Taking all extended X-ray sources into account, there are 107 and 109 subclusters with *Chandra* and *XMM-Newton* measurements, respectively. The total number of subclusters with morphological parameters is 150.

5.2.2 Sample for power spectral analysis

Power spectral analysis for SB fluctuations requires more counts than calculating morphological parameters. Therefore, we used an additional criterion of $> 10^4$ net X-ray counts in the annulus between 100 kpc and r_{2500} to select a subsample for SB power spectral analysis. Sixty-nine out of the total 109 *XMM-Newton* (sub)clusters meet the criterion. Among them, we excluded several objects that are in a complex merger state, which cannot be well modeled by a typical (double) β-model. They are PSZ2 G093.94-38.82 ES and EN, which are in a late pre-merger phase; PSZ2 G124.20-36.48 N and S (Abell 115), which is an offset major merger after first core passage. In addition, we excluded PSZ2 G160.83+81.66 for analysis due to its high redshift of 0.88. We also checked *Chandra* archival data. Since *Chandra* has only 1/3 of the effective area of *XMM-Newton*, we searched for clusters with total ACIS-I exposure > 80 ks and found that all clusters that meet this criterion have available *XMM-Newton* observations. Because we only investigate surface brightness fluctuations on large scales, where the *XMM-Newton* point spread function (PSF) size is not an issue, we did not include the *Chandra* data for analysis. Therefore, we have a sample size of 64 for analysis.

The cluster masses listed in Paper I are retrieved from Planck Collaboration et al. (2016), which are estimated from the Compton-y parameter of each PSZ2 object and are close to the total mass for systems with multiple subclusters that are not resolved by *Planck*. For systems showing multiple components in the X-ray images, We searched for mass ratios in the literature to accurately obtain r_{500} values for individual subclusters. If weak

lensing analyses are available, we prefer to use the weak lensing mass. PSZ2 G058.29+18.55 (Lyra complex) has a mass ratio of 2:1 between the E and W subclusters (Clavico et al. 2019); PSZ2 G107.10+65.32 (Abell 1758) has weak lensing mass of $M_{500,\mathrm{N}} = 9.6 \times 10^{14}\ M_\odot$ and $M_{500,\mathrm{S}} = 3.7 \times 10^{14}\ M_\odot$ for the N and S subclsters, respectively (Monteiro-Oliveira et al. 2017); PSZ2G093.94-38.82 (Abell 2572) has no literature of mass estimation and the PSZ centroid is located at the W subcluster, thus we use 2/3 of the total PSZ2 mass $1.5 \times 10^{14}\ M_\odot$ as the mass of the W subcluster.

5.3 Data reduction and spectral analysis

We used the *XMM-Newton* Science Analysis Software (SAS) v18.0.0 and Chandra Interactive Analysis of Observations (CIAO) v4.12 (Fruscione et al. 2006) for data reduction and analysis. The detailed reduction, image processing and point source detection methods are described in sect. 3.4 of Paper I. In this section, we describe our method of spectral analysis and *XMM-Newton* EPIC-pn non X-ray background (NXB) scaling. The pn filter wheel closed (FWC) version we used is 2019v1.

5.3.1 XMM-Newton EPIC spectral analysis

We used event selection criteria `#XMMEA_EM&&PATTERN<=12` and `FLAG==0&&PATTERN<=4` to extracted MOS and pn spectra, respectively. Redistribution matrix files and auxiliary response files were generated by the tasks `rmfgen` and `arfgen`, respectively.

We used SPEX v3.06 (Kaastra et al. 1996; Kaastra et al. 2020a) for spectral analysis. Since most of our objects have a temperature $kT > 2$ keV based on the $M - kT$ scaling relations (Mantz et al. 2016), we used the atomic database SPEXACT v2.07 which includes less lines for fast calculation. We used the spectral model combination $cie1 \times red \times abs + cie2 \times abs + pow$, where the two cies are collisional ionization equilibrium models for the ICM and the foreground Galactic halo, red the redshift of the object, abs the Galactic absorption, pow the power law for the cosmic X-ray background (CXB). For $cie1$, the abundances of metal elements are coupled to Fe and we set the lower limit as 0.3 proto-solar (Lodders et al. 2009). The temperature for $cie2$ is fixed to 0.2 keV (Snowden et al. 1998), the normalization of abs is set to the value from the database `nhtot`[3] (Willingale

[3] `https://www.swift.ac.uk/analysis/nhtot/index.php`

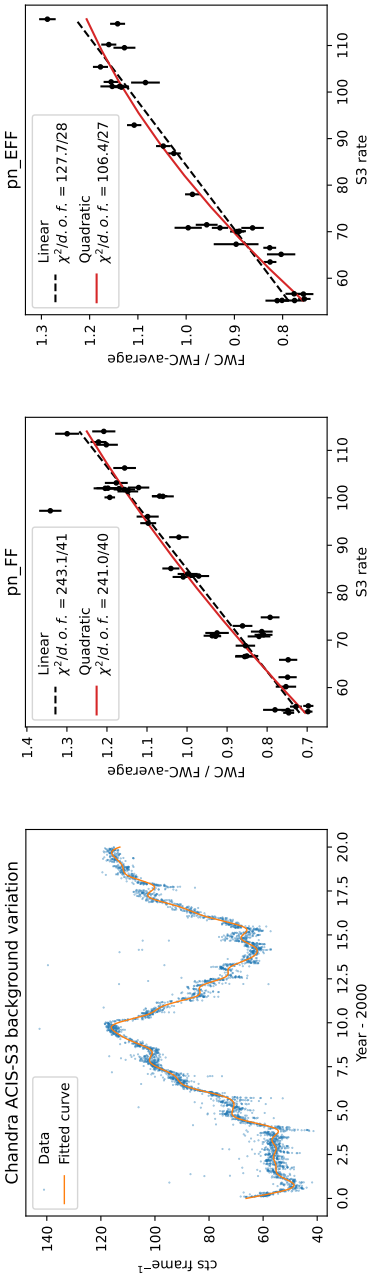

Figure 5.2: *Left:* Long term light curve of the *Chandra* ACIS-S3 particle background. *Middle and right:* EPIC-pn versus ACIS-S3 NXB levels for the FF and EFF observation modes, respectively. For both modes, a quadratic model (red) better fits the ratio than a linear model (black dashed).

et al. 2013). The photon index of *pow* is fixed to 1.41 (De Luca & Molendi 2004). We binned the spectra using the optimal binning algorithm (Kaastra & Bleeker 2016) and used the energy range 0.7–7.0 keV for spectral fitting. The Cash-statistic (Cash 1979) was adopted for calculating likelihood when optimizing parameters.

5.3.2 pn background scaling

XMM-Newton observations suffer from soft proton flares severely. Therefore, we need unexposed regions on the detectors to evaluate the level of the instrumental background. Different from the two EPIC-MOS detectors, there is no clean out of field of view (OoFoV) area on the four corners of the detector (e.g. Zhang et al. 2020; Marelli et al. 2021), i.e., the pn NXB level of each observation cannot be estimated using the OoFoV regions.

The particle backgrounds of both *XMM-Newton* and *Chandra* show long term variation that is anti-correlated with the solar activity (Gastaldello et al. 2022). We use *Chandra* ACIS-S3 long term monitoring data[4] as a reference to predict the NXB level of the pn detector for any given epoch. We first fit the ACIS-S3 light curve using a Gaussian process regression method (Ambikasaran et al. 2015) with the `George 0.4.0` package[5]. We adopted the product of an exponential squared kernel and a cosine kernel to represent the short term stochastic and long term periodic variation. The light curve and the fitted model are plotted in the left panel of Fig. 5.2.

We compared the pn FWC background 12–14 keV count rate with the predicted ACIS-S3 background count rate at each epoch of the calibration observations. We used a linear model and a quadratic model to fit the diagrams, respectively. χ^2 is used to evaluate the goodness of fit. We found that, for both the `full-frame` (FF) and `extended-full-frame` (EFF) observation mode, the diagrams are somewhat better fitted by quadratic models (see the middle and right panels of Fig. 5.2). We therefore applied the two quadratic models to science observations. For each observation epoch, we first predicted the ACIS-S3 NXB rate using the best-fit Gaussian process regression model, then we calculated the corresponding pn NXB rate either in FF or EFF modes based on the two quadratic models. We list the best-fit parameters for the two quadratic models in Table 5.2.

We evaluated the uncertainty of this method by calculating the stan-

[4] `https://space.mit.edu/~cgrant/cti/cti120.html`
[5] `https://github.com/dfm/george/tree/v0.4.0`

Table 5.2: Best-fit quadratic function parameters for scaling pn NXB.

Mode	a	b	c
FF	-0.000024	0.013	0.064
EFF	-0.000048	0.015	0.042

Note: The function is $y = ax^2 + bx + c$.

dard deviation of the residuals of the quadratic fitting. The standard deviations are 5.7% and 3.8% for the FF and EFF modes, respectively.

5.4 Morphological parameters

To investigate the connection between radio halos and cluster dynamic states in this series of papers, we adopt two X-ray morphological parameters. They are:

- concentration parameter (Santos et al. 2008),

$$c = \frac{F(r < r_{\rm core})}{F(r < r_{\rm ap})}, \tag{5.1}$$

  where F is the X-ray flux, $r_{\rm core}$ is the aperture of the core region, $r_{\rm ap}$ is the outer aperture;

- centroid shift (Mohr et al. 1993; Poole et al. 2006),

$$w = \left[\frac{1}{N_{\rm ap} - 1} \sum_i \left(\Delta_i - \bar{\Delta}\right)^2\right]^{1/2} \frac{1}{r_{\rm ap}}, \tag{5.2}$$

  where $N_{\rm ap}$ is the number of apertures, Δ_i the centroid for the ith aperture, $\bar{\Delta}$ the average centroid.

Following the convention of Cassano et al. (2010), we set $r_{\rm core} = 100$ kpc and $r_{\rm ap} = 500$ kpc. For the purpose of determining the centers of the analysis apertures, we smoothed both *XMM-Newton* and *Chandra* images and used the maximum intensity pixel after point source subtraction as the center of the analysis aperture. For parameter calculation, we input $\sigma = 30$ kpc Gaussian smoothed *Chandra* images but unsmoothed *XMM-Newton* images. The *Chandra* flux images were generated by subtracting the

blank-sky backgrounds that include CXB emission, while the background maps used for generating *XMM-Newton* flux images are NXB maps. Therefore, we subtract from the *XMM-Newton* images a universal constant as the CXB before calculating the morphological parameters. The universal value $S_{\rm CXB} = 2.3 \times 10^{-6}$ cts $\rm s^{-1}$ $\rm cm^{-2}$ $\rm arcmin^{-2}$ is the mean value of the cluster-free regions beyond r_{200} in the images of $z > 0.3$ clusters.

5.4.1 Individual measurements

In table 2 of Paper I, we presented single c and w measurements for all individual clusters. We note that for clusters with both usable *XMM-Newton* and *Chandra* data, the values are the mean values of the two measurements; the uncertainties are combinations of statistic and systematic uncertainties. We ask readers to refer to eqs. 3 and 4 of Paper I for the calculations. In this work, we present individual *XMM-Newton* and *Chandra* measurements of c and w in Table 5.3.

By comparing morphological parameters from two independent telescopes, we are able to evaluate the systematic uncertainties introduced during observations and data processing. We have 65 (sub)clusters that have morphological parameters measured by both *XMM-Newton* and *Chandra*. The *Chandra* versus *XMM-Newton* measurements of c and w are plotted in Fig. 5.3, where the insets in each panel illustrate the discrepancy of the measurements. In the next two subsections, we will explore the origins of the discrepancies.

5.4.2 Discrepancy in concentration parameter

In general, the c measurements from the two telescopes agree with each other well, with a mean deviation of 7% and a scatter of 11%. If we divide the sample into two different redshift ranges, the c from *Chandra* measurements are overall 15.3% and 5.3% higher than the *XMM-Newton* measurements, for the high redshift ($z > 0.3$) and low redshift ($z < 0.3$) populations, respectively.

The PSF of the telescopes is one of the major origins of the discrepancy in c, especially for distant cool core clusters, i.e., a large PSF smooths the core and leads to an underestimation of c. The result of the high redshift population agrees with this explanation. This discrepancy can be corrected if one recovers c from a surface brightness profile that takes instrumental PSF into account (e.g. Lovisari et al. 2017). However, for the low redshift

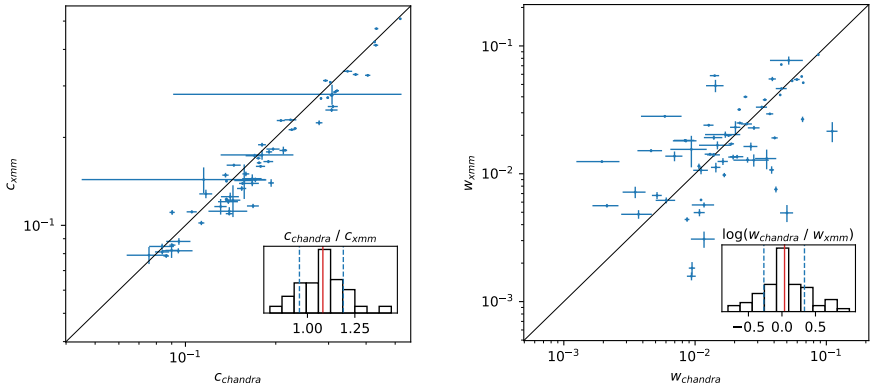

Figure 5.3: *Chandra* versus *XMM-Newton* measurements of c (*left*) and w (*right*), where black lines are diagonal. In each panel, the subplot is the histogram of the ratio between the measurements from the two telescopes. Red and blue dashed vertical lines indicate the mean and 1σ of the distributions, respectively. The large error bars of two *Chandra* c measurements are due to low count numbers.

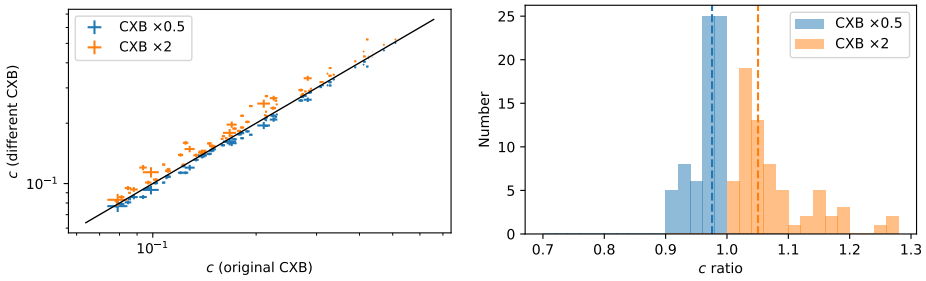

Figure 5.4: *Left:* Comparisons between c calculated using doubled (orange) and halved (blue) CXB levels and the original level for *XMM-Newton* clusters. The solid line is the diagonal. *Right:* Histograms of the discrepancy of the c values with doubled (orange) and halved (blue) CXB levels. The dashed lines denote median values of the two distributions.

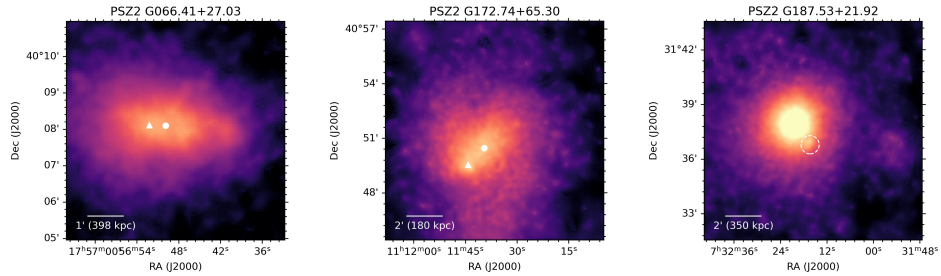

Figure 5.5: Examples of clusters with $w_{\rm Chandra} \gg w_{\rm XMM}$ (*left* and *middle*) and $w_{\rm Chandra} \ll w_{\rm XMM}$ (*right*). Triangle and point markers indicate the maximum intensity coordinates of the *Chandra* and *XMM-Newton* images, respectively. The dashed circle masks the residual of a point source near the bright core.

objects, the effect of the PSF should not be the case. In our analysis, we already smoothed the *Chandra* image with a 30 kpc kernel before the calculation, but not for the *XMM-Newton* image. This approach will make the smoothness of the *Chandra* images comparable to the *XMM-Newton* images at $z \sim 0.3$ and even higher for objects at lower redshifts, which means that PSF is not the only effect for the observed discrepancy. Therefore, we additionally check the systematic uncertainty due to CXB subtraction for low-z *XMM-Newton* clusters. We examined the discrepancy if increasing or decreasing the CXB level by a factor of two, respectively. The corresponding discrepancies are plotted in Fig. 5.4. A universal halved or doubled CXB levels can decrease or increase the measured c with median shifts of 2.5% and 5.1%. This analysis suggests that for our low-z *XMM-Newton* subsample, the CXB level could be globally higher than the universal value we use, which is obtained from the high-z subsample. This could be due to the large angular sizes of the low-z clusters, where more point sources are hidden behind the ICM emission and are not detected. This effect will be stronger on *XMM-Newton* observations due to its one order of magnitude larger PSF size than that of *Chandra*, and therefore is less sensitive to detect point sources in a cluster field.

Though *XMM-Newton* and *Chandra* have different instrumental properties, the measured c values are close enough for classifying cluster dynamic states in terms of the significance of the core. Our results extend the conclusion of Yuan & Han (2020) to a cross-instrument level, where they compared their *Chandra* c measurements with those in literature using dif-

ferent core-outer radii configurations (e.g. Cassano et al. 2013; Donahue et al. 2016; Andrade-Santos et al. 2017), and found that all the c measurements agree well.

5.4.3 Discrepancy in centroid shift

The centroid shift measurements show a larger discrepancy between the two telescopes. The distribution of $w_{\rm Chandra}/w_{\rm XMM}$ has a mean of 0.03 dex and a 1σ scatter of 0.34 dex. We did not find a redshift dependence of the ratio. Yuan & Han (2020) showed that the results of w have large discrepancy among different works, even if these are all with *Chandra* measurements.

We selected several objects with the largest difference to investigate the origin of the difference. We have five sources with discrepancies larger than $2\sigma_{\rm sys}$. Among them, G187.53+21.92 and G192.18+56.12 have much larger $w_{\rm XMM}$, while G172.74+65.30, G092.69+59.92 and G066.41+27.03 have much larger $w_{\rm Chandra}$.

For those clusters with $w_{\rm Chandra} \gg w_{\rm XMM}$, G092.69+59.92 is faint in the shallow *Chandra* image, which could lead to a large uncertainty. For the remaining two objects, we checked the coordinates of the aperture centers in maps of the two instruments and found large distances between them (see the left and middle panel of Fig. 5.5). The two clusters do not host bright cool cores, which means that the uncertainty of the maximum intensity pixel is based on count number. In addition, the count numbers of the *XMM-Newton* images are much larger than the *Chandra* images, suggesting that the X-ray peaks of *Chandra* images have large uncertainty, leading to overestimations of the w. The overestimation of w due to low count numbers is similar to the findings of Nurgaliev et al. (2013), where they also analyzed *Chandra* data and used similar $\sigma = 40$ kpc Gaussian convolved images to determine the centroid. Despite the overestimate of w, we note that due to the flat morphology of the two clusters, even though the X-ray peaks determined by the two telescopes are different, measurements of c agree with each other within a 10% level.

For the two $w_{\rm Chandra} \ll w_{\rm XMM}$ objects, we found that the cluster PSZ2 G187.53+21.92 has a peaked morphology and there is a residual of a point source filling near the core in the *XMM-Newton* image (see the right panel of Fig. 5.5). Due to the non-negligible PSF of *XMM-Newton*, if a bright point source is near the cool core, the traditional point source removing

process[6] cannot work perfectly due to the large gradient of the ICM emission. We also find a point source residual in G056.77+36.32, which is also a cluster with $w_{\rm Chandra} \ll w_{\rm XMM}$. However, we have no clear explanation for the discrepancy of G192.18+56.12.

5.4.4 Relaxation score

Recently, Ghirardini et al. (2021) proposed a novel method to combine the measurements of different morphological parameters into a new parameter, the relaxation score $\mathcal{R}$. The method calculates the joint cumulative probability function in a multi-dimensional parameter space. In our case, the joint cumulative distribution function in the space of c and w is

$$\mathcal{R}(c, w) = \int_{-\infty}^{C} \int_{W}^{\infty} f_{c,w}(c \leqslant C, w \geqslant W)\, \mathrm{d}w\, \mathrm{d}c, \tag{5.3}$$

where $f_{c,w}$ is the joint probability density function. Using this method, we are able to compare the degree of relaxation of clusters *within* our sample. We will use this parameter in the next section to explore the correlation between SB fluctuation and cluster dynamic state.

5.5 ICM density fluctuations on large scales

5.5.1 Calculation of 2D surface brightness fluctuations

The evaluation of the SB fluctuations, especially on large scales, is sensitive to the underlying SB model as illustrated in Zhuravleva et al. (2015) and Bonafede et al. (2018). For many clusters in our sample, the morphologies are clearly eccentric, which means a spherically symmetric β-model will lead to overestimation of the SB fluctuations. Therefore we used an elliptic β-model to fit the SB on large scales. For clusters with bright cool cores, we additionally used a second β-model to fit the core. For all clusters, we also added a constant model for the CXB during the fit. We fit the parameters directly in the 2D plane. The combination of the SB models can be written as

$$\begin{aligned} S_{\rm model}(x, y) = & Beta(x, y, x_1, y_1, s_1, r_1, \beta_1) + \\ & EBeta(x, y, x_2, y_2, s_2, r_2, \beta_2, \theta_2, e_2) + \\ & C(s_3), \end{aligned} \tag{5.4}$$

[6] Such as `https://cxc.cfa.harvard.edu/ciao/threads/diffuse_emission`

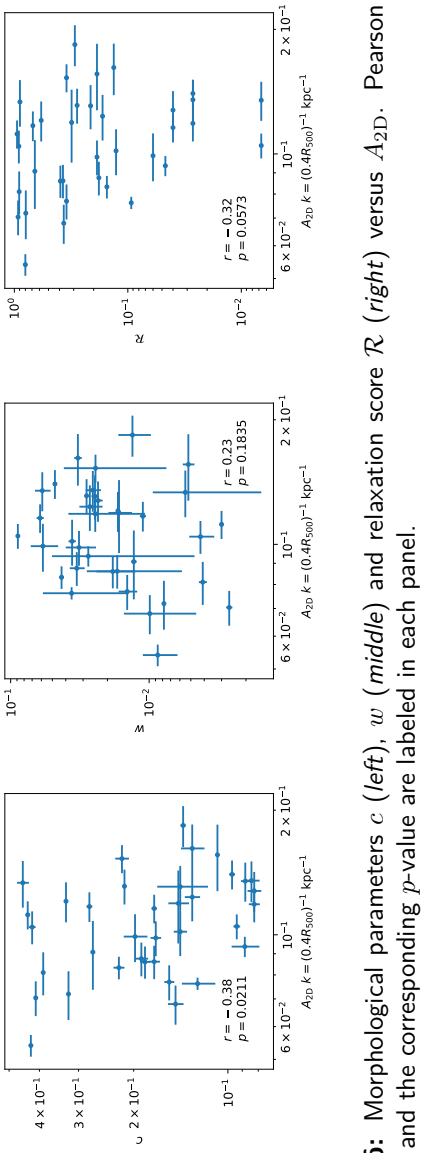

Figure 5.6: Morphological parameters c (*left*), w (*middle*) and relaxation score $\mathcal{R}$ (*right*) versus A_{2D}. Pearson correlation coefficient and the corresponding p-value are labeled in each panel.

Figure 5.7: Radio halo power (*left*), radio halo emissivity (*middle*) and cluster mass (*right*) versus A_{2D}. Marker size in left and middle panels indicates cluster mass. Red points in the left panel indicate upper limits of radio halo power.

where $Beta$ is the 2D β-model describing the cores, $EBeta$ the 2D elliptical β-model describing the bulk ICM, C the constant model describing the sky background, x_i, y_i the center of the ith model in image coordinate, s_i the SB normalization, r_i the β-model core radius, β_i the β-model slope. The residual map is calculated as

$$\delta S(x,y) = \frac{[N_{\rm obs}(x,y) - B(x,y)]/E(x,y) - C}{S_{\rm model}(x,y) - C}, \tag{5.5}$$

where $N_{\rm obs}$ is the observed count image, E the vignetting corrected exposure map, B the NXB map. To measure the fluctuations contributed by Poisson noise, we simulate Poisson randomization of model count images and convert them to the flux regime. The simulated noise residual maps can be expressed as

$$\delta S_{\rm noise}(x,y) = \frac{[N_{\rm rand}(x,y) - B(x,y)]/E(x,y) - C}{S_{\rm model}(x,y) - C}, \tag{5.6}$$

where

$$N_{\rm rand} \sim {\rm Pois}(\lambda = S_{\rm model} \times E + B_{\rm smoothed}), \tag{5.7}$$

is the Poisson randomization of the model count image, where $B_{\rm smoothed}$ is the smoothed NXB map. To minimize the uncertainty from the background, we choose $0.4r_{500}$ as the outer boundary for analysis, at which radius the flux from the ICM is approximately a factor of 2 higher than the sum of CXB and NXB.

We used a modified Δ-variance method (Arévalo et al. 2012) to calculate the 2D power spectra of the residual flux maps. This method cleanly compensates for data gaps and allows us to mask out regions of point sources and substructures of mergers. For each cluster, we obtained the power spectrum of SB fluctuation component $P_{\rm 2D}(k)$[7] by subtracting the noise power spectrum from the power spectrum of the residual map, where we used a Monte-Carlo approach to simulate 100 noise maps using Eq. 5.6. At large wavenumbers, the total power spectrum is dominated by the noise component. Therefore, we set a cutoff at the wavenumber where the power of the fluctuation component is twice that of the noise component. The noise removed SB fluctuation power spectra were converted to 2D amplitude spectra using the equation

$$A_{\rm 2D}(k) = \sqrt{P_{\rm 2D}(k) 2\pi k^2}. \tag{5.8}$$

[7]In this work, we adopt the definition of wave number $k \equiv 1/l$.

5.5.2 A_{2D} spectra and correlations with other parameters

E17 adopted a fixed scale of 660 kpc for calculating A_{2D}. Since our sample covers a wider range of mass, we adopt scales of $0.4 \times r_{500}$, which are close to 660 kpc for massive clusters. This scale also allows us to have at least two independent resolved components in the analysis aperture. After applying a wavenumber cut for each cluster, we have 36 objects whose A_{2D} spectra cover the wavenumber of $(0.4 \times r_{500})^{-1}$, where 11 objects have extended radio emission identified as radio halo. We note that the remaining 25 objects are not non radio halo clusters. Among them, 22 objects lack reasonable upper limits due to bad radio image quality, the presence of extended radio galaxies and residuals of source subtraction (Bruno et al. in prep.). Only three clusters have reasonable radio upper limits. The results of A_{2D} at $k = (0.4 \times r_{500})^{-1}$ are listed in the second column of Table 5.4.

We compared A_{2D} with morphological parameters (see Fig. 5.6). We calculated the Pearson correlation coefficients and corresponding p-values for A_{2D}–c, A_{2D}–w and A_{2D}–$\mathcal{R}$ in logarithmic space. We found that A_{2D} is marginally anti-correlated with the concentration parameter c with a p-value of 0.021, whereas the p-value of A_{2D}-w is 0.18, suggesting no correlation. As the combination of c and w, the relaxation score $\mathcal{R}$ is also marginally anti-correlated with A_{2D}, where the p-value 0.057 is mostly driven by the weak anti-correlation between c and A_{2D}. We conclude that for our sample, the ICM dynamic state is marginally correlated with SB fluctuations at a scale of $0.4 \times r_{500}$, implying that more relaxed clusters tend to have smaller SB fluctuations on large scales.

We also explored the correlations between A_{2D} and radio halo power $\mathcal{P}_{150\mathrm{MHz}}$, radio emissivity $J_{150\mathrm{MHz}}$ and cluster mass M_{500} (see Fig. 5.7). The radio halo power and emissivity are obtained from Paper III. The upper limits of radio power are obtained from Paper V (Bruno et al. in prep.). The p-values of the three pairs are 0.73, 0.62 and 0.44, respectively, which means that at least in our sample, A_{2D} is independent of the radio halo power, emissivity and cluster mass.

5.5.3 Turbulent velocity dispersion

Theoretical work illustrated that weak ICM turbulent motions excite isobaric perturbations, in which condition the density fluctuation is proportional to the turbulent Mach number, which is $\delta\rho/\rho_0 \simeq \eta\mathcal{M}_{1D}$ (Gaspari et al. 2014). We estimated the turbulent velocity dispersion based on the

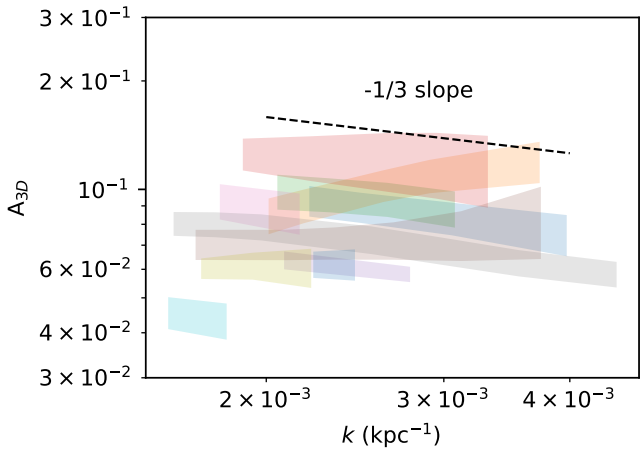

Figure 5.8: Recovered A_{3D} spectra for clusters with radio halo detection. The dashed line indicates the slope of Kolmogorov turbulent cascade.

following assumptions: 1) all surface brightness fluctuations are contributed by turbulent motions; 2) the triggered perturbations are isobaric; 3) the proportionality coefficient $\eta \simeq 1$ (Zhuravleva et al. 2014b) holds for both relaxed and merging clusters; 4) the ICM is isothermal in the radius of calculation, i.e. we use an average temperature to calculate the sound speed.

We used `pyproffit`[8] (Eckert et al. 2020) to recover the 3D density fluctuations from 2D SB fluctuations. The process is the same as described in E17. In short, we constructed an ellipsoid for the 3D density distribution using the elliptical β-model in Eq. 5.4 and then computed the power spectrum of the normalized emissivity distribution along the line of sight to convert P_{2D} to P_{3D} (Churazov et al. 2012). The final A_{3D} spectrum was converted as

$$A_{3D}(k) = \sqrt{P_{3D}(k) 4\pi k^3}. \tag{5.9}$$

The recovered A_{3D} spectra for the clusters hosting a radio halo are plotted in Fig. 5.8. Similar to A_{2D}, we took the value on the scale of $k = (0.4 \times r_{500})^{-1}$. The value of A_{3D} of each cluster is listed in the third column of Table 5.4. The A_{3D} values are linearly correlated with A_{2D} values, which means the relations of A_{2D} we obtained in Sect. 5.5.2 stand for A_{3D} as well.

[8] `https://github.com/domeckert/pyproffit`

For each cluster, the temperature is measured from a circular region with radius of $0.4 \times r_{500}$ centered at the X-ray centroid and with point sources and the center core component excluded. We excluded the MOS1 detector for spectral analysis because it has a chance to not cover the full region due to two missing chips. The measured temperatures are obtained following Sect. 5.3.1, and are listed in the fifth column of Table 5.4. We calculated the average sound speed within the region of analysis from the measured kT. The average ICM sound speed is $c_{\rm s} = \sqrt{\gamma kT/\mu m_{\rm p}} \simeq 507.3 \times \sqrt{kT/{\rm keV}}$ km s^{-1}. The one dimensional Mach number $\mathcal{M}_{\rm 1D}$ on the scale $1/k$ is identical to $A_{\rm 3D}(k)$ assuming $\eta = 1$. The three dimensional velocity dispersion is $\sigma_{v,{\rm 3D}} = \sqrt{3}\sigma_{v,{\rm 1D}} = \sqrt{3}\mathcal{M}_{\rm 1D}c_s$. The calculated $\sigma_{v,{\rm 3D}}$ values at $k = (0.4 \times r_{500})^{-1}$ are listed in the fourth column of Table 5.4.

By using the estimated 3D turbulent velocity dispersion, similar to E17, we explore its correlation to radio halo power (see the left panel of Fig. 5.9). The p-value of the Pearson correlation coefficient is 0.22, suggesting no correlation between radio power and turbulent velocity dispersion for our sample. Moreover, the velocity dispersions of the only three clusters with reliable radio upper limits are not lower than that of the population with radio halo detections. In the next section, we will further explore the connection between radio halo power and ICM properties from an angle of turbulent acceleration.

5.6 Relation between radio halo power and ICM thermodynamic properties

The radio halo power has been found to be correlated with the cluster mass (e.g. Cassano et al. 2006, 2007, 2013; Cuciti et al. 2021). With different sample selection functions and observation frequencies, the best-fit slopes in the $\mathcal{P}_\nu - M$ diagram range from 2.7 to 3.5 (Cuciti et al. 2021). Though we only have 11 clusters with both radio halo detection and velocity dispersion measurements, it is worthwhile to explore the relation between radio halo power and ICM properties using our measurements.

We inspected the relation between thermal and nonthermal phenomena in the scenario of turbulent acceleration assuming a quasi-steady state, which means the total amount of energy loss including synchrotron and the cosmic microwave background inverse Compton is balanced by the energy injection from acceleration. The turbulent dissipation rate per volume

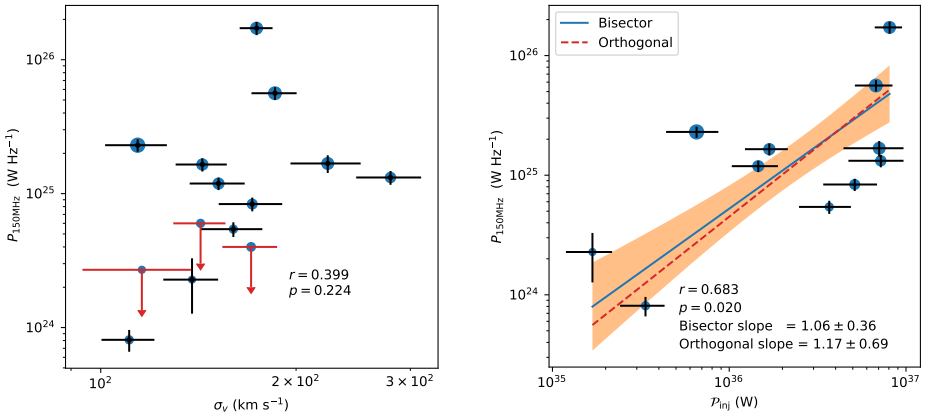

Figure 5.9: Radio halo power at 150 MHz versus turbulent velocity dispersion (*left*) and injection power from turbulent acceleration (*right*). Solid and dashed lines represent the best-fit results of BCES bisector and BCES Orthogonal, respectively. Orange band is the 1σ confidence band. Marker size indicates cluster mass.

is

$$\epsilon_{turb} = C_\epsilon \rho_{\mathrm{gas}} \sigma_{v,k}^3 k, \tag{5.10}$$

where the coefficient C_ϵ is calculated from the Kolmogorov constant, although its value has been found not to be universal (e.g. Sreenivasan 1995). The dissipation rate itself is the total flux of kinetic energy loss, where kinetic energy can be converted into heat, magnetic energy and relativistic particles. We introduce a coefficient C_{TTD} to denote the proportion of dissipation to particle acceleration through transit-time damping resonance (e.g. Chandran 2000), which is the most important turbulent acceleration mechanism, and the value of C_{TTD} is up to a few percent (Brunetti & Lazarian 2007). In a Kolmogorov nature of the turbulence, $\sigma_{v,k} \propto k^{-1/3}$ and the term $\sigma_{v,k}^3 k$ is a constant when k is in the inertial range of the turbulent cascade. For the $A_{3\mathrm{D}}$ spectra of our radio halo sample (see Fig. 5.8), the slope is close to -1/3, therefore we assume the Kolmogorov nature and use $k = (0.4 r_{500})^{-1}$ to estimate the dissipation rate. The total injection power of relativistic particles in the volume of the radio halo is

$$\mathcal{P}_{\mathrm{inj}} = \int_{V_{\mathrm{RH}}} C_{\mathrm{TTD}} C_\epsilon \rho_{\mathrm{gas}} \sigma_{v,k}^3 k \, \mathrm{d}V. \tag{5.11}$$

Assuming the two coefficients and $\sigma_{v,k}^3 k$ are invariant throughout the vol-

ume of the radio halo, then Eq. 5.11 can be written as

$$\mathcal{P}_{\rm inj} = C_{\rm TTD} C_\epsilon \sigma_{v,k}^3 k M_{\rm gas}(r_{\rm RH}), \tag{5.12}$$

where $r_{\rm RH}$ is the radius of the radio halo. The injected power is then proportional to the gas mass inside the volume of radius $r_{\rm RH}$.

Using Eq. 5.12, we estimated the power dissipated to particle acceleration for the 11 clusters. We first calculated the gas mass inside the volume of the radio halos in our sample. The 11 clusters do not show significant core components. Therefore, we extracted one dimensional SB profile for each cluster and fitted it using a simple projected density β-model (Cavaliere & Fusco-Femiano 1978), where the hydrogen number density $n_{\rm H}$ and projected surface brightness $S_{\rm X}$ are expressed as

$$n_{\rm H}(r) = n_{\rm H,0} \left[1 + \left(\frac{r}{r_{\rm c}}\right)^2\right]^{-3\beta/2}, \tag{5.13}$$

$$S_{\rm x}(r) = 2 \times \int_0^\infty n_{\rm H} \left(\sqrt{l^2 + r^2}\right)^2 \Lambda \, {\rm d}l, \tag{5.14}$$

where Λ is the cooling function and is approximately a constant for $kT \gtrsim 2.5$ keV. The gas density can be converted from hydrogen number density as $\rho_{\rm gas} \simeq 2.3 n_{\rm H} \mu m_{\rm H}$, where $\mu \simeq 0.6$ is the mean molecular weight. We integrated the gas mass using the best-fit density profile up to the radius of $r_{\rm RH}$. Following Bonafede et al. (2017), we use 2.6 e-folding radii as the $r_{\rm RH}$s. The e-folding radii are obtained from table 3 of Paper I. We set $C_\epsilon \simeq 5$ (Zhuravleva et al. 2014a) and arbitrarily set $C_{\rm TTD} = 0.05$ (e.g. Brunetti & Lazarian 2007) to calculate $\mathcal{P}_{\rm inj}$ for our sample. The resulting $\mathcal{P}_{150\rm MHz}$–$\mathcal{P}_{\rm inj}$ diagram is plotted in the right panel of Fig. 5.9. Different from the result in the $\mathcal{P}_\nu$–σ_v diagram, the corresponding p-value of the Pearson coefficient is improved to 0.020 in the $\mathcal{P}_\nu$–$\mathcal{P}_{\rm inj}$ plane, which shows that the radio monochromatic power at 150 MHz is marginally correlated with the injected power from turbulent dissipation. We use the code `BCES`[9], which uses the method taking bivariate correlated errors and intrinsic scatter into account (Akritas & Bershady 1996), to calculate the slope for our sample. The slope from the BCES bisector method is 1.06 ± 0.36. Alternatively, the BCES orthogonal method returns a slope of 1.17 ± 0.60. Both of the slopes from different methods agree with each other and are close to unity.

[9] `https://github.com/rsnemmen/BCES`

5.7 Discussion

The radio halo sample used in E17 is adopted from Cassano et al. (2013), where the mass range is $M_{500} > 6 \times 10^{14}\ M_{\odot}$ and the radio observation frequency is 1.4 GHz. The analysis of E17 has two main results. First, the $A_{\rm 2D}$ distribution shows bimodality, where clusters with radio halos have higher SB fluctuations than clusters with only upper limits of radio halo. Second, the radio halo power at 1.4 GHz is correlated with the turbulent velocity dispersion with a best-fit slope of 3.3 ± 0.7.

Our analysis cannot reproduce the first result directly, since among the 36 objects with $A_{\rm 2D}$ measurements, only 11 have radio halo detections and 3 have reasonable image quality to estimate upper limits. We cannot put reasonable upper limits for the other 22 objects due to either bad radio image quality or the emission significantly suffering from calibration artifacts. Nevertheless, the anti-correlation we found in the c–$A_{\rm 2D}$ plane (see Sect. 5.5.2) indirectly proves that radio halo clusters have higher $A_{\rm 2D}$ than clusters without a radio halo. Statistical studies show that the occurrence of radio halos is significantly higher in clusters with low concentration parameter (e.g. Cassano et al. 2010; Cuciti et al. 2015). Clusters with higher SB fluctuations are more likely to host less dense cores and therefore have a higher probability to host radio halos.

Different from the second conclusion of E17, our analysis does not find a correlation between $\mathcal{P}_{\rm 150MHz}$ and σ_v. To investigate this disagreement, we revisit the $\mathcal{P}_{\rm 1.4GHz}$–σ_v diagram of E17. We find that the Bullet Cluster and MACSJ0717 are in included that sample, which are two radio bright merging clusters that appear extremely disturbed in X-rays. Since an extremely disturbed morphology could overestimate the density fluctuation contributed by turbulent motions, we exclude the two clusters and compute the Pearson correlation coefficient again. For $\mathcal{P}_{\rm 1.4GHz}$ versus σ_v, the corresponding p-value increases from the original 2×10^{-6} to 0.05. However, it still suggests a marginal correlation. Therefore, besides the clusters with extremely disturbed morphology, the disagreement could be due to other factors. First, our sample size is half of the E17 sample, which means that it is more difficult to draw a statistically significant conclusion with a smaller sample. Second, the observation frequency of LoTSS is 150 MHz, which is an order of magnitude lower than the 1.4 GHz frequency used in E17. The energy of the CR population that is observed at 150 MHz is closer to that of the seed population, which means the density of that population

is less sensitive to acceleration efficiency. In this case, at low frequency, we will have more probability to observe ultra-steep spectrum radio halos (USSRHs) (e.g. Cuciti et al. 2021), which are below the detection limit in the GHz frequency bands. In other words, the radio halo sample in E17 only contains regular radio halos with relatively flat spectra, whereas the sample in our analysis could be the combination of USSRH and regular radio halos. The exact spectral nature of our sample needs to be further explored with high frequency follow-ups.

Though we did not find a correlation between the turbulent velocity dispersion and radio halo power for our sample, we successfully built up the scaling relation between injected turbulent power and the power emitted at 150 MHz (observer frame, k-correction applied) with a slope close to one. This slope suggests that the radio halo power, at least measured at 150 MHz, is determined not only by the turbulent velocity dispersion, but also by the ICM mass inside the radio halo volume. The two factors also reflect the underlying temperature - halo mass and baryonic mass - halo mass scaling relations. Since the high momentum CR population is more sensitive to the acceleration power, we speculate that the slope in the $\mathcal{P}_\nu$–$\mathcal{P}_{\rm inj}$ will be steeper for samples at higher observation frequencies. This is the first time we search for the relation between radio halo power and turbulent dissipation rate with radio-X-ray synergy. The slope needs to be further investigated with a larger sample and a wider frequency range.

5.8 Conclusion

We analyzed archival *XMM-Newton* and *Chandra* X-ray data of PSZ2 clusters in the footprint of LoTSS-DR2. We computed two morphological parameters, i.e. concentration parameter and centroid shift. Meanwhile, we calculated the large scale surface brightness and density fluctuation amplitude and estimate the turbulent velocity dispersion.

The measurements of concentration parameter obtained with the two telescopes agree well with each other with a global discrepancy of $7 \pm 11\%$. On the contrary, the discrepancy of the centroid shifts from the two telescopes is large, with an rms of 0.34 dex. We found that, the concentration parameter measured by *Chandra* is globally higher than by *XMM-Newton*, and the difference is more significant for the high redshift population, which can be explained by the different PSF sizes of the two telescopes. Nevertheless the difference in c is only 15% at $z > 0.3$. For the

low redshift population, the underestimation of the CXB level could introduce the discrepancy in the concentration parameter. Both artifacts of point source removal and low count number can introduce systematics to the centroid shift measurement.

We found a marginal correlation between the large scale surface brightness amplitude and concentration parameter. However, we did not find correlations between surface brightness fluctuations and cluster mass, radio halo power or radio halo emissivity. Using the turbulent velocity dispersion estimated from density fluctuations, we calculated the injected flux of turbulent acceleration. The injected flux is well correlated with radio power at 150 MHz with a slope consistent with unity within the uncertainties, suggesting that the turbulent acceleration scenario can well connect the observed cluster thermodynamic properties to the nonthermal properties.

Acknowledgements

This work is based on observations obtained with *XMM-Newton*, an ESA science mission with instruments and contributions directly funded by ESA Member States and NASA. This research has made use of data obtained from the *Chandra* Data Archive and the Chandra Source Catalog, and software provided by the *Chandra* X-ray Center (CXC) in the application packages CIAO and Sherpa. This research made use of Astropy[10], a community-developed core Python package for Astronomy (Astropy Collaboration et al. 2013, 2018).

[10] `http://www.astropy.org`

Table 5.3: Morphological parameters c and w measured using both *XMM-Newton* and *Chandra* images.

Name	Subcluster	$c_{\rm Chandra}$	$w_{\rm Chandra}$	$c_{\rm XMM}$	$w_{\rm XMM}$
PSZ2 G023.17+86.71		0.131 ± 0.006	0.0203 ± 0.0018	0.116 ± 0.007	0.0231 ± 0.0027
PSZ2 G031.93+78.71		—	—	0.2138 ± 0.0015	0.02826 ± 0.00024
PSZ2 G033.81+77.18		0.4270 ± 0.0014	0.01110 ± 0.00016	0.4242 ± 0.0007	0.00624 ± 0.00006
PSZ2 G040.58+77.12		0.224 ± 0.010	0.0060 ± 0.0010	0.2297 ± 0.0013	0.00620 ± 0.00033
PSZ2 G045.87+57.70		—	—	0.254 ± 0.005	0.0218 ± 0.0007
PSZ2 G046.88+56.48		0.0863 ± 0.0019	0.0219 ± 0.0012	0.0785 ± 0.0011	0.0250 ± 0.0005
PSZ2 G048.10+57.16		0.0905 ± 0.0021	0.0667 ± 0.0009	0.0856 ± 0.0008	0.0516 ± 0.0004
PSZ2 G048.75+53.18		0.340 ± 0.008	0.0065 ± 0.0012	—	—
PSZ2 G049.18+65.05		0.287 ± 0.017	0.0080 ± 0.0031	—	—
PSZ2 G049.32+44.37		0.180 ± 0.005	0.0111 ± 0.0014	0.1887 ± 0.0029	0.0106 ± 0.0007
PSZ2 G050.46+67.54		0.361 ± 0.005	0.0019 ± 0.0005	—	—
PSZ2 G053.53+59.52		0.1370 ± 0.0013	0.0167 ± 0.0005	0.1417 ± 0.0014	0.0098 ± 0.0004
PSZ2 G054.99+53.41		0.154 ± 0.005	0.0195 ± 0.0016	0.1337 ± 0.0024	0.0135 ± 0.0006
PSZ2 G055.59+31.85		0.315 ± 0.004	0.0095 ± 0.0005	0.2858 ± 0.0019	0.00183 ± 0.00021
PSZ2 G056.77+36.32		0.293 ± 0.006	0.0021 ± 0.0005	0.3129 ± 0.0014	0.00563 ± 0.00018
PSZ2 G057.61+34.93		0.105 ± 0.004	0.0139 ± 0.0016	0.1112 ± 0.0013	0.0141 ± 0.0005
PSZ2 G057.78+52.32	E	—	—	0.2256 ± 0.0018	0.0061 ± 0.0005
PSZ2 G057.78+52.32	W	—	—	0.225 ± 0.006	0.0161 ± 0.0014
PSZ2 G057.92+27.64		0.433 ± 0.006	0.0094 ± 0.0007	0.4712 ± 0.0022	0.00158 ± 0.00011
PSZ2 G058.29+18.55	E	0.140 ± 0.004	0.0141 ± 0.0011	0.1096 ± 0.0006	0.05856 ± 0.00022
PSZ2 G058.29+18.55	W	—	—	0.4215 ± 0.0033	0.0134 ± 0.0005
PSZ2 G059.47+33.06		0.405 ± 0.008	0.0130 ± 0.0012	0.3261 ± 0.0028	0.01423 ± 0.00030
PSZ2 G060.55+27.00		0.431 ± 0.008	0.0037 ± 0.0010	0.413 ± 0.004	0.0048 ± 0.0004
PSZ2 G062.94+43.69		—	—	0.43614 ± 0.00034	0.003000 ± 0.000019
PSZ2 G065.28+44.53		0.211 ± 0.007	0.0344 ± 0.0018	—	—
PSZ2 G066.41+27.03		0.095 ± 0.011	0.050 ± 0.006	0.0818 ± 0.0016	0.0049 ± 0.0008

Table 5.3: continued.

Name	Subcluster	$c_{\rm Chandra}$	$w_{\rm Chandra}$	$c_{\rm XMM}$	$w_{\rm XMM}$
PSZ2 G066.68+68.44		0.347 ± 0.012	0.0117 ± 0.0023	0.3366 ± 0.0021	0.00570 ± 0.00026
PSZ2 G067.17+67.46		0.2320 ± 0.0029	0.0445 ± 0.0006	0.2146 ± 0.0014	0.04139 ± 0.00024
PSZ2 G067.52+34.75		—	—	0.3888 ± 0.0024	0.00410 ± 0.00027
PSZ2 G068.36+81.81		—	—	0.1373 ± 0.0031	0.0269 ± 0.0008
PSZ2 G070.89+49.26		—	—	0.136 ± 0.004	0.0206 ± 0.0012
PSZ2 G071.21+28.86		—	—	0.064 ± 0.004	0.0129 ± 0.0021
PSZ2 G071.39+59.54		0.167 ± 0.009	0.0139 ± 0.0022	0.1392 ± 0.0031	0.0192 ± 0.0007
PSZ2 G071.63+29.78		0.084 ± 0.005	0.0383 ± 0.0017	0.0811 ± 0.0016	0.0107 ± 0.0007
PSZ2 G072.62+41.46		0.1370 ± 0.0018	0.0217 ± 0.0007	0.1228 ± 0.0016	0.0318 ± 0.0005
PSZ2 G073.31+67.52		0.167 ± 0.012	0.015 ± 0.004	0.144 ± 0.005	0.0167 ± 0.0012
PSZ2 G073.97-27.82		0.2830 ± 0.0014	0.01070 ± 0.00027	0.2718 ± 0.0028	0.0114 ± 0.0006
PSZ2 G074.37+71.11		0.143 ± 0.020	0.028 ± 0.006	—	—
PSZ2 G076.55+60.29		0.238 ± 0.017	0.029 ± 0.004	—	—
PSZ2 G077.90-26.63		0.226 ± 0.005	0.0189 ± 0.0009	0.2125 ± 0.0018	0.01715 ± 0.00026
PSZ2 G080.16+57.65		0.139 ± 0.011	0.0322 ± 0.0031	0.1205 ± 0.0021	0.0332 ± 0.0008
PSZ2 G080.41-33.24		0.2150 ± 0.0020	0.0454 ± 0.0005	0.1806 ± 0.0009	0.07153 ± 0.00019
PSZ2 G080.64+64.31		0.453 ± 0.012	0.0062 ± 0.0015	—	—
PSZ2 G081.02+50.57		—	—	0.149 ± 0.005	0.0377 ± 0.0014
PSZ2 G081.72+70.15		0.121 ± 0.018	0.018 ± 0.005	—	—
PSZ2 G083.29-31.03		0.189 ± 0.007	0.0404 ± 0.0022	0.1653 ± 0.0020	0.0191 ± 0.0004
PSZ2 G083.86+85.09		0.196 ± 0.010	0.0371 ± 0.0023	0.1824 ± 0.0022	0.0294 ± 0.0005
PSZ2 G084.10+58.72		0.18 ± 0.05	0.028 ± 0.008	0.174 ± 0.007	0.0128 ± 0.0014
PSZ2 G084.13-35.41		—	—	0.095 ± 0.006	0.0379 ± 0.0021
PSZ2 G084.69+42.28		—	—	0.270 ± 0.004	0.0129 ± 0.0006
PSZ2 G086.54-26.67		0.304 ± 0.006	0.0054 ± 0.0009	—	—
PSZ2 G086.93+53.18		0.140 ± 0.021	0.017 ± 0.005	0.112 ± 0.004	0.0203 ± 0.0011

Table 5.3: continued.

Name	Subcluster	c_{Chandra}	w_{Chandra}	c_{XMM}	w_{XMM}
PSZ2 G087.39+50.92		—	—	0.213 ± 0.012	0.0234 ± 0.0021
PSZ2 G088.98+55.07		0.31 ± 0.22	0.052 ± 0.015	0.281 ± 0.022	0.077 ± 0.006
PSZ2 G089.52+62.34		0.113 ± 0.009	0.0320 ± 0.0023	—	—
PSZ2 G091.79-27.00		—	—	0.073 ± 0.006	0.0454 ± 0.0025
PSZ2 G092.69+59.92		0.12 ± 0.07	0.111 ± 0.011	0.143 ± 0.014	0.022 ± 0.004
PSZ2 G092.71+73.46		0.159 ± 0.004	0.0163 ± 0.0015	0.1500 ± 0.0027	0.0125 ± 0.0008
PSZ2 G093.94-38.82	EN	—	—	0.2143 ± 0.0024	0.0407 ± 0.0006
PSZ2 G093.94-38.82	ES	—	—	0.1930 ± 0.0023	0.0318 ± 0.0006
PSZ2 G093.94-38.82	W	—	—	0.3285 ± 0.0031	0.0168 ± 0.0005
PSZ2 G094.44+36.13		0.310 ± 0.012	0.0085 ± 0.0017	0.2550 ± 0.0032	0.0181 ± 0.0005
PSZ2 G094.56+51.03		—	—	0.102 ± 0.004	0.0569 ± 0.0017
PSZ2 G094.61-41.24		—	—	0.3228 ± 0.0013	0.00782 ± 0.00022
PSZ2 G095.22+67.41		—	—	0.1246 ± 0.0023	0.0206 ± 0.0009
PSZ2 G096.83+52.49		0.209 ± 0.004	0.0087 ± 0.0009	—	—
PSZ2 G097.52+51.70		—	—	0.217 ± 0.008	0.0192 ± 0.0011
PSZ2 G097.72+38.12		0.1760 ± 0.0031	0.0242 ± 0.0008	0.1637 ± 0.0014	0.03998 ± 0.00032
PSZ2 G099.48+55.60		0.084 ± 0.008	0.0281 ± 0.0029	0.0847 ± 0.0019	0.0229 ± 0.0008
PSZ2 G099.86+58.45		0.141 ± 0.010	0.0266 ± 0.0032	0.125 ± 0.004	0.0163 ± 0.0012
PSZ2 G100.14+41.67		0.2500 ± 0.0030	0.0567 ± 0.0006	—	—
PSZ2 G100.45-38.42		—	—	0.4113 ± 0.0015	0.00264 ± 0.00014
PSZ2 G103.40-32.99		—	—	0.1076 ± 0.0012	0.0052 ± 0.0005
PSZ2 G105.55+77.21		—	—	0.1820 ± 0.0023	0.0252 ± 0.0006
PSZ2 G106.41+50.82		0.369 ± 0.008	0.0180 ± 0.0010	0.328 ± 0.004	0.0199 ± 0.0005
PSZ2 G106.61+66.71		0.140 ± 0.032	0.051 ± 0.008	—	—
PSZ2 G107.10+65.32	N	0.1130 ± 0.0026	0.0869 ± 0.0010	0.1019 ± 0.0017	0.0853 ± 0.0007
PSZ2 G107.10+65.32	S	0.1360 ± 0.0033	0.0340 ± 0.0012	0.1485 ± 0.0027	0.0379 ± 0.0007

Table 5.3: continued.

Name	Subcluster	c_{Chandra}	w_{Chandra}	c_{XMM}	w_{XMM}
PSZ2 G109.97+52.84		0.334 ± 0.005	0.0082 ± 0.0009	—	—
PSZ2 G111.75+70.37		0.095 ± 0.009	0.0596 ± 0.0030	0.0881 ± 0.0023	0.0547 ± 0.0010
PSZ2 G112.35-32.86		—	—	0.263 ± 0.010	0.0135 ± 0.0014
PSZ2 G112.48+56.99		0.174 ± 0.005	0.0046 ± 0.0010	—	—
PSZ2 G113.29-29.69		0.178 ± 0.006	0.0084 ± 0.0015	0.1592 ± 0.0015	0.0182 ± 0.0004
PSZ2 G113.91-37.01		0.171 ± 0.015	0.046 ± 0.004	0.1431 ± 0.0026	0.0464 ± 0.0007
PSZ2 G114.31+64.89		0.193 ± 0.004	0.0144 ± 0.0012	0.140 ± 0.004	0.0112 ± 0.0010
PSZ2 G114.79-33.71		0.145 ± 0.008	0.0117 ± 0.0024	0.1607 ± 0.0018	0.0031 ± 0.0004
PSZ2 G114.99+70.36		0.146 ± 0.006	0.0172 ± 0.0018	—	—
PSZ2 G116.32-36.33	N	0.157 ± 0.011	0.0094 ± 0.0029	0.142 ± 0.019	0.016 ± 0.004
PSZ2 G116.32-36.33	S	—	—	0.297 ± 0.013	0.0091 ± 0.0015
PSZ2 G116.50-44.47		—	—	0.130 ± 0.007	0.0560 ± 0.0024
PSZ2 G121.03+57.02		0.098 ± 0.008	0.110 ± 0.004	—	—
PSZ2 G121.13+49.64		—	—	0.099 ± 0.005	0.0328 ± 0.0019
PSZ2 G123.00-35.52		—	—	0.156 ± 0.005	0.0239 ± 0.0011
PSZ2 G123.66+67.25		0.250 ± 0.030	0.016 ± 0.005	—	—
PSZ2 G124.20-36.48	N	0.3040 ± 0.0029	0.0549 ± 0.0005	0.3086 ± 0.0025	0.05331 ± 0.00035
PSZ2 G124.20-36.48	S	0.0903 ± 0.0018	0.0251 ± 0.0007	0.1107 ± 0.0021	0.0128 ± 0.0006
PSZ2 G125.71+53.86		0.212 ± 0.006	0.0070 ± 0.0010	0.180 ± 0.005	0.0137 ± 0.0012
PSZ2 G126.61-37.63		—	—	0.170 ± 0.006	0.0088 ± 0.0011
PSZ2 G127.50-30.52		—	—	0.116 ± 0.007	0.0139 ± 0.0020
PSZ2 G132.54-42.16		—	—	0.211 ± 0.009	0.0026 ± 0.0016
PSZ2 G133.59+50.68		—	—	0.093 ± 0.005	0.0194 ± 0.0022
PSZ2 G133.60+69.04		0.087 ± 0.009	0.0380 ± 0.0035	—	—
PSZ2 G134.70+48.91		0.279 ± 0.007	0.0035 ± 0.0007	0.224 ± 0.004	0.0072 ± 0.0007
PSZ2 G135.17+65.43		0.105 ± 0.019	0.047 ± 0.008	—	—

Table 5.3: continued.

Name	Subcluster	c_{Chandra}	w_{Chandra}	c_{XMM}	w_{XMM}
PSZ2 G135.19+57.88		0.166 ± 0.009	0.0133 ± 0.0026	—	—
PSZ2 G136.92+59.46		—	—	0.0937 ± 0.0023	0.0887 ± 0.0012
PSZ2 G137.74-27.08		—	—	0.1462 ± 0.0024	0.0431 ± 0.0007
PSZ2 G138.32-39.82		0.198 ± 0.007	0.0132 ± 0.0013	—	—
PSZ2 G139.18+56.37		0.090 ± 0.004	0.0388 ± 0.0025	0.082 ± 0.005	0.0552 ± 0.0021
PSZ2 G143.26+65.24		0.168 ± 0.008	0.0247 ± 0.0024	0.1165 ± 0.0020	0.0245 ± 0.0006
PSZ2 G145.65+59.30		—	—	0.144 ± 0.007	0.0120 ± 0.0015
PSZ2 G148.36+75.23		0.206 ± 0.009	0.0527 ± 0.0024	—	—
PSZ2 G149.22+54.18		0.1360 ± 0.0034	0.0037 ± 0.0008	—	—
PSZ2 G149.75+34.68		0.1750 ± 0.0029	0.0649 ± 0.0010	0.1696 ± 0.0012	0.05768 ± 0.00028
PSZ2 G150.56+58.32		0.144 ± 0.008	0.0143 ± 0.0022	0.122 ± 0.015	0.049 ± 0.005
PSZ2 G151.19+48.27		0.076 ± 0.012	0.035 ± 0.006	0.079 ± 0.005	0.0131 ± 0.0023
PSZ2 G160.83+81.66		0.307 ± 0.014	0.0209 ± 0.0024	0.248 ± 0.004	0.0136 ± 0.0004
PSZ2 G163.69+53.52		0.198 ± 0.006	0.0083 ± 0.0014	—	—
PSZ2 G163.87+48.54		0.4610 ± 0.0035	0.00161 ± 0.00034	—	—
PSZ2 G164.65+46.37		0.246 ± 0.010	0.0605 ± 0.0021	—	—
PSZ2 G165.06+54.13		0.188 ± 0.005	0.0177 ± 0.0015	—	—
PSZ2 G165.46+66.15		0.070 ± 0.005	0.0331 ± 0.0031	—	—
PSZ2 G165.95+41.01		—	—	0.658 ± 0.028	0.042 ± 0.006
PSZ2 G166.09+43.38		0.190 ± 0.005	0.0127 ± 0.0011	0.1784 ± 0.0025	0.0240 ± 0.0005
PSZ2 G166.62+42.13		0.069 ± 0.006	0.0348 ± 0.0030	—	—
PSZ2 G168.33+69.73		0.264 ± 0.030	0.019 ± 0.004	—	—
PSZ2 G170.98+39.45		0.114 ± 0.016	0.027 ± 0.007	—	—
PSZ2 G172.63+35.15		0.184 ± 0.009	0.0201 ± 0.0021	—	—
PSZ2 G172.74+65.30		0.208 ± 0.006	0.0413 ± 0.0012	0.2284 ± 0.0019	0.0075 ± 0.0004
PSZ2 G175.60+35.47		0.266 ± 0.011	0.0105 ± 0.0020	—	—

Table 5.3: continued.

Name	Subcluster	c_{Chandra}	w_{Chandra}	c_{XMM}	w_{XMM}
PSZ2 G176.27+37.54		0.243 ± 0.017	0.019 ± 0.004	—	—
PSZ2 G179.09+60.12		0.520 ± 0.004	0.0087 ± 0.0004	0.5093 ± 0.0021	0.00439 ± 0.00018
PSZ2 G180.60+76.65		0.289 ± 0.006	0.0024 ± 0.0005	—	—
PSZ2 G180.88+31.04		—	—	0.101 ± 0.011	0.018 ± 0.004
PSZ2 G181.06+48.47		0.141 ± 0.011	0.0695 ± 0.0030	—	—
PSZ2 G182.59+55.83		0.2980 ± 0.0030	0.0051 ± 0.0004	0.2735 ± 0.0025	0.0068 ± 0.0004
PSZ2 G183.90+42.99		—	—	0.156 ± 0.005	0.0182 ± 0.0011
PSZ2 G184.68+28.91		0.307 ± 0.005	0.0108 ± 0.0010	0.2783 ± 0.0022	0.00497 ± 0.00032
PSZ2 G186.37+37.26		0.155 ± 0.004	0.0046 ± 0.0010	0.1391 ± 0.0016	0.0152 ± 0.0004
PSZ2 G186.99+38.65		0.199 ± 0.008	0.0385 ± 0.0021	—	—
PSZ2 G187.53+21.92		0.320 ± 0.005	0.0019 ± 0.0007	0.2890 ± 0.0018	0.01245 ± 0.00023
PSZ2 G189.31+59.24		0.245 ± 0.004	0.0476 ± 0.0008	—	—
PSZ2 G190.61+66.46		0.105 ± 0.016	0.029 ± 0.006	—	—
PSZ2 G192.18+56.12		0.170 ± 0.011	0.0059 ± 0.0020	0.1731 ± 0.0026	0.0282 ± 0.0006
PSZ2 G193.63+54.85		—	—	0.167 ± 0.007	0.0562 ± 0.0019
PSZ2 G194.98+54.12		0.184 ± 0.014	0.0607 ± 0.0035	—	—
PSZ2 G195.60+44.06	E1	—	—	0.094 ± 0.006	0.0194 ± 0.0024
PSZ2 G195.60+44.06	E2	0.117 ± 0.006	0.0659 ± 0.0019	0.128 ± 0.004	0.0267 ± 0.0013
PSZ2 G195.60+44.06	W1	—	—	0.283 ± 0.008	0.0086 ± 0.0010
PSZ2 G195.60+44.06	W2	—	—	0.0970 ± 0.0021	0.0479 ± 0.0007
PSZ2 G205.90+73.76		0.212 ± 0.018	0.0135 ± 0.0032	—	—

Table 5.4: Power spectral analysis results and temperature measurements of the sample.

Name	A_{2D}	A_{3D}	$\sigma_{v,3D}$ km s^{-1}	kT keV
PSZ2G031.93+78.71	0.131 ± 0.013	0.089 ± 0.009	138 ± 13	3.27 ± 0.04
PSZ2G033.81+77.18	0.0540 ± 0.0033	0.0375 ± 0.0023	75 ± 5	5.392 ± 0.031
PSZ2G040.58+77.12	—	—	—	4.64 ± 0.09
PSZ2G046.88+56.48	0.128 ± 0.014	0.086 ± 0.010	171 ± 19	5.28 ± 0.10
PSZ2G048.10+57.16	0.135 ± 0.015	0.097 ± 0.010	160 ± 17	3.68 ± 0.04
PSZ2G049.32+44.37	—	—	—	4.87 ± 0.14
PSZ2G053.53+59.52	0.184 ± 0.021	0.125 ± 0.014	280 ± 32	6.76 ± 0.18
PSZ2G054.99+53.41	0.119 ± 0.024	0.085 ± 0.017	210 ± 40	7.84 ± 0.27
PSZ2G055.59+31.85	—	—	—	7.28 ± 0.13
PSZ2G056.77+36.32	—	—	—	4.86 ± 0.05
PSZ2G057.61+34.93	—	—	—	4.57 ± 0.09
PSZ2G057.78+52.32E	—	—	—	2.98 ± 0.08
PSZ2G057.92+27.64	0.134 ± 0.017	0.090 ± 0.012	145 ± 19	3.51 ± 0.05
PSZ2G058.29+18.55E	0.0762 ± 0.0026	0.0512 ± 0.0017	91.2 ± 3.1	4.28 ± 0.04
PSZ2G058.29+18.55W	—	—	—	2.63 ± 0.18
PSZ2G059.47+33.06	—	—	—	6.79 ± 0.16
PSZ2G060.55+27.00	0.104 ± 0.010	0.071 ± 0.006	143 ± 13	5.47 ± 0.15
PSZ2G062.94+43.69	0.112 ± 0.009	0.073 ± 0.006	107 ± 8	2.868 ± 0.009
PSZ2G066.41+27.03	0.094 ± 0.005	0.0629 ± 0.0035	174 ± 10	10.29 ± 0.31
PSZ2G066.68+68.44	—	—	—	5.05 ± 0.07
PSZ2G067.17+67.46	0.083 ± 0.005	0.059 ± 0.004	152 ± 10	9.03 ± 0.16

Table 5.4: continued.

Name	A_{2D}	A_{3D}	$\sigma_{v,3D}$ km s^{-1}	kT keV
PSZ2G067.52+34.75	0.081 ± 0.010	0.056 ± 0.007	107 ± 13	4.92 ± 0.12
PSZ2G068.36+81.81	—	—	—	6.77 ± 0.32
PSZ2G071.39+59.54	—	—	—	6.37 ± 0.22
PSZ2G071.63+29.78	0.119 ± 0.011	0.084 ± 0.008	170 ± 17	5.52 ± 0.17
PSZ2G072.62+41.46	0.123 ± 0.016	0.087 ± 0.011	233 ± 30	9.67 ± 0.25
PSZ2G073.97-27.82	0.117 ± 0.010	0.078 ± 0.006	200 ± 17	8.90 ± 0.24
PSZ2G077.90-26.63	—	—	—	4.96 ± 0.07
PSZ2G080.16+57.65	0.162 ± 0.023	0.109 ± 0.016	197 ± 28	4.35 ± 0.13
PSZ2G080.41-33.24	0.099 ± 0.013	0.065 ± 0.009	143 ± 19	6.44 ± 0.08
PSZ2G083.29-31.03	—	—	—	8.74 ± 0.29
PSZ2G083.86+85.09	0.088 ± 0.008	0.060 ± 0.006	123 ± 12	5.59 ± 0.13
PSZ2G084.69+42.28	0.091 ± 0.017	0.064 ± 0.012	116 ± 22	4.45 ± 0.15
PSZ2G092.71+73.46	0.077 ± 0.007	0.054 ± 0.005	124 ± 12	7.12 ± 0.24
PSZ2G093.94-38.82W	0.121 ± 0.013	0.081 ± 0.009	115 ± 13	2.71 ± 0.09
PSZ2G094.44+36.13	—	—	—	3.77 ± 0.14
PSZ2G094.61-41.24	0.072 ± 0.010	0.049 ± 0.007	72 ± 10	2.882 ± 0.021
PSZ2G095.22+67.41	—	—	—	2.86 ± 0.15
PSZ2G097.72+38.12	0.098 ± 0.009	0.070 ± 0.007	152 ± 15	6.26 ± 0.14
PSZ2G099.48+55.60	0.135 ± 0.015	0.096 ± 0.011	151 ± 17	3.31 ± 0.09
PSZ2G100.45-38.42	0.070 ± 0.007	0.048 ± 0.005	68 ± 7	2.682 ± 0.025
PSZ2G103.40-32.99	0.156 ± 0.029	0.107 ± 0.020	144 ± 27	2.45 ± 0.18
PSZ2G105.55+77.21	—	—	—	3.25 ± 0.09

Table 5.4: continued.

Name	A_{2D}	A_{3D}	$\sigma_{v,3D}$ km s^{-1}	kT keV
PSZ2G106.41+50.82	—	—	—	4.79 ± 0.12
PSZ2G107.10+65.32N	—	—	—	7.17 ± 0.27
PSZ2G107.10+65.32S	0.102 ± 0.013	0.070 ± 0.009	162 ± 21	7.17 ± 0.27
PSZ2G111.75+70.37	—	—	—	6.10 ± 0.23
PSZ2G113.29-29.69	—	—	—	4.53 ± 0.07
PSZ2G113.91-37.01	—	—	—	7.60 ± 0.25
PSZ2G114.79-33.71	—	—	—	4.66 ± 0.10
PSZ2G134.70+48.91	—	—	—	7.3 ± 0.8
PSZ2G136.92+59.46	0.105 ± 0.007	0.073 ± 0.005	114 ± 8	3.28 ± 0.17
PSZ2G137.74-27.08	—	—	—	2.94 ± 0.07
PSZ2G143.26+65.24	0.131 ± 0.016	0.089 ± 0.011	224 ± 28	8.50 ± 0.31
PSZ2G149.75+34.68	0.116 ± 0.009	0.080 ± 0.006	186 ± 15	7.24 ± 0.13
PSZ2G166.09+43.38	0.086 ± 0.008	0.061 ± 0.005	143 ± 13	7.35 ± 0.20
PSZ2G172.74+65.30	0.153 ± 0.012	0.110 ± 0.009	185 ± 15	3.80 ± 0.06
PSZ2G179.09+60.12	—	—	—	4.23 ± 0.07
PSZ2G182.59+55.83	—	—	—	6.30 ± 0.13
PSZ2G184.68+28.91	—	—	—	6.07 ± 0.19
PSZ2G186.37+37.26	0.068 ± 0.007	0.044 ± 0.005	114 ± 12	8.90 ± 0.20
PSZ2G187.53+21.92	—	—	—	6.25 ± 0.12
PSZ2G192.18+56.12	0.086 ± 0.008	0.062 ± 0.006	111 ± 10	4.29 ± 0.11
PSZ2G195.60+44.06W2	0.140 ± 0.011	0.089 ± 0.007	186 ± 15	5.91 ± 0.17

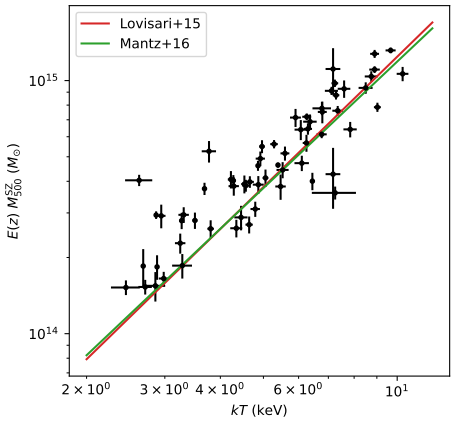

Figure 5.10: Mass versus temperature of our sample. The overplotted lines are scaling relations of Lovisari et al. (2015) (red) and Mantz et al. (2016) (green).

5.A Temperature measurements of the sample

We plotted mass versus temperature in Fig. 5.10. Though our spectral extraction region is $0.4r_{500}$, the measurements are close to the $M_{500} - kT_{500}$ scaling relation (e.g., Lovisari et al. 2015; Mantz et al. 2016).

Bibliography

Abell, G. O. 1958, ApJS, 3, 211

Ackermann, M., Ajello, M., Albert, A., et al. 2016, ApJ, 819, 149

Adam, R., Goksu, H., Brown, S., Rudnick, L., & Ferrari, C. 2021, A&A, 648, A60

Akamatsu, H., Hoshino, A., Ishisaki, Y., et al. 2011, PASJ, 63, S1019

Akamatsu, H. & Kawahara, H. 2013, PASJ, 65, 16

Akamatsu, H., Mizuno, M., Ota, N., et al. 2017, A&A, 600, A100

Akamatsu, H., van Weeren, R. J., Ogrean, G. A., et al. 2015, A&A, 582, A87

Akritas, M. G. & Bershady, M. A. 1996, ApJ, 470, 706

Allen, S. W., Evrard, A. E., & Mantz, A. B. 2011, ARA&A, 49, 409

Ambikasaran, S., Foreman-Mackey, D., Greengard, L., Hogg, D. W., & O'Neil, M. 2015, IEEE Transactions on Pattern Analysis and Machine Intelligence, 38, 252

Andrade-Santos, F., Jones, C., Forman, W. R., et al. 2017, ApJ, 843, 76

Andrade-Santos, F., van Weeren, R. J., Di Gennaro, G., et al. 2019, ApJ, 887, 31

Arévalo, P., Churazov, E., Zhuravleva, I., Hernández-Monteagudo, C., & Revnivtsev, M. 2012, MNRAS, 426, 1793

Arnaud, M., Pointecouteau, E., & Pratt, G. W. 2007, A&A, 474, L37

Ascasibar, Y. & Markevitch, M. 2006, ApJ, 650, 102

Astropy Collaboration, Price-Whelan, A. M., Sipőcz, B. M., et al. 2018, AJ, 156, 123

Astropy Collaboration, Robitaille, T. P., Tollerud, E. J., et al. 2013, A&A, 558, A33

Bagchi, J., Durret, F., Neto, G. B. L., & Paul, S. 2006, Science, 314, 791

Bagchi, J., Enßlin, T. A., Miniati, F., et al. 2002, New A, 7, 249

Baghmanyan, V., Zargaryan, D., Aharonian, F., et al. 2021, arXiv e-prints, arXiv:2110.00309

Bell, A. R. 1978a, MNRAS, 182, 147

Bell, A. R. 1978b, MNRAS, 182, 443

Benson, B., Wittman, D. M., Golovich, N., et al. 2017, ApJ, 841, 7

Biviano, A. 2000, in Constructing the Universe with Clusters of Galaxies, ed. F. Durret & D. Gerbal, 1

Blandford, R. & Eichler, D. 1987, Phys. Rep., 154, 1
Blandford, R. D. & Ostriker, J. P. 1978, ApJ, 221, L29
Bonafede, A., Brüggen, M., Rafferty, D., et al. 2018, MNRAS, 478, 2927
Bonafede, A., Brunetti, G., Rudnick, L., et al. 2022, arXiv e-prints, arXiv:2203.01958
Bonafede, A., Cassano, R., Brüggen, M., et al. 2017, MNRAS, 470, 3465
Bonafede, A., Giovannini, G., Feretti, L., Govoni, F., & Murgia, M. 2009, A&A, 494, 429
Bonafede, A., Intema, H. T., Brüggen, M., et al. 2014, ApJ, 785, 1
Boschin, W., Girardi, M., & Barrena, R. 2013, MNRAS, 434, 772
Botteon, A., Brunetti, G., van Weeren, R. J., et al. 2020, ApJ, 897, 93
Botteon, A., Gastaldello, F., & Brunetti, G. 2018, MNRAS, 476, 5591
Botteon, A., Gastaldello, F., Brunetti, G., & Kale, R. 2016, MNRAS, 463, 1534
Botteon, A., Shimwell, T. W., Cassano, R., et al. 2022, A&A, 660, A78
Bourdin, H., Mazzotta, P., Markevitch, M., Giacintucci, S., & Brunetti, G. 2013, ApJ, 764, 82
Brown, S., Duesterhoeft, J., & Rudnick, L. 2011, ApJ, 727, L25
Brown, S. & Rudnick, L. 2011, MNRAS, 412, 2
Brunetti, G., Cassano, R., Dolag, K., & Setti, G. 2009, A&A, 507, 661
Brunetti, G. & Jones, T. W. 2014, International Journal of Modern Physics D, 23, 1430007
Brunetti, G. & Lazarian, A. 2007, MNRAS, 378, 245
Brunetti, G. & Lazarian, A. 2011, MNRAS, 410, 127
Brzycki, B. & ZuHone, J. 2019, ApJ, 883, 118
Bulbul, E., Gaspari, M., Alvarez, G., et al. 2019, BAAS, 51, 210
Burns, J. O., Skillman, S. W., & O'Shea, B. W. 2010, ApJ, 721, 1105
Cash, W. 1979, ApJ, 228, 939
Cassano, R., Brunetti, G., & Setti, G. 2006, MNRAS, 369, 1577
Cassano, R., Brunetti, G., Setti, G., Govoni, F., & Dolag, K. 2007, MNRAS, 378, 1565
Cassano, R., Ettori, S., Brunetti, G., et al. 2013, ApJ, 777, 141
Cassano, R., Ettori, S., Giacintucci, S., et al. 2010, ApJ, 721, L82
Cassano, R., Gitti, M., & Brunetti, G. 2008, A&A, 486, L31
Cavaliere, A. & Fusco-Femiano, R. 1976, A&A, 500, 95
Cavaliere, A. & Fusco-Femiano, R. 1978, A&A, 70, 677
Chandran, B. D. G. 2000, Phys. Rev. Lett., 85, 4656
Chibueze, J. O., Akamatsu, H., Parekh, V., et al. 2022, PASJ
Churazov, E., Vikhlinin, A., Zhuravleva, I., et al. 2012, MNRAS, 421, 1123
Clarke, T. E. & Ensslin, T. A. 2006, AJ, 131, 2900
Clavico, S., De Grandi, S., Ghizzardi, S., et al. 2019, A&A, 632, A27
Clowe, D., Bradač, M., Gonzalez, A. H., et al. 2006, ApJ, 648, L109
Cornwell, T. J., Golap, K., & Bhatnagar, S. 2008, IEEE Journal of Selected Topics in

Signal Processing, 2, 647
Cuciti, V., Brunetti, G., van Weeren, R., et al. 2018, A&A, 609, A61
Cuciti, V., Cassano, R., Brunetti, G., et al. 2021, A&A, 647, A51
Cuciti, V., Cassano, R., Brunetti, G., et al. 2015, A&A, 580, A97
Dasadia, S., Sun, M., Morandi, A., et al. 2016, MNRAS, 458, 681
de Gasperin, F., Rudnick, L., Finoguenov, A., et al. 2022, A&A, 659, A146
de Gasperin, F., van Weeren, R. J., Brüggen, M., et al. 2014, MNRAS, 444, 3130
De Luca, A. & Molendi, S. 2004, A&A, 419, 837
de Plaa, J. 2020, spex-xray/pyspextools: Pyspextools 0.3.4
de Plaa, J., Zhuravleva, I., Werner, N., et al. 2012, A&A, 539, A34
Di Gennaro, G., van Weeren, R. J., Andrade-Santos, F., et al. 2019, ApJ, 873, 64
Di Gennaro, G., van Weeren, R. J., Hoeft, M., et al. 2018, ApJ, 865, 24
Di Gennaro, G., van Weeren, R. J., Rudnick, L., et al. 2021, ApJ, 911, 3
Dominguez-Fernandez, P., Bruggen, M., Vazza, F., et al. 2021, MNRAS, 500, 795
Donahue, M., Ettori, S., Rasia, E., et al. 2016, ApJ, 819, 36
Donnert, J., Vazza, F., Brüggen, M., & ZuHone, J. 2018, Space Sci. Rev., 214, 122
Drury, L. O. 1983, Reports on Progress in Physics, 46, 973
Eckert, D., Finoguenov, A., Ghirardini, V., et al. 2020, The Open Journal of Astrophysics, 3, 12
Eckert, D., Gaspari, M., Vazza, F., et al. 2017, ApJ, 843, L29
Eckert, D., Jauzac, M., Vazza, F., et al. 2016, MNRAS, 461, 1302
Ensslin, T. A., Biermann, P. L., Klein, U., & Kohle, S. 1998, A&A, 332, 395
Feretti, L., Giovannini, G., Govoni, F., & Murgia, M. 2012, A&A Rev., 20, 54
Fermi, E. 1949, Physical Review, 75, 1169
Finoguenov, A., Sarazin, C. L., Nakazawa, K., Wik, D. R., & Clarke, T. E. 2010, ApJ, 715, 1143
Fruscione, A., McDowell, J. C., Allen, G. E., et al. 2006, in Society of Photo-Optical Instrumentation Engineers (SPIE) Conference Series, Vol. 6270, Society of Photo-Optical Instrumentation Engineers (SPIE) Conference Series, ed. D. R. Silva & R. E. Doxsey, 62701V
Gaspari, M. & Churazov, E. 2013, A&A, 559, A78
Gaspari, M., Churazov, E., Nagai, D., Lau, E. T., & Zhuravleva, I. 2014, A&A, 569, A67
Gastaldello, F., Marelli, M., Molendi, S., et al. 2022, arXiv e-prints, arXiv:2202.05286
Ghirardini, V., Bahar, E., Bulbul, E., et al. 2021, arXiv e-prints, arXiv:2106.15086
Ghizzardi, S., Rossetti, M., & Molendi, S. 2010, A&A, 516, A32
Giacintucci, S., Markevitch, M., Johnston-Hollitt, M., et al. 2020, ApJ, 891, 1
Gilfanov, M. R., Syunyaev, R. A., & Churazov, E. M. 1987, Soviet Astronomy Letters, 13, 3

Giovannini, G., Bonafede, A., Feretti, L., Govoni, F., & Murgia, M. 2010, A&A, 511, L5
Giovannini, G., Bonafede, A., Feretti, L., et al. 2009, A&A, 507, 1257
Giovannini, G., Feretti, L., Girardi, M., et al. 2011, A&A, 530, L5
Giovannini, G., Tordi, M., & Feretti, L. 1999, New A, 4, 141
Giovannini, G., Vacca, V., Girardi, M., et al. 2013, MNRAS, 435, 518
Gitti, M., Brunetti, G., & Setti, G. 2002, A&A, 386, 456
Gitti, M., Ferrari, C., Domainko, W., Feretti, L., & Schindler, S. 2007, A&A, 470, L25
Golovich, N., Dawson, W. A., Wittman, D. M., et al. 2019a, ApJS, 240, 39
Golovich, N., Dawson, W. A., Wittman, D. M., et al. 2019b, ApJ, 882, 69
Govoni, F., Enßlin, T. A., Feretti, L., & Giovannini, G. 2001, A&A, 369, 441
Govoni, F., Murgia, M., Markevitch, M., et al. 2009, A&A, 499, 371
Gu, L., Zhuravleva, I., Churazov, E., et al. 2018, Space Sci. Rev., 214, 108
Gunn, J. E. & Gott, J. Richard, I. 1972, ApJ, 176, 1
Hales, S. E. G., Waldram, E. M., Rees, N., & Warner, P. J. 1995, MNRAS, 274, 447
Hallman, E. J. & Markevitch, M. 2004, ApJ, 610, L81
Henry, J. P., Evrard, A. E., Hoekstra, H., Babul, A., & Mahdavi, A. 2009, ApJ, 691, 1307
Herschel, W. 1785, Philosophical Transactions of the Royal Society of London Series I, 75, 213
Hickox, R. C. & Markevitch, M. 2006, ApJ, 645, 95
Hitomi Collaboration, Aharonian, F., Akamatsu, H., et al. 2016, Nature, 535, 117
Hoang, D. N., Shimwell, T. W., Stroe, A., et al. 2017, MNRAS, 471, 1107
Hoang, D. N., Shimwell, T. W., van Weeren, R. J., et al. 2019, A&A, 622, A20
Hoang, D. N., Zhang, X., Stuardi, C., et al. 2021, A&A, 656, A154
Hong, S. E., Kang, H., & Ryu, D. 2015, ApJ, 812, 49
Hoshino, A., Henry, J. P., Sato, K., et al. 2010, PASJ, 62, 371
Hubble, E. P. 1929, ApJ, 69, 103
Hudson, D. S., Mittal, R., Reiprich, T. H., et al. 2010, A&A, 513, A37
Ichinohe, Y., Simionescu, A., Werner, N., Markevitch, M., & Wang, Q. H. S. 2021, MNRAS, 504, 2800
Ichinohe, Y., Simionescu, A., Werner, N., & Takahashi, T. 2017, MNRAS, 467, 3662
Ichinohe, Y., Werner, N., Simionescu, A., et al. 2015, MNRAS, 448, 2971
Intema, H. T. 2014, in Astronomical Society of India Conference Series, Vol. 13, Astronomical Society of India Conference Series, 469
Intema, H. T., van der Tol, S., Cotton, W. D., et al. 2009, A&A, 501, 1185
Ishisaki, Y., Maeda, Y., Fujimoto, R., et al. 2007, PASJ, 59, 113
Jaffe, W. J. 1977, ApJ, 212, 1
Jones, F. C. & Ellison, D. C. 1991, Space Sci. Rev., 58, 259
Kaastra, J. S. 2017, A&A, 605, A51

Kaastra, J. S. & Bleeker, J. A. M. 2016, A&A, 587, A151
Kaastra, J. S., Mewe, R., & Nieuwenhuijzen, H. 1996, in UV and X-ray Spectroscopy of Astrophysical and Laboratory Plasmas, 411–414
Kaastra, J. S., Paerels, F. B. S., Durret, F., Schindler, S., & Richter, P. 2008, Space Sci. Rev., 134, 155
Kaastra, J. S., Raassen, A. J. J., de Plaa, J., & Gu, L. 2018a, SPEX X-ray spectral fitting package
Kaastra, J. S., Raassen, A. J. J., de Plaa, J., & Gu, L. 2018b, SPEX X-ray spectral fitting package. Zenodo. https://doi.org/10.5281/zenodo.2419563
Kaastra, J. S., Raassen, A. J. J., de Plaa, J., & Gu, L. 2020a, SPEX X-ray spectral fitting package
Kaastra, J. S., Raassen, A. J. J., de Plaa, J., & Gu, L. 2020b, SPEX X-ray spectral fitting package (https://doi.org/10.5281/zenodo.3939056)
Kale, R. & Dwarakanath, K. S. 2010, ApJ, 718, 939
Kale, R., Venturi, T., Giacintucci, S., et al. 2015, A&A, 579, A92
Kang, H. 2015, Journal of Korean Astronomical Society, 48, 9
Kang, H. & Jones, T. W. 2002, Journal of Korean Astronomical Society, 35, 159
Kang, H. & Jones, T. W. 2005, ApJ, 620, 44
Kang, H., Jones, T. W., & Gieseler, U. D. J. 2002, ApJ, 579, 337
Kang, H. & Ryu, D. 2011, ApJ, 734, 18
Kang, H., Ryu, D., & Jones, T. W. 2012, ApJ, 756, 97
Kardashev, N. S. 1962, Soviet Ast., 6, 317
Kempner, J. C. & Sarazin, C. L. 2001, ApJ, 548, 639
Kettula, K., Nevalainen, J., & Miller, E. D. 2013, A&A, 552, A47
Kraft, R. P., Roediger, E., Machacek, M., et al. 2017, ApJ, 848, 27
Kravtsov, A. V. & Borgani, S. 2012, ARA&A, 50, 353
Krymskii, G. F. 1977, Akademiia Nauk SSSR Doklady, 234, 1306
Kuntz, K. D. & Snowden, S. L. 2000, ApJ, 543, 195
Kuntz, K. D. & Snowden, S. L. 2008, A&A, 478, 575
Landau, L. D. & Lifshitz, E. M. 1959, Fluid mechanics
Lehmer, B. D., Xue, Y. Q., Brandt, W. N., et al. 2012, ApJ, 752, 46
Lodders, K., Palme, H., & Gail, H.-P. 2009, 4.4 Abundances of the elements in the Solar System: Datasheet from Landolt-Börnstein - Group VI Astronomy and Astrophysics · Volume 4B: "Solar System" in SpringerMaterials (https://doi.org/10.1007/978-3-540-88055-4_34)
Lodders, K., Palme, H., & Gail, H. P. 2009, Landolt Börnstein, 4B, 712
Lovisari, L., Forman, W. R., Jones, C., et al. 2017, ApJ, 846, 51
Lovisari, L., Reiprich, T. H., & Schellenberger, G. 2015, A&A, 573, A118
Machacek, M., Jones, C., Forman, W. R., & Nulsen, P. 2006, ApJ, 644, 155
Macquorn Rankine, W. J. 1870, Philosophical Transactions of the Royal Society of London Series I, 160, 277

Mantz, A. B., Allen, S. W., Morris, R. G., et al. 2016, MNRAS, 463, 3582
Marelli, M., Molendi, S., Rossetti, M., et al. 2021, ApJ, 908, 37
Markevitch, M. 2006, in ESA Special Publication, Vol. 604, The X-ray Universe 2005, ed. A. Wilson, 723
Markevitch, M., Gonzalez, A. H., David, L., et al. 2002, ApJ, 567, L27
Markevitch, M., Govoni, F., Brunetti, G., & Jerius, D. 2005, ApJ, 627, 733
Markevitch, M., Mazzotta, P., Vikhlinin, A., et al. 2003, ApJ, 586, L19
Markevitch, M. & Vikhlinin, A. 2007, Phys. Rep., 443, 1
Markevitch, M., Vikhlinin, A., & Mazzotta, P. 2001, ApJ, 562, L153
Melville, S., Schekochihin, A. A., & Kunz, M. W. 2016, MNRAS, 459, 2701
Menanteau, F., Hughes, J. P., Sifón, C., et al. 2012, ApJ, 748, 7
Mernier, F., de Plaa, J., Lovisari, L., et al. 2015, A&A, 575, A37
Messier, C. 1781, Catalogue des Nébuleuses et des Amas d'Étoiles (Catalog of Nebulae and Star Clusters), Connoissance des Temps ou des Mouvements Célestes
Miniati, F., Ryu, D., Kang, H., et al. 2000, ApJ, 542, 608
Mohr, J. J., Fabricant, D. G., & Geller, M. J. 1993, ApJ, 413, 492
Monteiro-Oliveira, R., Cypriano, E. S., Machado, R. E. G., et al. 2017, MNRAS, 466, 2614
Nelson, K., Lau, E. T., Nagai, D., Rudd, D. H., & Yu, L. 2014, ApJ, 782, 107
Nurgaliev, D., McDonald, M., Benson, B. A., et al. 2013, ApJ, 779, 112
Ogrean, G. A., Brüggen, M., van Weeren, R. J., Burgmeier, A., & Simionescu, A. 2014, MNRAS, 443, 2463
Owers, M. S., Nulsen, P. E. J., Couch, W. J., & Markevitch, M. 2009, ApJ, 704, 1349
Pearce, C. J. J., van Weeren, R. J., Andrade-Santos, F., et al. 2017, ApJ, 845, 81
Perley, R. A. & Butler, B. J. 2013, ApJS, 204, 19
Pinto, C., Fabian, A. C., Ogorzalek, A., et al. 2016, MNRAS, 461, 2077
Pinzke, A., Oh, S. P., & Pfrommer, C. 2013, MNRAS, 435, 1061
Planck Collaboration, Ade, P. A. R., Aghanim, N., et al. 2013, A&A, 554, A140
Planck Collaboration, Ade, P. A. R., Aghanim, N., et al. 2016, A&A, 594, A27
Poole, G. B., Fardal, M. A., Babul, A., et al. 2006, MNRAS, 373, 881
Pratt, G. W., Croston, J. H., Arnaud, M., & Böhringer, H. 2009, A&A, 498, 361
Rajpurohit, K., Hoeft, M., van Weeren, R. J., et al. 2018, ApJ, 852, 65
Rajpurohit, K., Hoeft, M., Vazza, F., et al. 2020, A&A, 636, A30
Rajpurohit, K., van Weeren, R. J., Hoeft, M., et al. 2022, ApJ, 927, 80
Rajpurohit, K., Vazza, F., van Weeren, R. J., et al. 2021, A&A, 654, A41
Rau, U. & Cornwell, T. J. 2011, A&A, 532, A71
Reiprich, T. H., Basu, K., Ettori, S., et al. 2013, Space Sci. Rev., 177, 195
Rengelink, R. B., Tang, Y., de Bruyn, A. G., et al. 1997, A&AS, 124, 259
Roediger, E., Kraft, R. P., Machacek, M. E., et al. 2012, ApJ, 754, 147

Roncarelli, M., Gaspari, M., Ettori, S., et al. 2018, A&A, 618, A39
Rosen, S. R., Webb, N. A., Watson, M. G., et al. 2016, A&A, 590, A1
Rottgering, H. J. A., Wieringa, M. H., Hunstead, R. W., & Ekers, R. D. 1997, MNRAS, 290, 577
Rudnick, L., Delain, K. M., & Lemmerman, J. A. 2006, Astronomische Nachrichten, 327, 549
Russell, H. R., McNamara, B. R., Sanders, J. S., et al. 2012, MNRAS, 423, 236
Russell, H. R., Sanders, J. S., Fabian, A. C., et al. 2010, MNRAS, 406, 1721
Sabol, E. J. & Snowden, S. L. 2019, sxrbg: ROSAT X-Ray Background Tool
Sanders, J. S. 2006, MNRAS, 371, 829
Santos, J. S., Rosati, P., Tozzi, P., et al. 2008, A&A, 483, 35
Sarazin, C. L. 1988, X-ray emission from clusters of galaxies
Sarazin, C. L. 2002, in Astrophysics and Space Science Library, Vol. 272, Merging Processes in Galaxy Clusters, ed. L. Feretti, I. M. Gioia, & G. Giovannini, 1–38
Schaal, K., Springel, V., Pakmor, R., et al. 2016, MNRAS, 461, 4441
Schekochihin, A. A. & Cowley, S. C. 2006, Physics of Plasmas, 13, 056501
Schellenberger, G., Reiprich, T. H., Lovisari, L., Nevalainen, J., & David, L. 2015, A&A, 575, A30
Schreier, S. 1982, Compressible Flow, A Wiley-Interscience publication (Wiley)
Sekiya, N., Yamasaki, N. Y., Mitsuda, K., & Takei, Y. 2014, PASJ, 66, L3
Serlemitsos, P. J., Soong, Y., Chan, K.-W., et al. 2007, PASJ, 59, S9
Shimwell, T. W., Brown, S., Feain, I. J., et al. 2014, MNRAS, 440, 2901
Shimwell, T. W., Hardcastle, M. J., Tasse, C., et al. 2022, A&A, 659, A1
Shimwell, T. W., Luckin, J., Brüggen, M., et al. 2016, MNRAS, 459, 277
Shimwell, T. W., Röttgering, H. J. A., Best, P. N., et al. 2017, A&A, 598, A104
Simionescu, A., Werner, N., Forman, W. R., et al. 2010, MNRAS, 405, 91
Simionescu, A., ZuHone, J., Zhuravleva, I., et al. 2019, Space Sci. Rev., 215, 24
Skillman, S. W., Xu, H., Hallman, E. J., et al. 2013, ApJ, 765, 21
Snowden, S. L., Egger, R., Finkbeiner, D. P., Freyberg, M. J., & Plucinsky, P. P. 1998, ApJ, 493, 715
Spitzer, L. 1956, Physics of Fully Ionized Gases
Sreenivasan, K. R. 1995, Physics of Fluids, 7, 2778
Stroe, A., Shimwell, T., Rumsey, C., et al. 2016, MNRAS, 455, 2402
Stroe, A., van Weeren, R. J., Intema, H. T., et al. 2013, A&A, 555, A110
Sun, M., Jones, C., Forman, W., et al. 2006, ApJ, 637, L81
Sunyaev, R. A. & Zeldovich, Y. B. 1972, Comments on Astrophysics and Space Physics, 4, 173
Tawa, N., Hayashida, K., Nagai, M., et al. 2008, PASJ, 60, S11
Tittley, E. R. & Henriksen, M. 2005, ApJ, 618, 227
Urdampilleta, I., Akamatsu, H., Mernier, F., et al. 2018, A&A, 618, A74

van Weeren, R. J., Andrade-Santos, F., Dawson, W. A., et al. 2017, Nature Astronomy, 1, 0005
van Weeren, R. J., Brunetti, G., Brüggen, M., et al. 2016a, ApJ, 818, 204
van Weeren, R. J., de Gasperin, F., Akamatsu, H., et al. 2019, Space Sci. Rev., 215, 16
van Weeren, R. J., Fogarty, K., Jones, C., et al. 2013, ApJ, 769, 101
van Weeren, R. J., Ogrean, G. A., Jones, C., et al. 2016b, ApJ, 817, 98
van Weeren, R. J., Röttgering, H. J. A., Bagchi, J., et al. 2009, A&A, 506, 1083
van Weeren, R. J., Röttgering, H. J. A., Brüggen, M., & Hoeft, M. 2010, Science, 330, 347
van Weeren, R. J., Röttgering, H. J. A., Rafferty, D. A., et al. 2012, A&A, 543, A43
Vazza, F., Brunetti, G., Kritsuk, A., et al. 2009, A&A, 504, 33
Vazza, F., Jones, T. W., Brüggen, M., et al. 2017, MNRAS, 464, 210
Vikhlinin, A., Markevitch, M., & Murray, S. S. 2001, ApJ, 551, 160
Voit, G. M., Bryan, G. L., Balogh, M. L., & Bower, R. G. 2002, ApJ, 576, 601
Wang, Q. H. S. & Markevitch, M. 2018, ApJ, 868, 45
Wang, Q. H. S., Markevitch, M., & Giacintucci, S. 2016a, ApJ, 833, 99
Wang, S., Liu, J., Qiu, Y., et al. 2016b, ApJS, 224, 40
Wen, Z. L., Han, J. L., & Liu, F. S. 2012, ApJS, 199, 34
Werner, N., Zhuravleva, I., Churazov, E., et al. 2009, MNRAS, 398, 23
Werner, N., ZuHone, J. A., Zhuravleva, I., et al. 2016, MNRAS, 455, 846
Willingale, R., Starling, R. L. C., Beardmore, A. P., Tanvir, N. R., & O'Brien, P. T. 2013, MNRAS, 431, 394
Wolter, H. 1952, Annalen der Physik, 445, 286
Xi, S.-Q., Wang, X.-Y., Liang, Y.-F., et al. 2018, Phys. Rev. D, 98, 063006
Xu, H., Kahn, S. M., Peterson, J. R., et al. 2002, ApJ, 579, 600
Yoshino, T., Mitsuda, K., Yamasaki, N. Y., et al. 2009, PASJ, 61, 805
Yu, H., Tozzi, P., Borgani, S., Rosati, P., & Zhu, Z. H. 2011, A&A, 529, A65
Yuan, Z. S. & Han, J. L. 2020, MNRAS, 497, 5485
Yuan, Z. S., Han, J. L., & Wen, Z. L. 2015, ApJ, 813, 77
Zhang, C., Churazov, E., Forman, W. R., & Jones, C. 2019a, MNRAS, 482, 20
Zhang, C., Churazov, E., Forman, W. R., & Lyskova, N. 2019b, MNRAS, 488, 5259
Zhang, X. 2021, Sbfit 0.2.0
Zhang, X., Simionescu, A., Akamatsu, H., et al. 2020, A&A, 642, A89
Zhuravleva, I., Churazov, E., Arévalo, P., et al. 2015, MNRAS, 450, 4184
Zhuravleva, I., Churazov, E., Kravtsov, A., & Sunyaev, R. 2012, MNRAS, 422, 2712
Zhuravleva, I., Churazov, E., Schekochihin, A. A., et al. 2014a, Nature, 515, 85
Zhuravleva, I., Churazov, E., Schekochihin, A. A., et al. 2019, Nature Astronomy, 3, 832
Zhuravleva, I., Churazov, E. M., Schekochihin, A. A., et al. 2014b, ApJ, 788, L13

ZuHone, J. & Su, Y. 2022, arXiv e-prints, arXiv:2202.06712
ZuHone, J. A. 2011, ApJ, 728, 54
ZuHone, J. A., Markevitch, M., Brunetti, G., & Giacintucci, S. 2013, ApJ, 762, 78
ZuHone, J. A., Markevitch, M., & Lee, D. 2011, ApJ, 743, 16
ZuHone, J. A., Markevitch, M., Weinberger, R., Nulsen, P., & Ehlert, K. 2021, ApJ, 914, 73
ZuHone, J. A., Markevitch, M., & Zhuravleva, I. 2016, ApJ, 817, 110
Zuhone, J. A. & Roediger, E. 2016, Journal of Plasma Physics, 82, 535820301
Zwicky, F. 1933, Helvetica Physica Acta, 6, 110

Nederlandse Samenvatting

Clusters van sterrenstelsels zijn knooppunten van het Kosmische Web en zijn de grootste gevirialiseerde *halo's* in het heelal, met massa's van ongeveer $10^{14} - 10^{15}\ M_{\odot}$. Naast de vijf zesde van de massa die in de vorm van donkere materie is bedraagt het intracluster medium (ICM), die de enorme ruimte tussen de sterrenstelsels doordringt, het grootste deel van de resterende één zesde aan baryonische inhoud. De gasvormige clusteratmosfeer is extreem ijl en heet. De getalsdichtheid van het ICM is $< 10^{-2}$ cm^{-3}, wat veel lager is dan is bereikt in het beste vacuümlab op aarde. De temperatuur kan oplopen tot 10^{8} K, wat betekent dat zware elementen zoals Fe worden geïoniseerd tot H- en He-achtige ionen. Ondertussen is de intraclusterruimte turbulent en spelen clusterfusies een sleutelrol bij het stimuleren van de gasbewegingen. Deze gasbewegingen leiden tot grootschalige dichtheidsdiscontinuïteiten in de vorm van koude fronten en schokgolven, en thermodynamische fluctuaties als gevolg van turbulente bewegingen.

Op radiofrequenties is gevonden dat clusters van sterrenstelsels, vooral samensmeltende clusters, uitgebreide synchrotronbronnen herbergen die groottes van een Mpc kunnen bereiken en worden gekenmerkt door steile spectra. Op basis van de morfologie en radio-eigenschappen worden deze bronnen geclassificeerd als radiorelikwieën en radiohalo's. Het onderzoeken van deeltjesversnellingsmechanismen in het ICM is de sleutel om de oorsprong van deze uitgebreide clusterradiobronnen te onthullen. De twee algemeen aanvaarde versnellingsmechanismen voor radiorelikwieën en radiohalo's zijn respectievelijk schokversnelling en turbulente versnelling. Beide scenario's zijn het gevolg van ICM bewegingen. Daarom zijn röntgenwaarnemingen van het ICM belangrijk voor het kwantificeren van schokgolf- en turbulentie-eigenschappen om de versnellingsmodellen te testen.

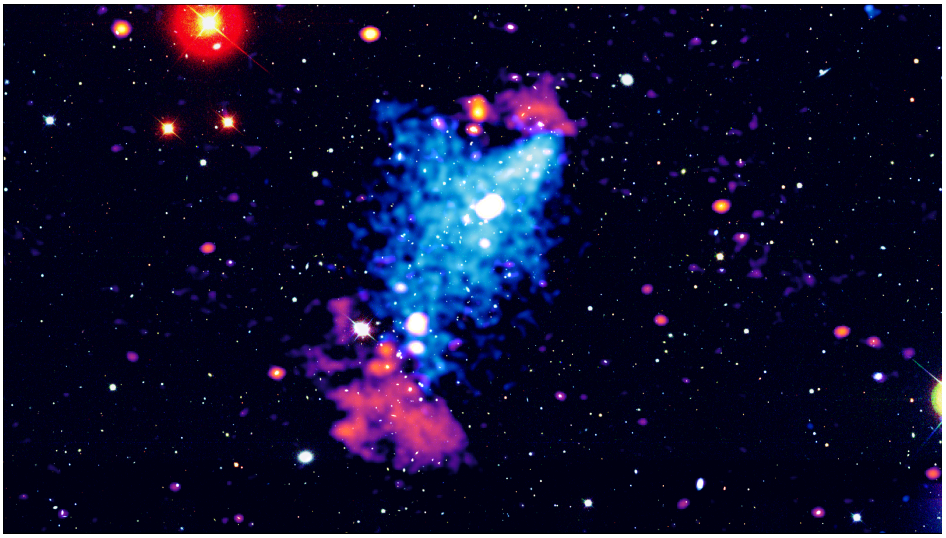

Figuur A.1: Samensmeltend cluster ZwCl 2341+0000, met twee radiorelikwieën aan weerszijden.

De eigenschappen van schokgolven kunnen worden gekwantificeerd op basis van de Rankine-Hugoniot-conditie door de stroomopwaartse en de stroomafwaartse thermodynamische eigenschappen te meten. De turbulente snelheidsdispersie kan worden geschat door de amplitude van de dichtheidsfluctuatie te meten of in de nabije toekomst aan de hand van lijnverschuivingen en lijnbreedtes in spectra van hoge resolutie.

Dit proefschrift

Dit proefschrift richt zich op röntgenwaarnemingen van clusters van sterrenstelsels. Het hoofddoel is om de verbanden tussen röntgen- en radioverschijnselen vast te stellen en verder te onderzoeken.

1. Het verband tussen schokgolven en radiorelikwieën

   In **Hoofdstukken 2** en **3** heben we diepe röntgenwaarnemingen geanalyseerd van twee samensmeltende clusters, respectievelijk Abell 3411-3412 en ZwCl 2341+0000. De diepe waarnemingen onthullen de thermodynamische structuur van het ICM rond radiorelikwieën en illustreren dat zowel schokgolven als koude fronten ruimtelijk kun-

nen overlappen met radiorelikwie-emissie. Onder hen bevinden de geprojecteerde posities van schokgolven zich dicht bij de buitenranden van radiorelikwieën, wat het scenario voor schokversnelling ondersteunt.

Als we de resultaten vergelijken tussen de diepe en voorheen gepubliceerde ondiepe waarnemingen, is een cruciale boodschap dat schokgolven kunnen worden verward met koude fronten op basis van de vergelijkbare kenmerken van sprongen in oppervlaktehelderheid. Om de aard van een oppervlaktehelderheidssprong als schokgolf te bevestigen is röntgenspectrale analyse nodig op basis van thermodynamische eigenschappen die verschillen met die van die van koude fronten.

2. Het verband tussen schokgolven en radiohalo's

   Hoofdstuk 4 meldt twee sprongen in de oppervlaktehelderheid van de röntgenstraling op de locatie van de radiohalo rand in het cluster ClG 0217+70. Dit zijn nieuwe kandidaten voor associatie tussen de schokgolf en de radiohalo, als deze schokgolven worden bevestigd door de komende diepe röntgenwaarnemingen. Deze ontdekking en een handvol eerder gemelde gevallen suggereren dat schokgolven ook een rol kunnen spelen bij het vormen van radiohalo's.

3. Het verband tussen het vermogen van radiohalo's en de sterkte van turbulentie

   In **Hoofdstuk 5** onderzoeken we de relatie tussen het vermogen van radiohalo's en eigenschappen van turbulentie in het ICM met behulp van het monster in de tweede gegevensvrijgave van de LOFAR Two-metre Sky Survey. Het Mach-getal van turbulentie wordt geschat door het vermogensspectrum van fluctuaties in de oppervlaktehelderheid van röntgenstraling te berekenen, wat blijkt te zijn gecorreleerd met de dynamische toestand van het cluster. Bovendien, door de turbulente dissipatieflux te berekenen, vinden we dat deze gecorreleerd is met het vermogen van radiohalo's met een regressiehelling van ongeveer één, wat een onderliggend verband suggereert tussen deeltjesversnelling en de turbulente bewegingen van het ICM.

Naast het beperken van de eigenschappen van de grootste deeltjesversnellers in het heelal, behandelt dit proefschrift diverse onderwerpen over

röntgenwaarnemingen van clusters van sterrenstelsels. In **Hoofdstuk 2** en **5** ontwikkellen we methoden voor het modelleren van de gefocuste en ongefocuste niet-röntgenachtergrond voor de *XMM-Newton* EPIC beeldvormingsspectrometer, die de systematische onzekerheid voor data-analyse in achtergrond-gedomineerde regio's reduceren. In **Hoofdstuk 3** ontdekken we een uniek kegelachtig restant van een kern in het samensmeltende cluster ZwCl 2341+0000, wat een korte overgangsfase van de kernrest in een frontale samenvoeging impliceert. **Hoofdstuk 4** illustreert de kracht van röntgenspectroscopie bij het meten van de roodverschuiving van een cluster van sterrenstelsels achter het Galactische vlak, waarvan de optische gegevens te lijden hebben onder systematische onzekerheden als gevolg van extinctie.

English Summary

Galaxy clusters are nodes of the Cosmic Web, and are the largest virialized *halos* in the Universe, with masses of about $10^{14} - 10^{15}\ M_{\odot}$. Beside the five sixths of the mass content that is in the form of dark matter, the intracluster medium (ICM) permeating the vast space between the member galaxies amounts for most of the remaining one sixth baryonic content. The gaseous cluster atmosphere is extremely tenuous and hot. The number density of the ICM is $< 10^{-2}$ cm^{-3}, which is much lower than achieved in the best vacuum lab on Earth. The temperature can reach 10^{8} K, meaning that heavy elements such as Fe are ionized to H- and He-like ions. Meanwhile, the intracluster space is turbulent, and cluster mergers play a key role in stimulating the gas motions. These gas motions lead to large scale density discontinuities in the forms of cold fronts and shock waves, and thermodynamic fluctuations due to turbulent motions.

At radio frequencies, galaxy clusters, especially merging clusters have been found to host extended synchrotron sources, which have scales up to a Mpc and are characterized by steep spectra. Based on radio properties such as morphology and polarization, these sources are classified as radio relics and radio halos. Investigating particle acceleration mechanisms in the ICM is the key to unveil the origin of these extended cluster radio sources. The two widely accepted acceleration mechanisms for radio relics and radio halos are shock acceleration and turbulent acceleration, respectively. Both of these scenarios are due to ICM motions. Therefore, X-ray observations of the ICM are important for quantifying shock wave and turbulence properties to test the acceleration models. The properties of shock waves can be quantified based on Rankine-Hugoniot condition by measuring the upstream and downstream thermodynamic properties.

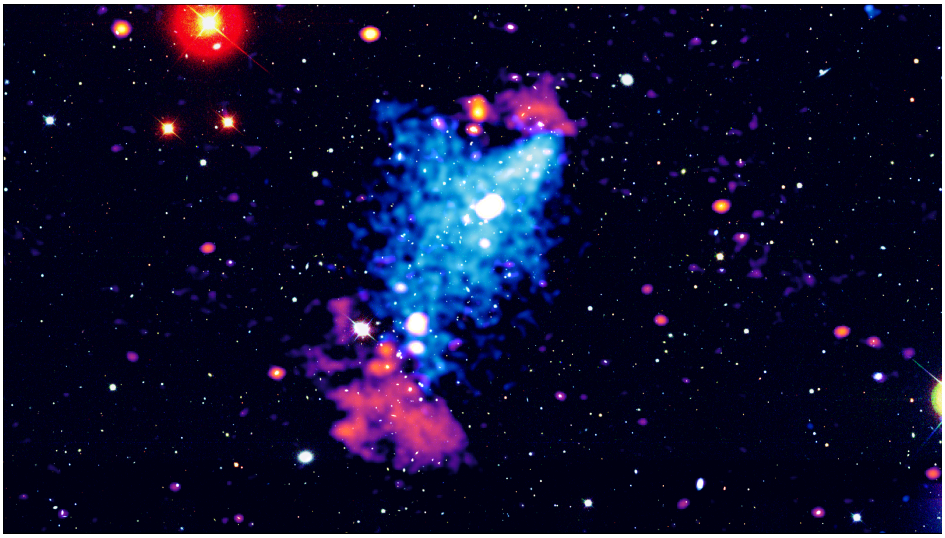

Figure B.1: Merging galaxy cluster ZwCl 2341+0000, which hosts two radio relics on the opposite sides.

The turbulent velocity dispersion can be estimated by measuring the density fluctuation amplitude or in the near future by line shifts and widths of high resolution spectra.

This thesis

This thesis focuses on X-ray observations of galaxy clusters. The main goal is to establish and further explore and the connections between X-ray and radio phenomena.

1. The connection between shocks and radio relics

   In **Chapters 2** and **3**, we analyzed deep X-ray observations of two merging clusters, Abell 3411-3412 and ZwCl 2341+0000. The deep observations reveal the ICM thermodynamic structure around radio relics and illustrate that both shock waves and cold fronts could spatially overlap with radio relic emission. Among them, the projected positions of shock waves are close to the outer edges of radio relics, which supports the shock acceleration scenario.

Comparing the results between the deep and previously published shallow observations, one crucial message is that shock waves could be confused with cold fronts based on the similar features of surface brightness jumps. X-ray spectral analysis is necessary to confirm the shock wave nature of a surface brightness jump based on its thermodynamic properties that are distinct from those of cold fronts.

2. The connection between shocks and radio halo edges

   Chapter 4 reports two X-ray surface brightness jumps at the location of the radio halo edge in galaxy cluster ClG 0217+70. These are new candidates of shock wave - radio halo association, if their shock wave nature is confirmed by the upcoming deep X-ray observations. This discovery as well as a handful of previously reported cases suggest that shock waves may also play a role in shaping radio halos.

3. The connection between turbulence strength and radio halo power

   In **Chapter 5**, we investigate the relation between radio halo power and properties of ICM turbulence using the sample in the second data release of the LOFAR Two-metre Sky Survey. The Mach number of turbulence is estimated by calculating the power spectrum of X-ray surface brightness fluctuations, which is found to be correlated with the cluster dynamic state. Moreover, by calculating the turbulent dissipation flux, we find it is correlated with radio halo power with a regression slope close to unity, suggesting an underlying connection between particle acceleration and the ICM turbulent motions.

In addition to constraining the properties of the largest particle accelerators in the Universe, this thesis addresses diverse topics on X-ray observations of galaxy clusters. In **Chapter 2** and **5**, we develop methods for modeling the focused and unfocused non X-ray background for the *XMM-Newton* EPIC imaging spectrometer, which reduce the systematic uncertainty for data analysis in background dominated regions. In **Chapter 3**, we discover a unique cone-like core remnant in the merging cluster ZwCl 2341+0000, which implies a short transition stage of the core remnant in a head-on merger. **Chapter 4** illustrates the power of X-ray spectroscopy on measuring the redshift of a galaxy cluster behind the Galactic plane, whose optical data suffers from systematic uncertainties due to extinction.

List of publications

First-author publications

1. **Zhang, X.**, Simionescu, A., Akamatsu, H., Kaastra, J. S., de Plaa, J., & van Weeren, R. J. (2020), A&A, 642, A89.

2. **Zhang, X.**, Simionescu, A., Kaastra, J. S., Akamatsu, H., Hoang, D. N., Stuardi, C., van Weeren, R. J., Rudnick, L., Kraft, R. P., & Brown, S. (2020), A&A, 642, L3.

3. **Zhang, X.**, Simionescu, A., Stuardi, C., van Weeren, R. J., Intema, H. T., Akamatsu, H., de Plaa, J., Kaastra, J. S., Bonafede, A., Brüggen, M., ZuHone, J., & Ichinohe, Y. (2021), A&A, 656, A59.

4. **Zhang, X.**, Simionescu, A., Gastaldello, F., Eckert D., Camillini, L., Natale, R., Akamatsu, H., Botteon, A., Cassano, R., Cuciti, V., Bruno, L., Shimwell, T.W., & Kaastra, J.S. (2022), to be submitted.

Co-author publications

1. Hoang, D. N., **Zhang, X.**, Stuardi, C., Shimwell, T. W., Bonafede, A., Brüggen, M., Brunetti, G., Botteon, A., Cassano, R., de Gasperin, F., Di Gennaro, G., Hoeft, M., Intema, H., Rajpurohit, K., Röttgering, H. J. A., Simionescu, A., & van Weeren, R. J. (2021), A&A, 656, A154.

2. Botteon, A., Shimwell, T. W., Cassano, R., Cuciti, V., **Zhang, X.**, Bruno, L., Camillini, L., Natale, R., Jones, A., Gastaldello, F., Simionescu, A., Rossetti, M., Akamatsu, H., van Weeren, R. J., Brunetti, G., Brüggen,

M., Groeneveld, C., Hoang, D. N., Hardcastle, M. J., Ignesti, A., Di Gennaro, G., Bonafede, A., Drabent, A., Röttgering, H. J. A., Hoeft, M., & de Gasperin, F. (2022), A&A, 660, A78.

3. Urdampilleta, I., Simionescu, A., Kaastra, J. S., **Zhang, X.**, Di Gennaro, G., Mernier, F., de Plaa, J., & Brunetti, G. (2021), A&A, 646, A95.

4. Zhu, Z., Simionescu, A., Akamatsu, H., **Zhang, X.**, Kaastra, J. S., de Plaa, J., Urban, O., Allen, S. W., & Werner, N. (2021), A&A, 652, A147.

5. Shimwell, T. W., Hardcastle, M. J., Tasse, C., Best, P. N., Röttgering, H. J. A., Williams, W. L., Botteon, A., Drabent, A., Mechev, A., Shulevski, A., van Weeren, R. J., Bester, L., Brüggen, M., Brunetti, G., Callingham, J. R., Chyży, K. T., Conway, J. E., Dijkema, T. J., Duncan, K., de Gasperin, F., Hale, C. L., Haverkorn, M., Hugo, B., Jackson, N., Mevius, M., Miley, G. K., Morabito, L. K., Morganti, R., Offringa, A., Oonk, J. B. R., Rafferty, D., Sabater, J., Smith, D. J. B., Schwarz, D. J., Smirnov, O., O'Sullivan, S. P., Vedantham, H., White, G. J., Albert, J. G., Alegre, L., Asabere, B., Bacon, D. J., Bonafede, A., Bonnassieux, E., Brienza, M., Bilicki, M., Bonato, M., Calistro Rivera, G., Cassano, R., Cochrane, R., Croston, J. H., Cuciti, V., Dallacasa, D., Danezi, A., Dettmar, R. J., Di Gennaro, G., Edler, H. W., Enßlin, T. A., Emig, K. L., Franzen, T. M. O., García-Vergara, C., Grange, Y. G., Gürkan, G., Hajduk, M., Heald, G., Heesen, V., Hoang, D. N., Hoeft, M., Horellou, C., Iacobelli, M., Jamrozy, M., Jelić, V., Kondapally, R., Kukreti, P., Kunert-Bajraszewska, M., Magliocchetti, M., Mahatma, V., Małek, K., Mandal, S., Massaro, F., Meyer-Zhao, Z., Mingo, B., Mostert, R. I. J., Nair, D. G., Nakoneczny, S. J., Nikiel-Wroczyński, B., Orrú, E., Pajdosz-Śmierciak, U., Pasini, T., Prandoni, I., van Piggelen, H. E., Rajpurohit, K., Retana-Montenegro, E., Riseley, C. J., Rowlinson, A., Saxena, A., Schrijvers, C., Sweijen, F., Siewert, T. M., Timmerman, R., Vaccari, M., Vink, J., West, J. L., Wołowska, A., **Zhang, X.**, & Zheng, J. (2022), A&A, 659, A1.

6. Bonafede, A., Brunetti, G., Rudnick, L., Vazza, F., Bourdin, H., Giovannini, G., Shimwell, T. W., **Zhang, X.**, Mazzotta, P., Simionescu, A., Biava, N., Bonnassieux, E., Brienza, M., Brüggen, M., Rajpurohit, K., Riseley, C. J., Stuardi, C., Feretti, L., Tasse, C., Botteon, A., Carretti, E., Cassano, R., Cuciti, V., de Gasperin, F., Gastaldello, F., Rossetti, M.,

Rottgering, H. J. A., Venturi, T., & van Weeren, R. J. (2022), Accepted for publication in ApJ, arXiv e-prints, arXiv:2203.01958.

Other publications

1. Li, T., Wu, J.-H., Meng, N.-K., Dai, Y., & **Zhang, X.-Y.** (2021), Research in Astronomy and Astrophysics, 21, 259.

2. Dai, Y., Fang, Y., **Zhang, X.**, Meng, N., Wu, J., & Zhu, Z.-H. (2021), MNRAS, 507, 455.

Curriculum Vitae

I was born in Zhenhai, Ningbo, China, on October 11, 1992. Zhenhai is a seaside town 20 kilometers south of the city center. I lived there for the first 18 years of my life before moving to Beijing to study in 2011.

I was admitted by Beijing Normal University (BNU) where I joined the Department of Astronomy. Honestly, astronomy was not my first choice at the age of 18, but it was my childhood dream. I spent seven years at BNU for the Bachelor and Master degrees. Under the supervision of Prof. Jianghua Wu, who later became my Master supervisor, I began my first research project in 2013 on analyzing optical data of blazars. During my Master program, I continued the research on blazar variability and involved more on observations. Over the three years, I spent many nights at Xinglong Station operating telescopes. In addition to my thesis research, in 2014, I completed two summer intern projects. One is for stellar spectra classification with Prof. Jifeng Liu at the National Astronomical Observatories of China. Another one is for quasar variability search using *GALEX* archival data with Prof. Minfeng Gu at Shanghai Astronomical Observatory.

I had the opportunity to gain international experience during my seven years at BNU, with short trips to Perth, Australia in 2012 and Turku, Finland in 2016. In Perth, I spent a few days in ICRAR learning basic radio astronomy. In Turku, I worked for three weeks in Tuorla Observatory on the *Swift* spectra of AGNs. It was my first time learning X-ray spectroscopy, though the nonthermal spectra of point sources are very different from what I am currently doing on galaxy clusters. Honestly, these short visits are still insufficient for gaining international experience and establishing international collaborations. For this reason, I was motivated to pursue

my PhD abroad.

I started my PhD program in 2018 at Leiden University and SRON on the topic of merging galaxy clusters supervised by Prof.dr. Jelle Kaastra and Dr. Aurora Simionescu. My PhD research is X-ray focused but includes a lot of radio data, for which I receive great help from Dr. Reinout van Weeren. During my PhD, I have opportunities to collaborate with astronomers from different parts of the world, including Europe, America, and Asia. Meanwhile, I achieved several milestones, the first oral presentation in a conference, the first press release, and the first successful observation proposals in X-ray, radio and optical with data observed.

In September 2022, I will begin postdoctoral research at the Max Planck Institute for Extraterrestrial Physics. I will be part of the eROSITA clusters and cosmology working group, focusing on galaxy clusters and groups in the eROSITA All Sky Survey.

Acknowledgments

Going abroad for a PhD on a new topic is a big step, especially when you have to deal with a two-year pandemic. It would be difficult to complete it without the help and support of my supervisors, colleagues, and family.

First of all, I would express my sincere thanks to all support staffs in Leiden Observatory (Evelijn, Monica, Marjan, Alexandra, Erik, David, Hafize and Jacqueline), SRON (Esther and Frank), and Service Centre International Staff of Leiden University (Yvonne, Mariëlle and Saskia). You all did a fantastic job making my life in the Netherlands go smoothly and easily, allowing me to focus on my research.

I am grateful to my supervisors and SRON colleagues Aurora, Jelle, another Jelle, Hiroki (the unforgettable 5 a.m. deadline), Daniela, Liyi, Jan-Willem, Cor, Lucien, Elisa, Jean, Michael and Francois (I account you still a SRON member, thank for organizing workshops in ESTEC). I am also greatful to STRW radio experts Reinout, Andrea, Tim, Huib and Huub for your support at a completely different wavelength. I would also like to thank my external collaborators, Duy, Chiara, Annalisa, Marcüs, Larry, Shea, Ralph, John, Yuto, Okabe-san, Rossella (especially for your reference letters during my postdoc search), Virginia, Luca, Fabio, Mariachiara and Dominique, for your discussion and input.

Great thanks to my PhD mates Lydia (my train mate!), Zhenlin, Anwesh, Anna, Roland (also for your great Dutch translation of the summary), Erik, Chen and Yanling. And I will not forget the help from previous PhDs Igone, Gabriella, Daniele and Nastasha at the beginning stage.

I am deeply indebted to my wife Siqi. Your understanding and support is invaluable to me. I also appreciate the firm support from my parents and parents-in-law.